UCLouvain

École polytechnique de Louvain

# Thermal non equilibrium implementation within Argo

Author: **Antoine GHYOOT**
Supervisors: **Philippe CHATELAIN, Pierre SCHROOYEN**
Reader: **Véronique DIAS**
Academic year 2022–2023
Master [120] in Mechanical Engineering

# ABSTRACT

The correct design of the ablative protection system of a spacecraft is crucial for any space mission involving atmospheric reentry. Such a design is possible through robust and reliable numerical tools which allow an accurate modeling of the aerothermal loads experienced by the thermal protection system. During atmospheric reentry, the extreme velocity of the vehicle will make it endure a harsh environment characterised by a non-equilibrium state due to the large thermal loads encountered. The present work addresses the implementation of thermal non-equilibrium within Argo, a discontinuous Galerkin numerical tool based on a strong coupling approach in the solving of the material response and the flow. The equilibrium assumption between the energy modes in the modeling of the flow field is alleviated by tracking the translational-rotational and vibrational-electronic energy modes at separate temperatures. The implementation is verified based on two test codes developed aside Argo. Several cases involving strong non-equilibrium phenomena are examined to illustrate the performances of the extended model. The obtained results demonstrated a large impact of non-equilibrium phenomena on the properties of the flow, especially on its chemical kinetic which is of prior interest when ablative processes are considered. This work aims to be a first step in the modeling of the thermal non-equilibrium within Argo. However, these results are sign of motivation for future work in improving the model presented in this work in order to capture high enthalpy flows in an even more accurate way.

# AKNOWLEDGEMENTS

Il serait impensable de commencer ce travail sans remercier toutes les personnes qui m'ont aidées, soutenues et encouragées durant ce travail, et ce tout au long de l'année.

En premier lieu, je tiens à remercier tout particulièrement deux personnes sans qui ce mémoire n'aurait jamais abouti. Pour commencer, je voudrais exprimer toute ma gratitude à mon promoteur, Pierre Schrooyen, qui a pu m'aiguiller tout au long de ce travail que ce soit au niveau de la compréhension de l'architecture complexe d'Argo ou bien sur la compréhension de la physique du problème. Je le remercie également pour ses accueils à Cenaero et surtout pour tout le temps qu'il m'a consacré pendant l'année, surtout la patience dont il a fait preuve durant l'installation d'Argo sur ma machine qui fut quelque peu fastidieuse.

J'aimerais également vivement remercier David Henneaux, doctorant au Von Karman Institute, pour tout son temps accordé lors de ce dernier quadrimestre et pour ses conseils et aides qui me furent extrêmement utiles à la compréhension et l'utilisation de $Mutation^{++}$.

Je remercie également mes amis qui ont pu me soutenir et me faire changer les idées quand ça n'allait pas. Que ce soit d'avant l'Université ou pendant, du KapTech au SupportKot, je ne pourrais tous les citer mais si vous lisez ces lignes, vous vous reconnaitrez. Je tiens quand même à spécifiquement remercier Matteo pour ses conseils et sa relecture qui m'ont permis d'avoir un avis externe précieux. Egalement, un tout grand merci à Isabelle, John, Patrick, Marc-André et Julien pour l'énergie et la motivation qu'ils ont réussi à me véhiculer de par leurs magnifiques réalisations.

Finalement, ces remerciements n'auraient pas lieux d'être sans une mention spéciale à ma mère, mon père et mon frère. Tout au long de ma vie, ils m'ont soutenu et m'ont permis de grandir dans les meilleures conditions. Si j'en suis là aujourd'hui, c'est essentiellemet grâce à eux et pour ça, **merci**. J'espère que ce travail, fruit d'un long parcours, et ce que j'ai accompli les rendront fier.

# NOMENCLATURE

## Abbreviations

| | |
|---|---|
| AUSM | Advection Upstream Splitting Method |
| CFD | Computational Fluid Dynamics |
| CM | Command Module |
| CR | Collisional-Radiative |
| DG | Discontinuous Galerkin |
| DPLR | Data-Parallel Line Relaxation |
| FEM | Finite Element Methods |
| GMRES | Generalized Minimal RESidual |
| GMT | General Multi-Temperature |
| LAURA | Langley Aerothermodynamic Upwind Relaxation Algorithm |
| LTE | Local Thermal Equilibrium |
| LTNE | Local Thermal Non-Equilibrium |
| MT | Multi-Temperature |
| OT | One-Temperature |
| RRHO | Rigid-Rotor and Harmonic-Oscillator |
| STS | State-To-State |
| TT | Two-Temperature |
| US3D | UnStructured3D |
| XML | eXtensible Markup Language |

## Greek symbols

| | |
|---|---|
| $\alpha$ | Reactant stoechiometric coefficient |
| $\beta$ | Product stoechiometric coefficient |
| $\gamma$ | Heat capacities ratio |
| $\epsilon$ | Energy level |
| $\theta_{el}$ | Electronic characteristic temperature |
| $\theta_{vib}$ | Vibrational characteristic temperature |
| $\mu$ | Dynamic viscosity |
| $\nu$ | Vibrational frequency |
| $\rho$ | Density |
| $\sigma$ | Effective cross-section |
| $\tau$ | Relaxation time |
| $\tau_{ET}$ | Heavy-electron translational energy relaxation time |
| $\tau_{VT}$ | Vibrational-translational energy relaxation time |
| $\boldsymbol{\tau}$ | Viscous stress tensor |
| $\Phi$ | Non-equilibrium coupling factor |
| $\dot{\omega}$ | Species mass production rate due to chemical reactions |
| $\Omega$ | Energy transfer rate |

## Roman symbols

| | |
|---|---|
| $c$ | Speed of sound |
| $c_p$ | Heat capacity at constant pressure |
| $c_v$ | Heat capacity at constant volume |
| $\mathbf{d}$ | Specific driving force |
| $D$ | Multi-component diffusion coefficient |
| $e$ | Internal energy |
| $e_V$ | Vibrational-electronic-electron energy (TT model) |
| $E$ | Total internal energy |
| $E_a$ | Activation energy |
| $\mathcal{E}$ | Set of energy levels |
| $g$ | Degeneracy of a particular energy level |
| $h$ | Planck's constant |
| $h$ | Enthalpy |
| $H$ | Total enthalpy |
| $\mathcal{H}$ | Set of heavy particles |
| $\mathcal{H}^p$ | Set of polyatomic heavy particles |
| $\mathbf{I}$ | Identity second order tensor |
| $I$ | Moment of inertia |
| $\mathbf{J}$ | Diffusive flux |
| $J$ | Rotational quantum number |
| $k$ | Normal mode |
| $k_b$ | Backward reaction rate |
| $k_B$ | Boltzmann's constant |
| $k_f$ | Forward reaction rate |
| $k^{eq}$ | Equilibrium reaction rate |
| $K_c$ | Equilibrium constant |
| $Kn$ | Knudsen number |
| $M$ | Molecular mass |
| $Ma$ | Mach number |
| $\mathcal{M}$ | Set of purely internal energy modes |
| $n$ | Electronic quantum number |
| $n^{\mathcal{H}}$ | Number of heavy particles |
| $n^{\mathcal{H}^p}$ | Number of polyatomic heavy particles |
| $n^{\mathcal{S}}$ | Number of species |
| $N$ | Density number |
| $\mathcal{N}_{vib}$ | Vibrational degree of freedom |
| $p$ | Pressure |
| $\mathbf{q}$ | Heat flux |
| $Q$ | Partition function |
| $Q_{rad}$ | Rate of energy loss due to radiation |
| $R$ | Specific gas constant |
| $\mathfrak{R}$ | Universal gas constant |
| $\mathcal{R}$ | Set of reactional mechanisms |
| $\mathcal{S}$ | Set of species |
| $T$ | Temperature |
| $T$ | Trans-rotational temperature (TT model) |
| $T_{el}$ | Electronic temperature |
| $T_{rot}$ | Rotational temperature |
| $T_{tr}$ | Translational temperature |
| $T_{tr}^e$ | Free electrons translational temperature |
| $T_{tr}^h$ | Heavy particles translational temperature |
| $T_{vib}$ | Vibrational temperature |

| | |
|---|---|
| $T_P$ | Park temperature |
| $T_V$ | Vibrational temperature (TT model) |
| $t$ | Time |
| $\mathbf{u}$ | Velocity vector with the components u,v,w |
| $v$ | Vibrational quantum number |
| $\mathbf{v}$ | Diffusion velocity vector |
| $\mathbf{x}$ | Cartesian coordinates vector |
| $Y$ | Mass fraction |

# CONTENTS

CHAPTER

# ONE

# INTRODUCTION

## 1.1 Context

Space access and its exploration have always been a challenge and areas of interest either from scientific or economic perspectives. In the past years, the Moon has regained its prominence by captivating the interests of many and projects concerning a wild scale of applications are currently developed by cooperation between agencies or even by private companies worldwide.

One of the current standout missions is the Artemis program, led by the NASA, aiming at a sustainable exploration of our natural satellite through the organization of regular missions which outcome would be the installation of a permanent post on the Moon. Build upon the legacy of the Apollo missions, the program should also allow the testing and development of equipment and procedures that will be implemented during future crewed missions to the surface of Mars. Private space companies are also making their mark in lunar exploration. Such as SpaceX which has announced ambitious plans for lunar missions, including the development of the Starship spacecraft, designed for crewed missions to the Moon and Mars. Their goal is to make space travel more accessible, with the Moon serving as a stepping stone for interplanetary travel and the establishment of a self-sustaining colony on Mars. Meanwhile, international collaborations are flourishing as well. The European Space Agency (ESA), China's CNSA, and other nations have launched successful lunar missions, delivering valuable insights into the Moon's composition, potential water ice deposits in permanently shadowed regions, and its historical evolution.

Each mission is different and many crucial steps will take place before their respective success. However, for planetary missions, one of them is particularly critical : the Entry-Descent-Landing (EDL) set manoeuvres. In fact, during this phase, extreme phenomena happen, and every small miscalculations could lead to enormous hazards for the spacecraft and its payload. Given the fact that atmospheric entry cannot be reproduced multiple times to accumulate data in an experimental framework, the numerical approach seems to be the best way to predict the mechanical and thermal loads on the spacecraft.

Ongoing improvements in computing performance continue to break down the barriers that once limited the modeling of complex physicochemical phenomena in realistic timescales. As a result, the desire to increase the accuracy of the already existing models has never been greater.

## 1.2 Atmospheric reentry

The aim of this section is to give to the reader the big picture of an Earth atmospheric reentry based on the Apollo AS-202 mission. In addition, the various thermochemical phenomena occurring in the environment surrounding the atmospheric entry vehicle will be proposed.

### 1.2.1 Reentry overview

The liftoff of the Apollo AS-202 mission took place on the afternoon of Aug. 25, 1966. Mounted on the top of a Saturn 1B rocket, the unmanned spacecraft was sent into a lob-type trajectory in the objective of determining the performance of the vehicle and its subsystems in preparation of manned orbital missions. At T70, 70 minutes after the launch, the Command Module capsule separated from the Service Module and three minutes later, at T73, the capsule performed its reentry into the Earth atmosphere.

As it decelerated, the vehicle experienced various numbers of flow speed regimes during its descent (see Fig. 1.1) from hypersonic to subsonic passing by the supersonic and transonic flow regimes. These regimes are characterised by the Mach number ($Ma$) which is defined as

$$Ma = \frac{u}{c}, \tag{1.1}$$

where $u$ represents the velocity of the body and $c$ the speed of sound, both in meters per second. For the subsonic regime, this Mach number is strictly below unity while it lies between 0.8 and 1.2 for the transonic one. The clear Mach number transition value between the supersonic and hypersonic regimes can be argued. It is said to be at Mach 5 but no particular visible reaction would occur at this limit, as opposed to the ones observabled at the transonic regime. Rather, certain physical flow phenomena will become progressively more important as the Mach number increases to higher values.

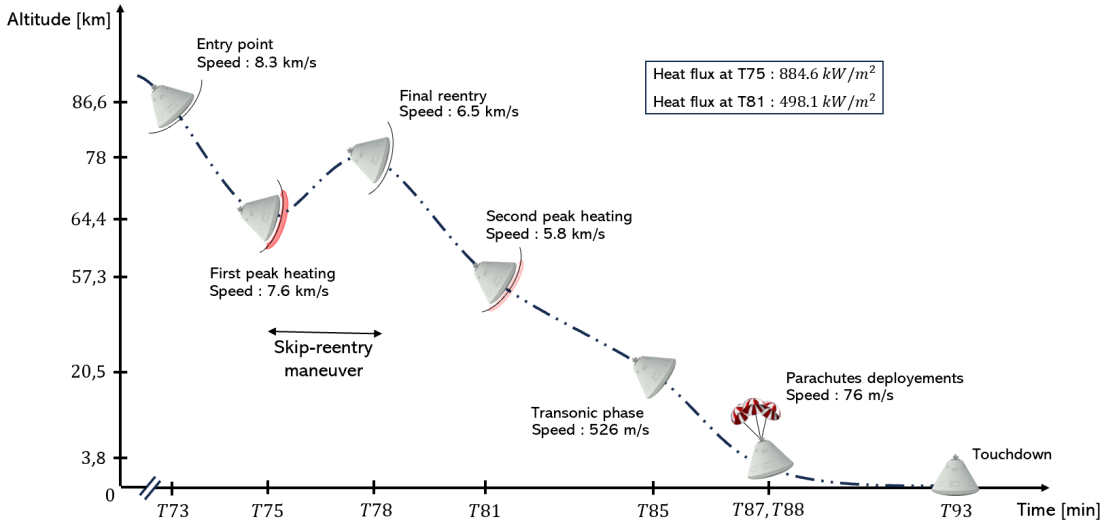


Figure 1.1: Illustration of the flight trajectory of the unmanned, suborbital test flight module during the AS-202 mission. Only some of the key steps of the reentry are represented but the reader is invited to read the technical report of the mission in [58] for an in-depth discussion.

In general, as the entry vehicle collides with the so far undisturbed atmospheric gas, it generates pressure waves propagating in the surrounding at the ambient speed of sound. For the subsonic regime, these pressure waves "inform" the upstream flow in such a way that its constituting particles have time to "get out" of the way of the incoming vehicle. However, when the vehicle velocity is greater than the speed of sound ($Ma > 1$), these particles will not have time to move out and will stack in front of the body creating a very thin compression zone.

This zone is more commonly called a shock and can have various forms depending on the vehicle's geometry. As shown on Fig. 1.2, in case of a blunt body, a bow (or detached) shock will appear where its standoff distance with the body front will be closely related to the traveling speed of the latter. For Earth atmospheric reentry, the peak velocity can climb up to 12 [km/s] but more extreme values can be reached like the 47.4 [km/s] experienced by the Galileo probe during its entry into the Jupiter's atmosphere.

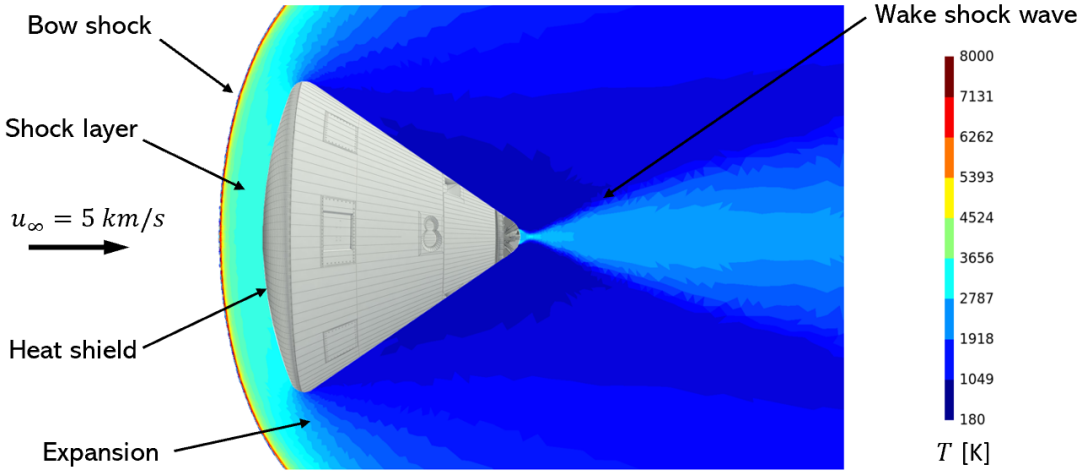


Figure 1.2: Temperature distribution around the Apollo Module Command traveling in hypersonic regime at 5 $[km/s]$. The surrounding medium is initially composed of a pure and reactive molecular oxygen mixture.

While the flow speed regime is described by the Mach number, another dimensionless number allowing the flow regime to be determined in terms of the medium continuity is used : the Knudsen number (Kn). It is defined as

$$Kn = \frac{\lambda}{L}, \tag{1.2}$$

where $\lambda$ is the molecular mean free path length [1] and $L$ a representative physical length scale, like the diameter of the capsule for example. The Knudsen number helps determine the validity of the continuum assumptions in the modeling of a given problem. For altitude exceeding 80 kilometers, the mean free path length between molecules is such that continuum mechanic becomes invalid and the Navier-Stokes (NS) equations are inadequate for accurately predicting regions with such flow behaviour. The flow is then qualified as rarefied and statistical mechanic approaches, such as the Direct Dimulation Monte Carlo (DSMC) particle-based methodology, must be used. Nevertheless, only altitudes allowing the continuum regime will be considered in this work.

Note that the reason of a blunt body for the capsule's geometry has not been explained yet. It may seem obvious but the challenge of the atmospheric reentry is to slow down the capsule

[1] The mean free path length can be seen as the maximum distance a particle can travel before colliding with another one

while maintaining its integrity. It is also important to understand that the dissipation of the vehicle kinetic energy is not due to the friction of the capsule with the atmosphere given the low air density at high altitudes. The effects of the energy loss due to friction will only play a role at low altitudes where most of the kinetic energy has already been dissipated. Instead, the quasi-entire amount of the kinetic energy is transformed to thermal energy by means of the shock appearing at the front of vehicle. For a blunt body, the bow shock will generate a high level of aerodynamic drag that will slow down the vehicle during its reentry.

As the flow passes the shock, it abruptly decelerates entering in the subsonic regime. A byproduct of this flow deceleration is a significant increase in the post-shock pressure and temperature resulting in a high enthalpy flow that will be convected downstream and which must be dissipated to preserve the capsule integrity. This abrupt increase in temperature due to the shock can be noticed on Fig. 1.2 where the peak value reaches 8000K. However, a particularity of the bow shock is its distancing with respect to the surface of the vehicle. This distance is represented by the shock layer and its thickness can vary depending on the velocity of the vehicle. As it will be discussed in the next section, this layer is very reactive and acts like a damper as the occurring thermochemical phenomena will "consume" a part of the flow's energy. The main result is that a fraction of the overall thermal energy reaches the surface of the vehicle where its thermal protection system (TPS) will diminish it even further to acceptable temperatures.

Finally, to give an order of magnitude, let us consider back the case of the AS-202 mission. Given the flight data at the entry point (see Fig. 1.1), the Apollo module's kinetic energy to be dissipated was approximately 191.41 $[GJ]$. Between the transonic phase and the entry point, the elapsed time was about 12 minutes which gives an averaged dissipation rate of 265.85 $[MJ/s]$. This represents the energy required to bring 115.5 $[kg]$ of water initially at room temperature to the boil every second. Note that the heat flux is not constant during the flight and attempts in minimizing it by lengthening the reentry time through ballistic manoeuvres, such as the skip-reentry procedure, are usually performed.

### 1.2.2 Thermochemical phenomena

As previously discussed, the bow shock appearing in front of the capsule at hypersonic regime will slow the post-shock flow to subsonic speeds. A consequence of this flow deceleration is a significant increase in the post-shock temperature reaching thousands of degrees. Considering the Earth atmosphere, the diatomic particles constituting the medium will jump from a high to low kinetic energy state resulting in an excitation of their translational mode. Following this excitation, the vibrational, rotational and electronic internal modes will be in turn excited through collisional processes leading to a non-equilibrium state of the gas. These excitation processes will lead to a highly reactive flow characterised by numerous reactions as shown on Fig. 1.3, a brief listing is given hereunder.

When the vibrational mode of the nitrogen and oxygen molecules becomes sufficiently excited, dissociation can occur leading to the formation of atomic nitrogen and oxygen species. Consequently, these new species will react giving rise to the formation of nitric oxide molecules through exchange processes.

In addition, the excitation of the electronic mode will excite the bound electrons of the atoms and molecules to higher electronic states. If this excitation is sufficiently high, these electrons can be separated from their parent species leading to a partially ionized mixture. A plasma is then formed and the free electrons will participate to the reactional mechanism through associative and impact ionization reactions with the neutral or charged heavy species [2]

On the other hand, de-excitation of the electronic mode leads to radiation as the particles emit

[2]The designation *heavy particles* for every constituents but the electrons of a mixture is introduced here and will be used later

a photon as they drop to lower electronic energy states. This radiant energy can add up to the heating load on the heat shield or it can be absorbed by other particles causing them to jump to higher energy levels. Note that radiation can also reduce the temperature of the shock layer by a process referred as "radiative cooling" [76].

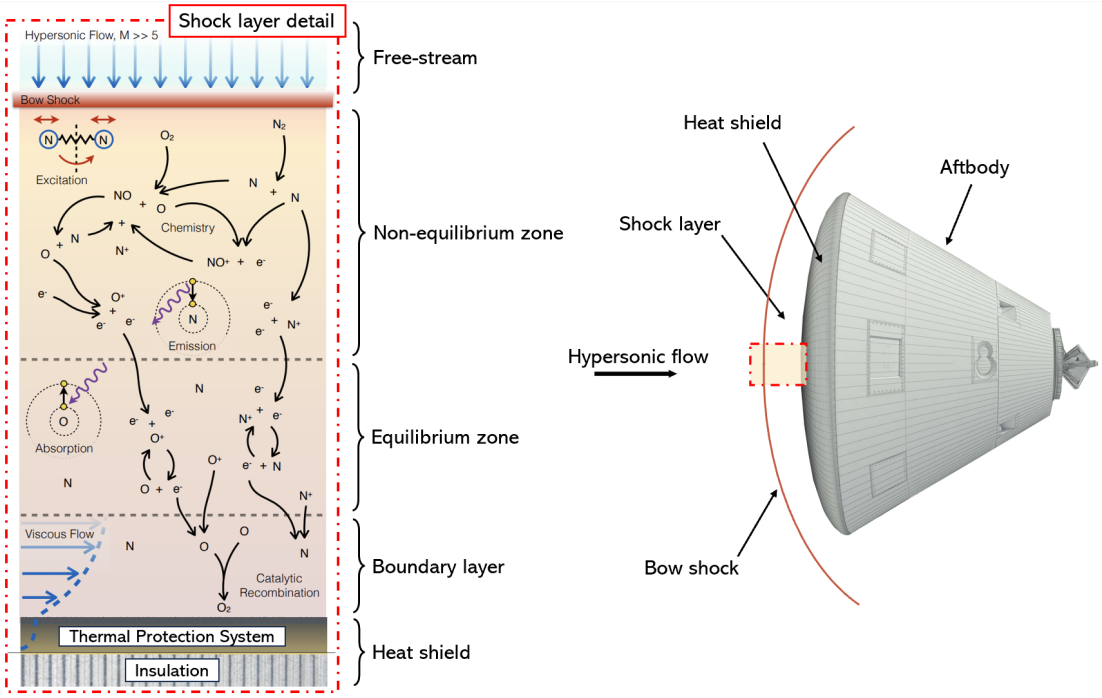


Figure 1.3: Detail of the shock layer and its related thermochemical phenomena. Left figure is taken from (S. Scoggins, VKI *Mutation*$^{++}$ Training Day, June 15, 2018).

All these collisional processes consume a lot of the gas internal energy causing its temperature to rapidly drop as it shown on Fig. 1.2 where the temperature in the shock layer jumped from 8000K to approximately 3000K. Given the huge energy depletion, the thermochemical properties of the flow will tend to equilibrate when exiting the non-equilibrium zone. As the diminished, but still relatively high enthalpy flow, progresses towards the surface of the vehicle, a boundary layer develops due to viscous interactions. Given the lower temperature in this region compared to the shock layer, catalytic and recombination reactions, such as the re-formation of molecular oxygen, can arise.

Finally, the heat reaching the surface due to convection and radiation is transferred deep in the TPS by conduction and diffusion. Due to the temperature rise, thermal decomposition of the TPS material (fibers coupled to a resin matrix) will occur allowing the absorption of the excess heat through two different mechanisms. The first one, the pyrolysis, consists in endothermic reactions that decompose the resin generating a pyrolysis gas. The latter is then blown out of the porous material and injected into the boundary layer inducing a blockage of the inbound convective heat flux from the shock layer. The second degradation mechanism is the erosion of the remaining carbonized resin and the fibers by means of heterogeneous chemical reactions, sublimation and spallation.

To illustrate the harsh environment suffered by the Apollo Module Command during its atmospheric reentry, a comparison of the state of the Apollo Module Command before the launch and after its recovery is displayed on Fig. 1.4.

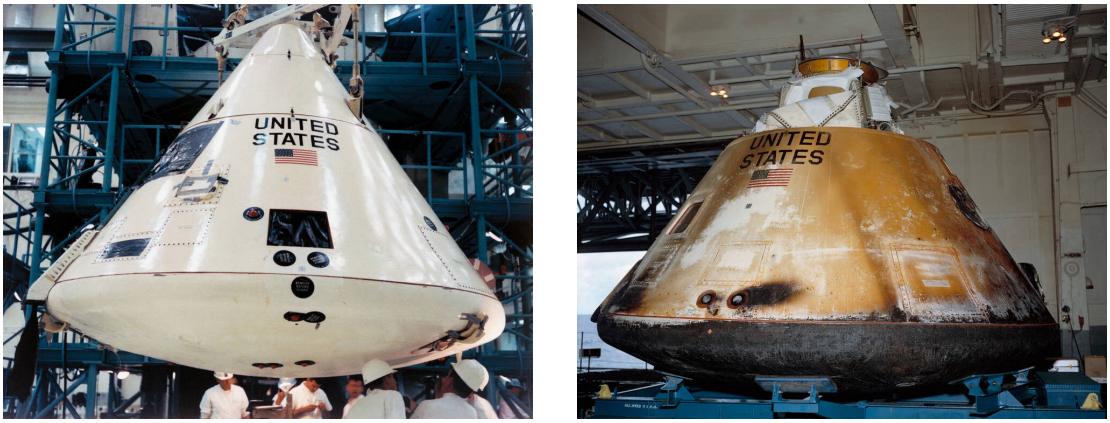


(a) Apollo CM before launch

(b) Apollo CM after its recovery

Source: `https://rb.gy/zv7wy`

Figure 1.4: The Apollo Command Module before and after the AS-202 test flight mission.

***Remark :***

As the material response is not of interest in this thesis, a mere introduction is given in this chapter in sight of providing to the reader most of the thermochemical phenomena happening from the shock to the insulation layer of the capsule. For in-depth discussions of this topic, see [74, 76].

## 1.3 State-of-the-art

As explained in the previous section, the atmospheric reentry phase is crucial for any mission and knowledge of its phenomena is of prior interest. Given the extreme cost and the rare occurrence of in-flight experiments, such a knowledge is mainly accessible to us by numerically reproducing the flow field. Therefore, great efforts in the development of accurate models have been conducted all around the world by many research centers and institutes. The aim of this section is then to provide a review of the current state-of-the-art in the modeling of high enthalpy flows with a focus on topics relevant to this thesis.

### 1.3.1 Experimental tools

Reproducing flight conditions at hypersonic regimes is very harsh but also, and mainly, very costly. However, the experimental framework may turn out to be necessary as it can provide precious real conditions data that can be compared to the outputs of the numerical models. To obtain the conditions a spacecraft would experience during its reentry, one can distinguish two main approaches : in-flight and ground-based experiments.

**In-flight experiments :**

The first approach consists in performing an atmospheric reentry with a test vehicle equipped with specific instruments depending on the data to be collected. A direct example is the previously seen AS-202 mission during the Apollo program where the objective, among others, was to test the TPS of the Apollo Command Module (see Fig. 1.4). Another flight experiment related to the Apollo program was the FIRE II (Flight Investigation of Reentry Environment) experiment. The objective was to specifically measure the convective and radiative heating of a body entering the dense atmospheric layers at high velocity (11.4 $[km/s]$). Launched in the sixties, the capsule was equipped with radiometers and calorimeters (see Fig. 1.5) and it remains one of the best sources of aerothermal heating data. Forty years later, these data are

still used to validate numerical models such as the Collisional-Radiative one proposed Panesi *et al.* [62].

More recently, in 1998, the European Space Agency (ESA) performed the very first guided sub-orbital reentry vehicle built, launched and recovered by Europe with the Atmospheric Reentry Demonstrator (ARD) [83]. Launched with an Ariane 5, the on-board measurement tools of the vehicle allowed to build an experimental database to be used in the development of future reentry vehicles. Let us also cite the Hypersonic Flight Experiment (Hyflex) [73], a reentry demonstrator prototype which was launched in 1996 by the National Space Development Agency of Japan (NASDA) aiming to test carbon-carbon heat shielding tiles and to gather data on hypersonic lifting. Despite succeeding its reentry, the prototype regrettably sank in the Pacific after splashdown before it could be recovered.

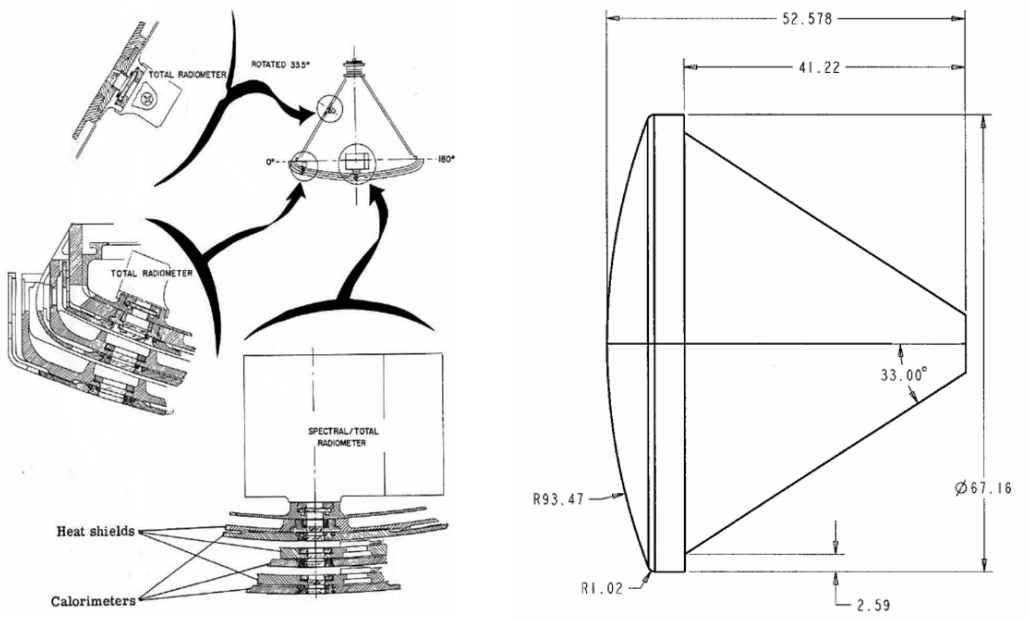


Figure 1.5: Relevant dimensions (in centimeters) of the FIRE II reentry vehicle along with the positions of its measuring instruments. Left and right images are respectively taken from [47] and [87].

Note that, even if this approach provides highly valuable data, the small occurrence of in-flight experiments constraints their flexibility. Therefore, ground-based experiments mimicking the extreme conditions of atmospheric reentries have been developed all around the world.

**Ground-based experiments :**

According to sought-after purpose, several facilities can be used and can be distinguishable by the conditions they can recreate and also their operational time. For example, the VKI Plasmatron facility (see Fig. 1.6a), in Belgium, allows to reproduce high enthalpy flows during several minutes which is very suitable to study the material response of TPS samples. On Fig. 1.6b, the cork heat shield of the ESA's Qarman (QubeSat for Aerothermodynamic Research and Measurements on Ablation) CubeSat [72] is being tested burning away in simulated atmospheric reentry conditions. However, the Plasmatron is limited to supersonic flows with its two nozzles reaching a flow regime of Mach 2,6 and 3,2.

When the aerodynamic of spacecrafts during atmospheric is studied, hypersonic cold wind tunnels are more appropriate as they can generate hypersonic flow typically from Mach 5 to 20 for longer periods of time. One can cite the SR3 low density wind tunnel-facility [1] from

the CNRS which can reproduce subsonic, supersonic and hypersonic flows up to Mach 22 in rarefied conditions. One advantage of this facility resides in its almost unlimited running time. This is particularly suitable to get rid of the instrumentation response time and to get a good stabilization of the flow conditions prior to experiments.

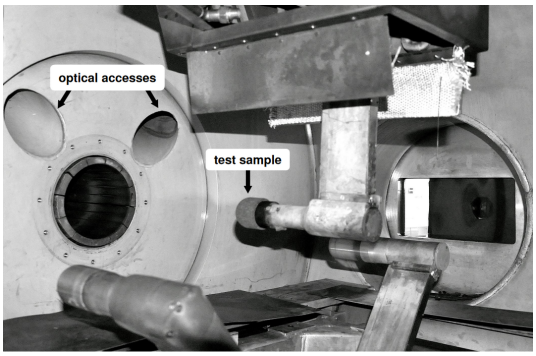


(a) Plasmatron chamber

(b) Ablation test of a thermal protection system sample of the Qarman CubeSat.
Source: https://rb.gy/o8m8m

Figure 1.6: Plasmatron facilty of the Von Karman Institute (VKI). The image of the chamber's configuration is taken from [74].

Finally, one can also cite the hypersonic shock tubes facilities such as the Large Energy National Shock (LENS) tunnel one [43]. These experiment tools allow to reproduce very high temperature conditions. However, their running time is extremely short ($\mathcal{O}(1e^{-3})[s]$) which makes the focus of their investigations on the chemistry aspect associated with hypersonic flows. Nevertheless, recent efforts in lengthening their operational time have been proposed such as in [59].

### 1.3.2 Numerical tools

Given their replicability and wild range of applications, continuous research efforts are proposed in the development of efficient and robust computational models that effectively capture the extreme phenomena related to atmospheric reentry. As explained in Sec. 1.2.2, these phenomena are represented by strong chemical and thermal non-equilibrium which can have an impact on the physics of the flow if they are badly modeled. Therefore, during the last forty years, intensive efforts in the treatment of the thermal non-equilibrium have been made through various energy partitioning models. Most of the solvers rely on the *Two-Temperature* model which can be attributed to the works of Park [65, 63] as explained in Sec. 2.2. Forty years later, this model is still widely used for aerospace engineering applications thanks to its capacity in providing satisfactory results for multi-dimensional problems. As it will also be the model of interest in this thesis, an overview of three CFD solvers treating thermal non-equilibrium in the continuum region based on this model is proposed in the following paragraph.

Named after its implicit time integration method, the DPLR (Data-Parallel Line Relaxation) code [86] is one of the hypersonic solvers developed at the NASA Ames Research Center that can successfully calculate hypersonic flow properties around flying objects. The other one, differing in its time integration scheme, is called LAURA (Langley Aerothermodynamic Upwind Relaxation Algorithm) [27]. Both solvers are parallel multiblock structured finite-volume codes which allow to solve reacting Navier Stokes equations where finite-rate chemistry and thermal non-equilibrium can be considered. These two codes have been notably used in the design of the TPS of the capsule Orion from the NASA Constellation Program Crew Explo-

ration Vehicle (CEV). Furthermore, alongside with the US3D solver, a comparison of their outputs with the FIRE II test flight has been made to investigate the reliability of their prediction in the aerothermal loads [29].

Developed at the University of Minnesota, the US3D (UnStructured3D) solver [13] greatly inherits its architecture from the DPLR solver. However, it has a number of distinct capabilities beyond those available in DPLR. One of them is the possibility of splitting the domain in independent grids to solve different problems separately such as the flow and the material response. Another interesting feature, especially for complex geometries, is the capacity of solving problem on unstructured meshes.

From the discussion in [74], the flow and the material can be solved independently and then coupled using appropriate boundary conditions at the fluid-solid interface. This approach is categorized as *weakly-coupled* as the two sides of the problems are solved separately. For example, Thompson and Gnoffo [81] proposed the implementation of such a procedure within the LAURA code where a diagram of the method is represented On Fig. 1.7. In a nutshell, a code is used to compute the equilibrium species at the surface (ACE) once the pressure and temperature are known from the flow (LAURA) and material (FIAT [19]) solvers. Then, the variation in the vehicle geometry due to ablation, determined by the material solver, is given as input to a regridding module (mvgrd) which will provide the updated mesh for the next iteration.

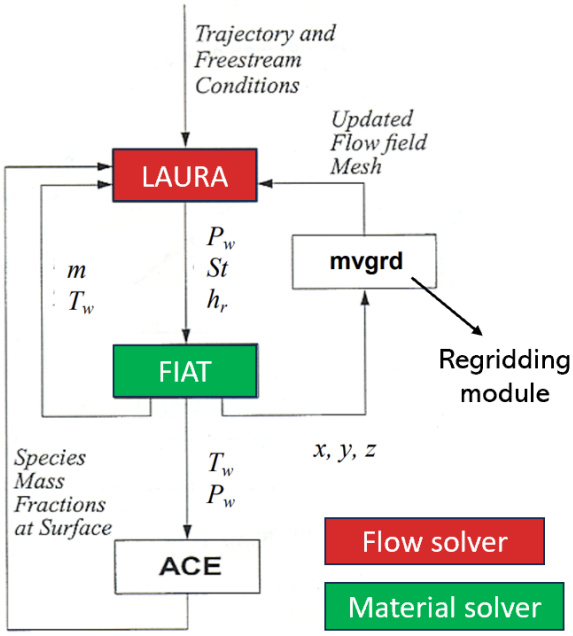


Figure 1.7: Weakly-coupled procedure for the recession treatment due to ablation within the LAURA solver. Image modified from [81].

However, the exchange of information at the boundary can be performed only at defined time steps and instabilities may appear because of the complex and highly non-linear behaviour of ablation problems. Therefore, another type of coupling methods, categorized as *strongly-coupled*, is usually preferred. The latter consists in solving both problems in an unified tool where the fluid and solid phases are computed within the same domain. Such a fully-coupled fashion is at disposal within the US3D solver for example. Nonetheless, most material response codes, the one used in US3D included, consider heat and mass exchanges as a surface phenomena only [74]. In particular, volume ablation is usually neglected and this

strong assumption can lead to inaccurate results, especially for highly porous materials.

To answer this problem, Schrooyen [74] implemented, in the scope of his PhD thesis, a new module related to ablation in the multi-physics platform Argo, developed at Cenearo in Belgium (a presentation of Argo and its Discontinuous Galerkin based spatial discretization method is proposed in Sec. 3.2). The purpose of this module, called *DGAblation*, is to model the response of an ablative material submitted to a high enthalpy flow using a strong coupling approach in sight of investigating the competition between surface and volume ablation phenomena. Combined with the benefits of its spatial discretization scheme in modeling complex geometry with unstructured meshes at high orders, this module allowed Argo to stand out from the previously cited solvers thanks to its high-fidelity in modeling ablation phenomena.

Nevertheless, its strength mainly resides in solving the material part of the domain. In fact, compared to US3D, LAURA, DPLR and many others solvers such as DLR TAU [75], LeMANS [56], SU2-NEMO [45] or hy2Foam [16, 15], the flow part of Argo is not fitted with the treatment of thermal non-equilibrium. Given the strong coupling approach of Argo, an accurate modeling of the thermochemical phenomena occurring in the shock layers is then crucial.

In fact, as shown on Fig. 1.8, the quantities convected to the surface of the TPS, which are closely related to the modeling of the upstream flow, will participate in the gas-surface reactional mechanisms. For example, a possible impact of an inaccurate modeling of the gas flow can be the following. Among the heterogeneous, two oxidation reactions happen :

$$\mathrm{C_{(s)} + O_{2(g)} \longrightarrow CO_{2(g)}},$$
$$\mathrm{C_{(s)} + O_{(g)} \longrightarrow CO_{(g)}}.$$

As these reactions are exothermic, an overestimation of the molecular/atomic oxygen production could lead to an overestimated degradation of the phenolic resin within the TPS and vice versa if their production is underestimated. Because of this kind of results, extension of the gas flow model of Argo to treat thermal non-equilibrium in the scope of making it more reliable will be the motivation of this thesis.

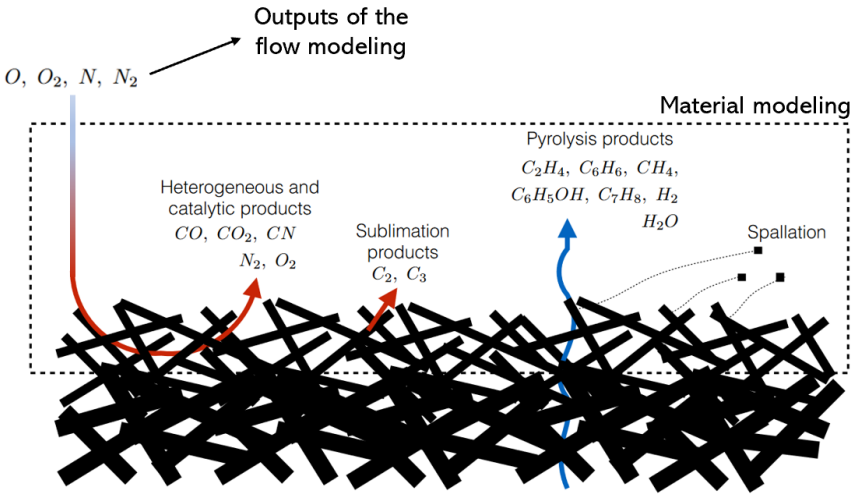


Figure 1.8: Schematic of the gas-surface interaction in the interface region of low density phenolic carbon fibers ablator for an Earth atmospheric entry. Image taken from Schrooyen [74].

## 1.4 Objectives and outlines of the thesis

From the discussion of the previous section, the objective of this thesis is to extend the reliability of the gas flow model of Argo through the treatment of thermal non-equilibrium. The model used in this work to treat thermal non-equilibrium will be the Two-Temperature model of Park given the lessened computing resources it requires compared to other models.

Including the introduction in Chapter 1, this thesis is composed of six chapters which are arranged in the following manner :

**Chapter 2** will begin by a quick introduction to statistical mechanics along with a review of the principal energy partitioning models required to treat thermal non-equilibrium. Secondly, and with respect to the Two-Temperature model, the governing set of equations applicable to hypersonic flows, and of use in this work, will be highlighted. Finally, the closure models for the thermodynamics, chemical reaction rates and energy transfer mechanisms with respect to the previously mentioned governing model will be presented.

**Chapter 3** will present the practical implementation of the physical model from Chapter 2 within Argo. In the first place, the presentation of Argo along with an introduction to the Discontinuous Galerkin methods is proposed. Then, the thermochemical library *Mutation*$^{++}$, which plays a central role as it provides the closure models, will be reviewed. Next, two test codes developed aside from Argo to verify its correct implementation will be described. Finally, the extension of the numerical schemes proper to the Discontinous Galerkin methods to deal with extended model will be reviewed.

**Chapter 4** will provide a quantitative validation of the numerical implementations performed in Chapter 3. A simple problem allowing the verification of specific terms of the governing models will be applied to each code.

**Chapter 5** will apply the extended version of Argo to different problems based on the model validation provided in Chapter 4. The impact of thermal non-equilibrium on the flow properties will be studied along with a discussion of the current limitation of Argo in capturing sharp interfaces, such as shock, with high order methods.

**Chapter 6** will summarize the main achievements of the thesis and will finally provide some perspectives for possible future work.

CHAPTER

# TWO

# PHYSICAL MODELING

## 2.1 Introduction

During atmospheric re-entry, the extreme velocity along with the blunt geometry of the vehicle leads to the formation of a detached shock on its front. Across the shock, pressure, temperature and velocity change drastically reaching very high temperatures values leading to a high enthalpy flow which is then convected within the shock layer. This region, delimited by the shock itself and the thermal protection system of the vehicle, is subject to various thermal and chemical processes. Due to the equivalent timescales between those processes and the transit time of the particles in the shock layer, chemical and thermal non-equilibrium behaviours emerge and must be captured in order to predict accurately the properties of the flow. Therefore, the motivation for this chapter is to provide the governing equations which this thesis will rely on to describe the thermochemical phenomena occurring in the shock layer. In order to have the ins and outs of the governing model used in this work, the chapter is constructed in the following manner.

First, an introduction to statistical thermodynamic trough the review of the most popular energy partitioning models is proposed.

Then, based on the energy partitioning model chosen for this thesis, the common governing equations found in the literature for thermal non-equilibrium in hypersonic flows are reviewed.

Finally, the physical model used in the scope of this thesis is highlighted and the chemical kinetic, the thermodynamic properties as well as the energy transfer models necessary to close the governing equations are presented.

## 2.2 Energy partitioning

Determination of thermodynamic properties for equilibrium and non-equilibrium flow field requires knowledge of the energy distribution, or partition, among the allowable energy states of the species [2, 49, 82]. Given a generic gas, one can assume its composition by a large number of heavy particles (i.e molecules and atoms) and electrons, in case of (partially-) ionized gas.

Depending on their nature, these particles have several modes of energy :

1. Translational energy $\epsilon_{tr}$ resulting from the motion of the particle's center of mass.
2. Rotational energy $\epsilon_{rot}$ resulting from the particle's rotational velocity and its moment of inertia.
3. Vibrational energy $\epsilon_{vib}$ resulting from the back and forth motion of the molecule's atoms around an equilibrium point within the molecule and the potential energy associated with the intramolecular force.
4. Electronic energy $\epsilon_{el}$ resulting from the kinetic and potential energy of the orbiting electrons around the nucleus.

Hence, the total energy of a particle, in case of a molecule, is given by the sum of all the energy modes

$$\epsilon = \epsilon_{tr} + \epsilon_{rot} + \epsilon_{vib} + \epsilon_{el}, \tag{2.1}$$

and for atoms, only translational and electronic energy modes exist

$$\epsilon = \epsilon_{tr} + \epsilon_{el}. \tag{2.2}$$

From quantum mechanics, each energy mode is only permitted at discrete energy levels [2] as shown on Fig. 2.1. Levels that could contain several energy states due to degeneracy. The degeneracy of an energy level emerges from the fact that quantum mechanics not only quantize energy, but also angular momentum for example. Thus, for the rotational energy mode, a given level $j$ will have $g$ distinguishable states as the rotational momentum can have different directions, as shown on Fig. 2.2. In general, particles can jump from one state to another through collisions and/or radiative interactions.

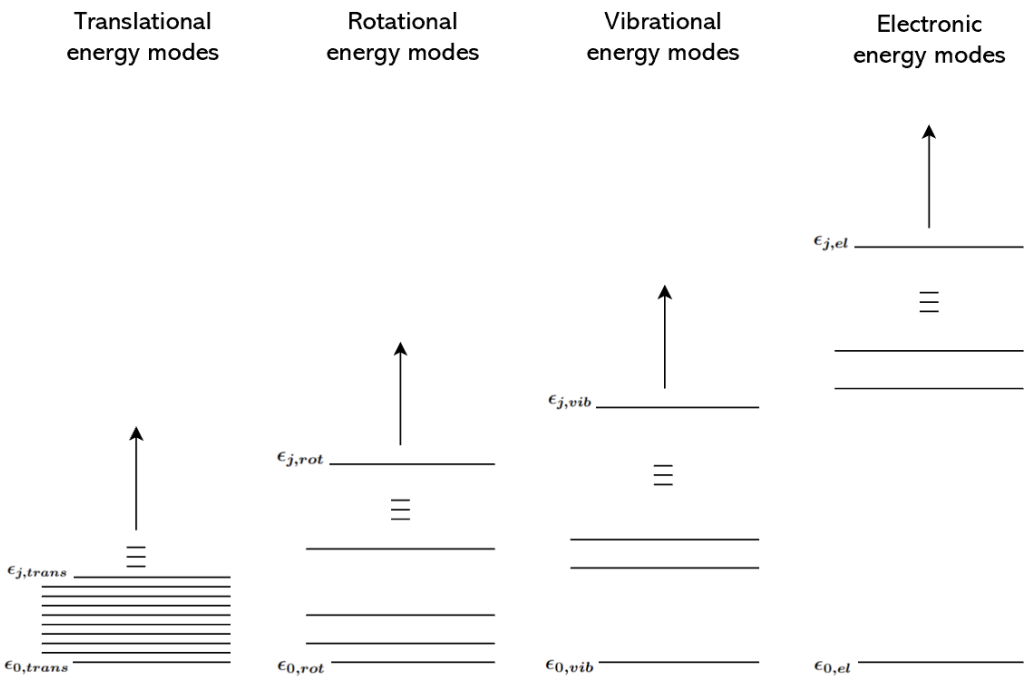


Figure 2.1: Schematic of energy levels for the different molecular energy modes. Figure modified from Anderson [2]

As mentioned in [76], "the use of *internal energy* should not be confused with the typical fluid dynamic description of the internal energy of a gas, which includes translational energy. Here,

internal energy is meant to differentiate between energy associated with the translation of the center of mass of a particle and the energy associated with the relative motion of its constituents (nuclei and electrons)". Furthermore, due to the closeness of the quantum spacings between energy levels of the translational mode, the latter will be assumed continuous [80] resulting in a semiclassical[1] approach of the system.

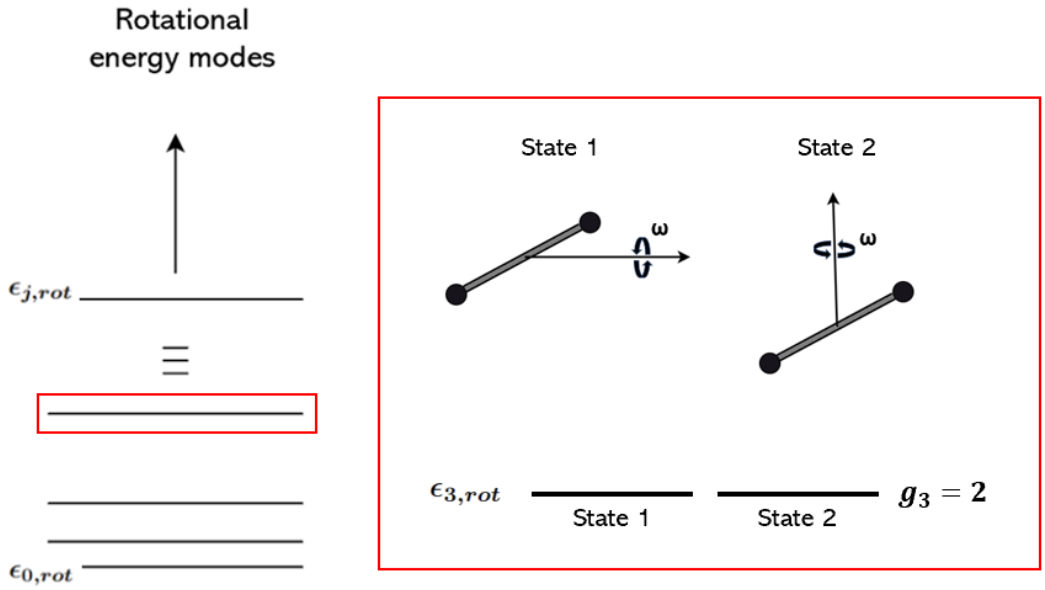


Figure 2.2: Illustration of a degenerate rotational energy level for a generic diatomic particle

### 2.2.1 Local Thermal Equilibrium (LTE)

In a reactive gas, the collisions among its constituting particles give rise to continual chemical processes and energy exchanges between the different energy modes. As these collisions occur, energy modes will tend to their equilibrium state in such a way that given numbers of collisions required to reach equilibrium are attributed to each mode. These numbers are called the "collisonal numbers" and can differ according to the energy mode. If the time required to reach the highest collisonal number is very short compared to the transit time in the flow field of interest, the system is considered as in equilibrium. Henceforth, all energy modes are characterised by the same temperature. On the opposite, if the transit time is much shorter than the lowest collisional number, the flow field is considered as frozen. For a given species $s$, the population of the energy levels follows a Boltzmann distribution and the probabilities for a specific energy level $j$ to be populated is computed as

$$p_j^s \propto g_j^s \exp\left(-\frac{\epsilon_j^s}{k_B T}\right), \quad s \in \mathcal{S}, \quad j \in \mathcal{E}^s, \tag{2.3}$$

where $g_j^s$ is the degeneracy of the level $j$ and the exponential term represents the Boltzmann factor where $\epsilon_j^s$ is the internal energy of level j of species s, $k_B$ the Boltzmann constant and $T$ the temperature. The set of all species in the mixture is denoted as $\mathcal{S}$ and the set of all the rovibronic[2]/electronic levels of molecule/atom $s$ is denoted as $\mathcal{E}^s$. To ensure the probabilities

[1] Semiclassical refers to a theory in which one part of a system is described quantum mechanically, whereas the other is treated classically

[2] Rovibronic is the contraction of rotational-vibrational-electronic

of all levels to add up to 1, the right-hand-side of Eq. (2.3) is divided by a normalization constant equal to the sum of all the Boltzmann factors. This constant is more commonly denoted as the partition function $Q^s$ for species s

$$p_j^s = \frac{g_j^s}{Q^s(T)} \exp\left(-\frac{\epsilon_j^s}{k_B T}\right), \quad \text{with} \quad Q^s(T) = \sum_j g_j^s \exp\left(-\frac{\epsilon_j^s}{k_B T}\right). \tag{2.4}$$

Then, the density number $N_j^s$ of species $s$ at a specific energy level $j$ is given as

$$N_j^s = \frac{N^s g_j^s}{Q^s(T)} \exp\left(-\frac{\epsilon_j^s}{k_B T}\right), \tag{2.5}$$

where $N^s = \sum_j N_j^s$ represents the total density number of the species $s$. From Eq. (2.5), one can observe that low-energy levels will be more likely to be populated and the system will also tend to populate excited levels as the temperature increases, as shown on Fig. 2.3 where probabilities for higher vibrational energy levels to be populated increase with temperature. Such distribution of the vibrational energy levels can have an impact on the dissociation of molecules if a preferential model is considered for example. A more detailed discussion of this topic is proposed in Sec. 2.5.

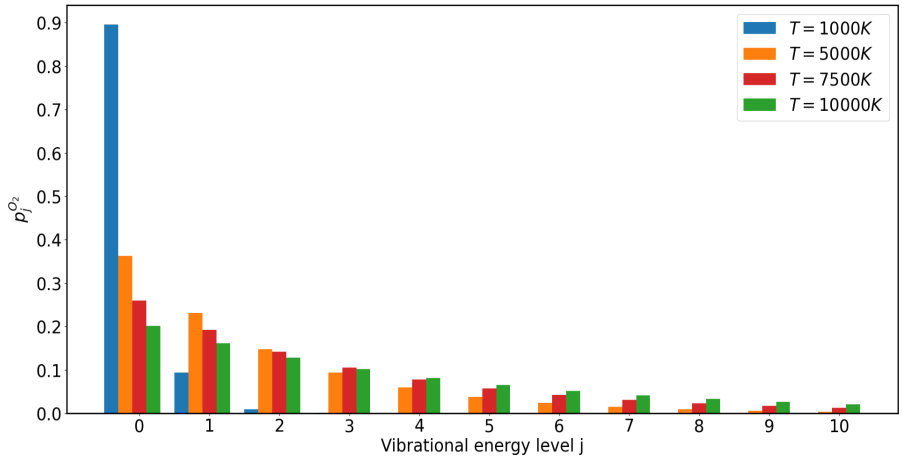


Figure 2.3: Vibrational population distribution among the 10 first energy levels at increasing temperatures up to 10000K.

When the time required for chemical reactions or energy exchanges mechanisms to accommodate themselves to local conditions becomes equivalent to the transit time, the equilibrium state is no longer valid. The flow field is therefore considered as in non-equilibrium and the model must be adapted to provide the distribution of energy levels for each species. Such models will be presented in the next subsections.

### 2.2.2 Local Thermal Non-Equilibrium (LTNE)

This subsection aims to provide some of the most popular energy partitioning models for non-equilibrium flow fields. The latest are classified on the basis of decreasing complexity to be modelled and also with their advantages and disadvantages. While some models will be reviewed without getting into details, emphasis will be placed on the multi-temperature models introduced by Park [64] and Lee [37] as it will be the one used in this thesis (see Sec. 2.3.2). Before going further, the author would like to point out that the following is greatly inspired from work of Scoggins in summarizing the existing models [76].

**State-Specific and State-To-State (STS) models :**

In order to completely describe any flow fields, one should know the energy state of all particles in the flow and their positions, versus time [76]. However, this method requires to track every particle individually which is theoretically possible but unfeasible from a computational point of view.

Another approach is to compute the population of particles related to each energy state as the number of these energy states is very small compared to the total number of particles in the flow. This method is known as "State-To-State" and currently represents the most rigorous energy partitioning model. Based on the availability of *ab initio* rate parameters for elementary collisional processes [61], these models can treat all internal energy levels as pseudo-species such that no assumption on their distribution is made.

In the case of the State-Specific models, the internal energy level populations can either be estimated through a Boltzmann distribution or the internal energy levels can be treated as pseudo-species. Such models are more specifically called "Collisional-Radiative" (CR) and they can differ dependently on the internal mode for which the energy levels are treated as pseudo-species. For example, in the Elecronic-specific CR model introduced by Cambier [11], all relevant collisional and radiative mechanisms between the electronic energy levels are treated as pseudo-species while the rovibrational levels of the molecules are populated according to Boltzmann distributions at temperatures $T_{vib}$ and $T_{rot}$ [60]. Likewise, the Vibrational-specific CR model [18, 69] considers the vibrational excitation and de-excitation mechanisms between the vibrational levels of the molecules as pseudo-species and only a rotational temperature is defined.

The main advantage of the State-Specific and the State-To-State models is their validity range as they are not assuming any distribution, or only partially for the State-Specific models. In fact, the Boltzmann distribution assumes only small departures from equilibrium, an assumption that may not hold anymore when strong non-equilibrium phenomena occur.

Nonetheless, despite their robustness, the CR and the STS models are prohibitively computationally expensive. Even if several methods have been introduced in order to reduced their complexity, like the energy binning and the coarse-grain models [36, 76] or even through machine learning based algorithms [12], their applications are reduced to 0D reactors or 1D problems such as nozzle flows for example [53]. Therefore, when it comes to compute multi-dimensional flows, simplified models called "Multi-Temperature" are usually preferred.

**Multi-Temperature (MT) models :**

Widely used in CFD platforms such as SU2-NEMO [45], DPLR, LAURA, and US3D [29], multi-temperature models separate the energy associated with any internal level between the different energy modes discussed in Sec. 2.2.1. However, the latter are now characterised by their own thermal bath instead of a single temperature as it was the case at equilibrium. The designation "multi-temperature" models results precisely from this separation between the temperatures associated with each energy mode. Given the classical approach for the translational mode and by neglecting spin–orbit coupling [42, 24], all internal energy levels of a diatomic molecule may be enumerated by the electronic, rotational and vibrational quantum numbers n, J and $v$, respectively. Then, under the hypothesis of decoupled energy modes, the energy at level $j = (n, J, v)$ of diatomic molecule $s$ is the following

$$\epsilon_j^s = \epsilon^s(n, J, v) = \epsilon_{el}^s(n) + \epsilon_{rot}^s(J) + \epsilon_{vib}^s(v), \tag{2.6}$$

where the pure electronic, rotational and vibrational energy modes contributing to the energy level $j$ are assumed to represent a thermal bath in equilibrium at separate temperatures $T_{el}$, $T_{rot}$, $T_{vib}$, respectively. The translational mode represents a thermal bath at temperature $T_{tr}$. In thermodynamics, thermal baths are theoretical concepts which represent large systems characterised by their own temperature. When a system contain several thermal baths at

different temperatures, the latter is considered as in non-equilibrium and energy exchanges can occur between them until equilibrium is reached (see Fig. 2.4).

From Eq. 2.6, the density number of species $s$ at level $j$ in Eq. (2.5) can now be expressed as

$$N_j^s = \frac{N^s}{Q^s\left(T_{el}, T_{rot}, T_{vib}\right)} g_{el}^s g_{rot}^s g_{vib}^s \exp\left(-\frac{\epsilon_{el}^s(n)}{k_B T_{el}} - \frac{\epsilon_{rot}^s(J)}{k_B T_{rot}} - \frac{\epsilon_{vib}^s(v)}{k_B T_{vib}}\right), \tag{2.7}$$

where the partition function $Q^s(T_{el}, T_{rot}, T_{vib})$ is given by

$$Q^s\left(T_{el}, T_{rot}, T_{vib}\right) = \sum_n \sum_J \sum_v g_{el}^s g_{rot}^s g_{vib}^s \exp\left(-\frac{\epsilon_{el}^s(n)}{k_B T_{el}} - \frac{\epsilon_{rot}^s(J)}{k_B T_{rot}} - \frac{\epsilon_{vib}^s(v)}{k_B T_{vib}}\right), \tag{2.8}$$

$$= Q_{el}^s(T_{el}) Q_{rot}^s(T_{rot}) Q_{vib}^s(T_{vib}). \tag{2.9}$$

Recalling the perfect decoupling between energy modes, one obtains the following generic expression for the density number of species $s$ at energy level $j$

$$N_j^s = N^s \prod_m \frac{g_m^s}{Q_m^s(T_m)} \exp\left(-\frac{\epsilon_m^s(i)}{k_B T_m}\right), \quad \text{with} \quad Q_m^s(T_m) = \sum_i g_m^s \exp\left(-\frac{\epsilon_m^s(i)}{k_B T_m}\right), \tag{2.10}$$

where $i \in \mathcal{E}_m^s$, the set of the pure energy levels of the internal energy mode $m$.

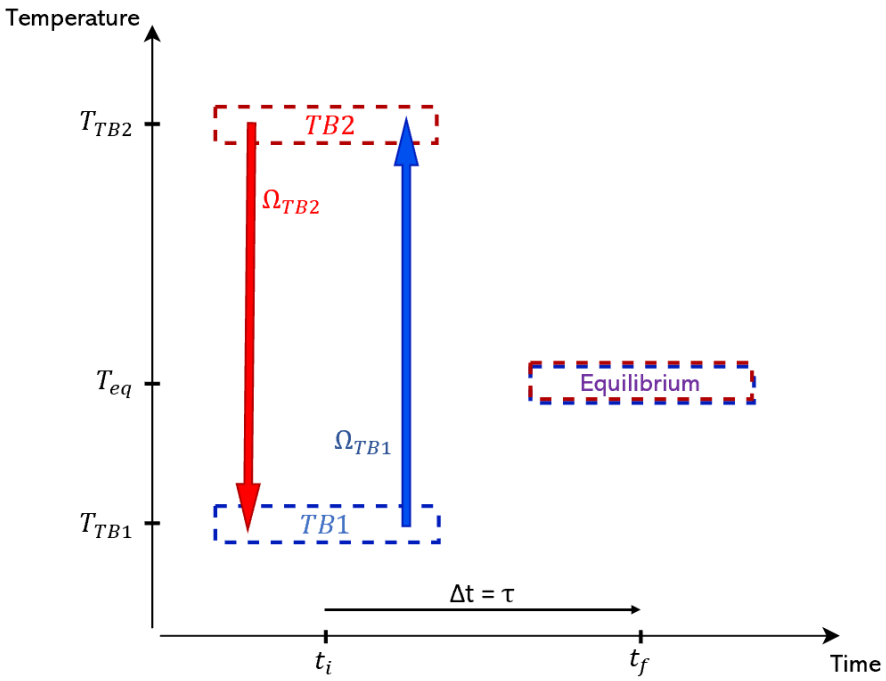


Figure 2.4: Schematic representation of the thermal relaxation towards equilibrium of two thermal baths initially in non-equilibrium at temperatures $T_{TB1}$ and $T_{TB2}$. The equilibrium state, characterised by the temperature $T_{eq}$, is reached through energy exchanges $\Omega$ after a relaxation time $\tau$.

Large interest has been devoted on MT models because they drastically reduce the complexity of the thermal non-equilibrium model, leading to better computational performances. However, the assumptions considered for the MT models could introduce errors on the thermochemical properties giving rise to discrepancies between the final results and the reality. For

temperatures under 2500K, errors can be negligible as only low-energy levels of the electronic ground state are more likely to be populated. On the other side, at extremely high temperatures, complete separability between all energy modes is not accurate because strong coupling exist between them. Considering a diatomic molecule for example, vibrational motion and centrifugal distortions due to rotation will cause the constituent nuclei's bond to stretch. These bond length variations will change the moment of inertia of the diatomic molecule on which the rotational energy is dependent. Hence, vibrational quantum number transitions will often be accompanied by transitions of the rotational quantum number, leading to a coupling between the two modes. Furthermore, dependency of the rovibrational spectroscopic constants on the electronic states and impact of the electrical anharmonicity [70] may also exhibit a coupling between rovibrational and electronic modes as shown on Fig. 2.5. In order to deal with such couplings, a General Multi-Temperature (GMT) model introduced by Jaffe [34] is reviewed in the next subsection.

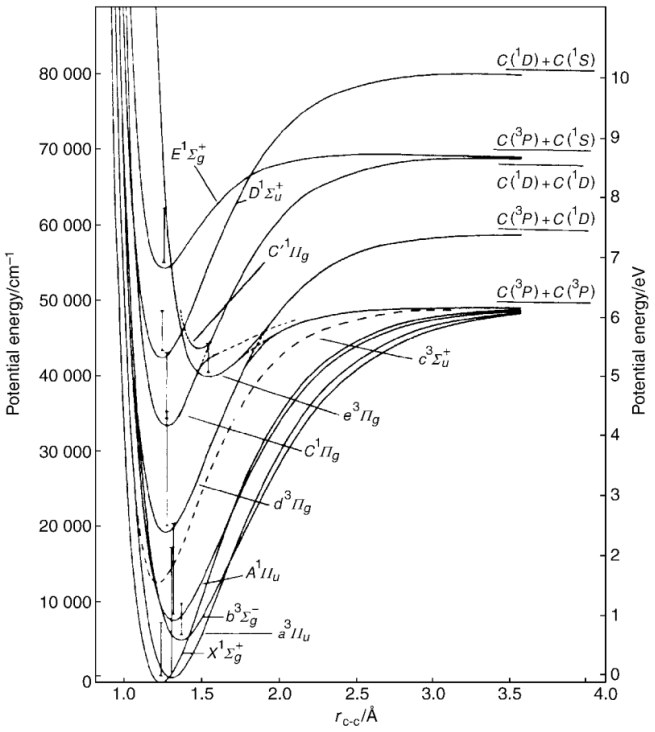


Figure 2.5: Potential energy curves for the ground and several excited states of $C_2$. Figure from [31]

Before going further, note that the case of a diatomic molecule has been considered until now but the MT models can be adapted to any polyatomic molecules. By considering a polyatomic molecule with $n$ nuclei, its number of vibrational degrees of freedom is given by $\mathcal{N}_{vib} = 3n - (l+3)$ where $l = 2$ if the molecule is linear and $l = 3$ otherwise. Such degrees of freedom, called "normal modes of vibration", arise due to the combinations of stretches, contractions, and bends that can occur between the bonds of atoms in the molecule. Therefore, additional vibrational frequencies $\nu_k^s$ are attributed to each normal mode $k$ and the vibrational partition function for the polyatomic molecule $s$ is updated as follows

$$Q_{vib}^s = \prod_{k=1}^{\mathcal{N}_{vib}} Q_{k,vib}^s(\nu_k). \tag{2.11}$$

Finally, polyatomic molecules of the mixture can have their own vibrational temperatures $T^s_{vib}$ which requires to solve vibrational energy conservation equations for the vibrational energy of each molecule [62].

**General Multi-Temperature (GMT) model :**

In the GMT model, the split between the energy modes contributing to energy level $j = (n, J, v)$ is the following

$$\epsilon^s_j(n, J, v) = \epsilon^s_{j,el}(n) + \epsilon^{s'}_{j,rot}(n, J, v) + \epsilon^{s'}_{j,vib}(n, J, v), \tag{2.12}$$

with

$$\epsilon^{s'}_{j,rot}(n, J, v) = \epsilon^s_{j,rot}(n, J) + \epsilon^s_{j,inter}(n, J, v)(1 - \alpha), \tag{2.13}$$

$$\epsilon^{s'}_{j,vib}(n, J, v) = \epsilon^s_{j,vib}(n, v) + \epsilon^s_{j,inter}(n, J, v)\alpha, \tag{2.14}$$

where $\epsilon^s_{j,rot}(n, J)$ and $\epsilon^s_{j,vib}(n, v)$ are respectively the pure rotational and vibrational energies for the given electronic level $n$. The term $\epsilon^s_{j,inter}(n, J, v)$ represents the interaction energy between the rotational and vibrational modes. Note that, given the coupling between the energy modes, the partition function in Eq. (2.8) can no longer be decomposed in a product of each energy mode contribution.

The constant $\alpha \in [0, 1]$ was introduced by Scoggins in [76] to showcase the distribution of the rovibrational interaction energy into rotational and vibrational modes while the Jaffe's model [34] gave the two extreme cases. If $\alpha = 1$ or $\alpha = 0$ , all of the interaction energy is either added to the vibrational or to the rotational mode, respectively. However, it has been shown that values of $\alpha$ have a minor effect on thermodynamic properties for diatomic air species [76, 34].

Even though the GMT model has a more realistic approach than the MT models, both are still relying on Boltzmann distributions which only assume small departures from equilibrium. Therefore, vibrational distributions will tend to non-Boltzmann profiles [53] when strong non-equilibriums occur leading to inaccurate values for the chemical kinetic parameters for example (e.g. the chemical reaction rates, see Sec. 2.5) [23].

## 2.3 Governing equations

In the last section, several energy partitioning models have been reviewed. These models describe how the energy is distributed among the allowable energy levels of a given species. Given the motivation of using the Multi-Temperature model to treat multi-dimensional flows, only this model will be considered in what follows. From the MT model, one obtained the following generic expression for the density number of species $s$ at energy level $j$

$$N^s_j = N^s \prod_m \frac{g^s_m}{Q^s_m(T_m)} \exp\left(-\frac{\epsilon^s_m(i)}{k_B T_m}\right) = f\left(N^s, T_m\right), \quad i \in \mathcal{E}^s_m. \tag{2.15}$$

From this relation, one can note that the density number of a species at a given energy level depends on total density number of this species $N^s$ and also on the temperatures related to each internal energy mode $T_m$ contributing to the energy level. These quantities, related to the flow field of interest, can be derived from a suitable set of mass, momentum and energy conservation equations. Thereby, the motivation of this section is to provide such equations.

Given a vehicle performing atmospheric re-entry, the latter will pass through atmospheric layers characterised by a decreasing Knudsen number. As discussed in Chapter 1, we will focus on an altitude range characterised a low Knudsen number such that the continuum regime can be assumed (see Fig. 2.6). The mixture composing the surrounding of the vehicle is considered

as a partially ionized gas composed of $n^{\mathcal{S}}$ distinct species. Given the atmospheric gas composition, the set of species for air is the following : $\mathcal{S} = \{N, O, NO, N_2, O_2, N^+, O^+, NO^+, N_2^+, O_2^+, e^-\}$. Any quantity $\lambda$ (e.g. density or pressure) related to a specific species $s$ is denoted as $\lambda^s$ where $s \in \mathcal{S}$ can either be a free-electron, a neutral or charged heavy particle such that $\mathcal{S} = \{e\} \cup \mathcal{H}$ and $n^{\mathcal{S}} = 1 + n^{\mathcal{H}}$. A subset of $\mathcal{H}$, regrouping only the polyatomic neutral or charged heavy particles, is denoted as $\mathcal{H}^p$. Moreover, due to the strong disparity in mass between free electrons and heavy particles, it is assumed that heavy particles translational modes represent a thermal bath in equilibrium at a common temperature $T_{tr}^h$ and free electrons at a temperature $T_{tr}^e$, which may differ from $T_{tr}^h$.

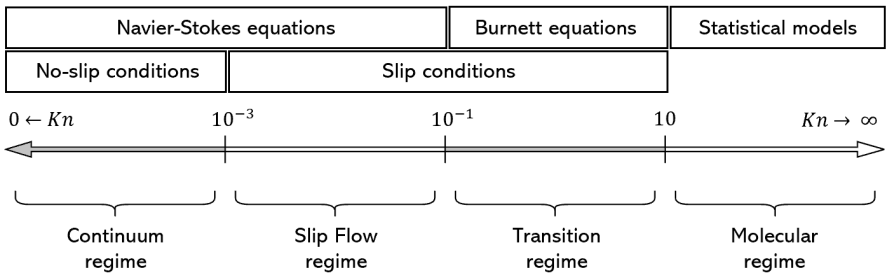


Figure 2.6: Flow regimes and valid models at different Knudsen number

As discussed in the introduction of this chapter, the flow field in the shock layer formed on the front of the vehicle is considered in thermochemical non-equilibrium. Therefore, a fitted energy partitioning model has been chosen, which is the MT model. According to the Boltzmann based distribution for the internal energy levels population, no pseudo-species are considered, unlike the CR or the STS models. Hence, the governing model is reduced to $n^{\mathcal{S}}$ species mass conservation equations, one momentum conservation equation, one total energy conservation equation, one free electrons energy conservation equation and $n^{\mathcal{M}}$ purely internal mode energy conservation equations. If separate vibrational temperatures are considered for each polyatomic particle, a set of $n^{\mathcal{H}^p}$ vibrational energy conservation equations is added.

These equations are more commonly nominated as the *non-equilibrium Navier-Stokes* equations and will be presented in the following subsection. Note that the following governing equations are only valid for the MT model. However, Scoggins [76] proposed a set of equations with a notation allowing it to be valid for any of the partitioning models seen in Sec. 2.2.

Finally, in the last subsection, the particular MT model used in the scope of this thesis is presented. This model is directly derived from the Navier-Stokes equations where the assumptions will be listed along with a small discussion regarding their impact on the model.

### 2.3.1 Non-equilibrium Navier-Stokes equations

#### Species mass conservation

The mass conservation equation for species $s$ can be written as

$$\frac{\partial \rho^s}{\partial t} + \boldsymbol{\nabla} \cdot (\rho^s \mathbf{u}) = \dot{\omega}^s - \boldsymbol{\nabla} \cdot \mathbf{J}^s, \qquad s \in \mathcal{S}, \tag{2.16}$$

where $\rho^s$ is the density of species $s$, $\mathbf{u}$ the velocity vector and $\mathbf{J^s}$ the diffusive flux of the species $s$ within the mixture. Neglecting the thermal diffusion effect [17], $\mathbf{J^s}$ can be expressed as

$$\mathbf{J}^s = \rho^s \mathbf{v}^s = \rho \sum_{i=1}^{n^{\mathcal{S}}} D^{si} \mathbf{d}^i, \tag{2.17}$$

where $\mathbf{v}^s$ is the diffusion velocity, $D^{si}$ the multicomponent diffusion coefficients and $\mathbf{d}^i$ the species specific driving forces [74]. The term $\dot{\omega}^s$ stands for the chemical source term of species $s$ due to homogeneous chemical reactions (see Sec. 2.5). Species mass production due to heterogeneous reactions near the thermal protection system is not included in the source term as the latter is considered sufficiently far away from the flow field of interest.

By summing Eq. (2.16) over all species in the mixture, one obtains the total mass conservation equation

$$\sum_{i=1}^{n^{\mathcal{S}}} \dot{\omega}^i = \sum_{i=1}^{n^{\mathcal{S}}} \rho^i \mathbf{v}^i = 0 \quad \xRightarrow[\text{yielding}]{} \quad \frac{\partial \rho}{\partial t} + \boldsymbol{\nabla} \cdot (\rho \mathbf{u}) = 0, \tag{2.18}$$

where the density of the mixture is given as $\rho = \sum_{i \in \mathcal{S}} \rho^i$.

## Momentum conservation

The momentum conservation equation can be expressed as follows

$$\frac{\partial (\rho \mathbf{u})}{\partial t} + \boldsymbol{\nabla} \cdot (\rho \mathbf{u}\mathbf{u}) = -\boldsymbol{\nabla} p + \boldsymbol{\nabla} \cdot \boldsymbol{\tau}, \tag{2.19}$$

where the mixture pressure $p$ is given as the sum of the partial pressures of its constituents, yielding

$$p = \rho R T_{tr}^h \sum_{i=1}^{n^{\mathcal{H}}} \frac{Y^i}{M^i} + \rho R T_{tr}^e \frac{Y^e}{M^e}, \tag{2.20}$$

where $Y^i$ and $M^i$ respectively denote the mass fraction and the molecular mass of the species $i \in \mathcal{H}$ while the exponent $e$ is related to the free electrons. By neglecting bulk viscosity and chemical pressure effects [20], the following expression for the viscous stress tensor $\boldsymbol{\tau}$ holds

$$\boldsymbol{\tau} = \mu \left[ \boldsymbol{\nabla} \mathbf{u} + \boldsymbol{\nabla} \mathbf{u}^T - \frac{2}{3} \boldsymbol{\nabla} \cdot \mathbf{u} \mathbf{I} \right], \tag{2.21}$$

where $\mu$ is the dynamic viscosity and $\mathbf{I}$ the identity second order tensor.

## Total energy conservation

The total energy conservation equation can be written as

$$\frac{\partial}{\partial t} (\rho E) + \boldsymbol{\nabla} \cdot (\rho H \mathbf{u}) = \boldsymbol{\nabla} \cdot (\boldsymbol{\tau} \cdot \mathbf{u}) - \boldsymbol{\nabla} \cdot \mathbf{q} + Q_{rad}, \tag{2.22}$$

where the total internal energy of the gas $E$ includes the sum of the internal and kinetic energies of the mixture such that $E = e + \mathbf{u}^2/2$. The internal energy of the mixture can be obtained as the sum of the internal energies of each species, yielding

$$e = \sum_{i=1}^{n^{\mathcal{S}}} Y^i e^i, \tag{2.23}$$

where the internal energy of a given species $s$ is the sum of the translational mode, treated classically, and the purely internal modes which are treated quantum mechanically as discussed in Sec. 2.2

$$e^s = e_{tr}^s(T_{tr}) + \sum_m e_m^s(T_m), \quad m \in \mathcal{M}, \tag{2.24}$$

where $\mathcal{M}$ denotes the set of the purely internal energy modes.

Similarly to the total energy, the total enthalpy $H$ is given as

$$H = h + \frac{1}{2}\mathbf{u}^2 \quad \text{with} \quad h = e + \frac{p}{\rho}. \tag{2.25}$$

Practical evaluations of the internal energy, enthalpy and other thermodynamic properties based on statistical mechanics is proposed in Sec. 2.4. Finally, the three terms on the right-hand-side in Eq. (2.22) respectively account for the work done on the fluid due to viscous forces, the heating related to conduction and diffusion of energy due to temperature and concentration gradients and the rate of energy loss due to radiation.

### Free electrons energy conservation

The energy conservation of the free electrons can be written as

$$\frac{\partial}{\partial t}\left(\rho^e e^e\right) + \boldsymbol{\nabla}\cdot\left(\rho^e h^e \mathbf{u}\right) = \mathbf{u}\cdot\boldsymbol{\nabla} p^e - \boldsymbol{\nabla}\cdot\mathbf{q}^e + \Omega^e + Q^e_{rad}. \tag{2.26}$$

The term accounting for the convection of the free electrons enthalpy in Eq. 2.26 can be decomposed as

$$\begin{aligned}
\boldsymbol{\nabla}\cdot\left(\rho^e h^e \mathbf{u}\right) &= \boldsymbol{\nabla}\cdot\left[\rho^e\left(e^e + \frac{p^e}{\rho^e}\right)\mathbf{u}\right], && (2.27)\\
&= \boldsymbol{\nabla}\cdot\left(\rho^e e^e \mathbf{u}\right) + \boldsymbol{\nabla}\cdot\left(p^e\mathbf{u}\right), && (2.28)\\
&= \boldsymbol{\nabla}\cdot\left(\rho^e e^e \mathbf{u}\right) + p^e\boldsymbol{\nabla}\cdot\mathbf{u} + \mathbf{u}\cdot\boldsymbol{\nabla} p^e. && (2.29)
\end{aligned}$$

By injecting this result in 2.26, the terms $\mathbf{u}\cdot\boldsymbol{\nabla} p^e$, representing the work done on electrons by an electric field induced from an electron pressure gradient, cancel each other out, yielding

$$\frac{\partial}{\partial t}\left(\rho^e e^e\right) + \boldsymbol{\nabla}\cdot\left(\rho^e e^e \mathbf{u}\right) = -p^e\boldsymbol{\nabla}\cdot\mathbf{u} - \boldsymbol{\nabla}\cdot\mathbf{q}^e + \Omega^e + Q^e_{rad}. \tag{2.30}$$

As it will be discussed in Sec. 3.4.2, Eq. 2.30 is preferred to Eq. 2.26 where a special treatment for the non-conservative term $-p_e\boldsymbol{\nabla}\cdot\mathbf{u}$ is made. The last three terms on the right-hand-side respectively account for the conduction and diffusion of electron energy due to temperature and concentration gradients, electron energy exchanged from other energy modes and rate of energy loss due to radiation. In the case of free electrons, energy exchanges can occur through elastic and inelastic collisions with heavy particles and through chemical processes such that

$$\Omega^e = \sum_{n\in\mathcal{M}} \Omega^e_n + \Omega^e_{\mathrm{C}}. \tag{2.31}$$

### Internal energy modes conservation

Finally, the conservation of the purely internal modes energy can be written as

$$\frac{\partial}{\partial t}\left(\rho e_m\right) + \boldsymbol{\nabla}\cdot\left(\rho e_m \mathbf{u}\right) = -\nabla\cdot\mathbf{q}_m + \Omega_m + Q_{m,rad}, \qquad m\in\mathcal{M}, \tag{2.32}$$

where the last three terms are respectively accounting for the conduction and diffusion of the internal energy due to temperature and concentration gradients, energy exchanges between the mode $m$ and the others through collisional processes and, finally, energy exchanges through radiative processes. If specific vibrational temperatures are considered for each polyatomic species, separate vibrational energy conservation equations must be solved

$$\frac{\partial}{\partial t}\left(\rho Y^s e^s_{vib}\right) + \boldsymbol{\nabla}\cdot\left(\rho Y^s e^s_{vib}\mathbf{u}\right) = -\boldsymbol{\nabla}\cdot\mathbf{q}^s_{vib} + \Omega^s_{vib} + Q_{vib,rad}, \qquad s\in\mathcal{H}^p. \tag{2.33}$$

Similarly to the free electrons energy source terms, the collisional term $\Omega_m$ giving rise to energy exchanges can be written as

$$\Omega_m = \sum_{n \in \mathcal{M}} \Omega_{mn} + \Omega_{Cm}, \quad \text{with} \quad n \neq m, \tag{2.34}$$

where $\Omega_{mn}$ accounts for relaxation with translation and internal energy modes through elastic and inelastic collisions and $\Omega_{Cm}$ acts as a source or sink energy terms due to reactive collisions. Finally, in order to respect mass and energy conservation, the following relations for the energy transfer terms hold

$$\sum_{m \in \mathcal{M}} \Omega_{Cm} = 0 \quad \text{and} \quad \Omega_{mn} + \Omega_{nm} = 0, \quad m, n \in \mathcal{M}. \tag{2.35}$$

### 2.3.2 Two-Temperature model

This subsection aims to provide the physical model which will be of use to modelize thermal non-equilibrium in the scope of this thesis. The following equations are based on the non-equilibrium Navier-Stokes equations, reviewed in Sec. 2.3.1, coupled with some assumptions reducing the complexity of the model while maintaining a relatively good accuracy. These assumptions are enumerated below along with the resulting model :

1. In the continuum region, the collisional numbers of the translational and rotational modes are such that their relaxation times are way shorter than the transit time of the particles within the shock layer. Then, in the light of the discussion in Sec 2.2.1, thermal equilibrium between the two modes can be assumed. Therefore, the description of the distribution of heavy-particle translational and rotational energies can be characterised by a common temperature T

   $$T = T_{tr}^h = T_{rot}, \quad h \in \mathcal{H}, \tag{2.36}$$

   Note that in rarefied regions, due to the low density encountered at these altitudes, the depleted amount of interactions between particles can prevent translational and rotational modes from reaching their collisional number and thermal equilibrium may no longer be assumed [10, 5].

2. The distribution of the molecules vibrational energy is characterised by a single vibrational temperature. However, the assumption of a single vibrational temperature may be a strong assumption. In fact, as it will be discussed in Sec. 2.5, the dissociation mechanism can be dictated by the Park's model which is based on an average of several temperatures. In the case of the Two-Temperature model, this average includes the vibrational and the trans-rotational temperatures. Then, separate vibrational temperatures should be more appropriate as molecular oxygen dissociates faster than nitrogen for example. Therefore, a single controlling rate temperature may underestimate or overestimate the time required for molecules to dissociate leading to a faster or slower relaxation time towards equilibrium. In their work, Lee *et al.* [38] exhibit the need to use separate vibrational temperatures for $N_2$ and $O_2$ in order to describe the dissociation mechanisms.

3. It is also assumed that the vibrational and electronic energy modes as well as the translational energy of the free electrons are in equilibrium [65]. Therefore, they are characterised by a common vibrational temperature $T_V$, such that

   $$T_V = T_{vib} = T_{el} = T_{tr}^e, \tag{2.37}$$

   If only a single electron-electronic temperature is considered while retaining a separate vibrational temperature, one obtains the Three-Temperature model introduced by Lee [37]. Nevertheless, Clarey and Greendyke [22] investigated the impact of using the Two-Temperature or the Three-Temperature models on the thermochemical non-equilibrium and only very small differences were found.

4. Attempts to estimate the radiative flux assuming a Boltzmann distribution might lead to an overestimation of the latter [60]. Hence, as the treatment of the radiative source terms in the Two-Temperature model remains unclear, a practical choice is to neglect them to the rotational mode such that all radiant power is converted to vibration and electronic energy [76].
5. Finally, the flow field is assumed inviscid as the region of interest in this thesis only encompasses the shock layer without the boundary layer. Hence, the viscous stress tensor in 2.19 is neglected. Moreover, in the scope of this thesis, it has been decided to neglect conduction effects as well as species diffusion. Therefore, only the convective terms are considered, leading to the Euler equations. Implementation and investigations of the thermal non-equilibrium impact on transport properties within Argo may be the subject of future works (see Sec. 6.2). However, adaptation of the transport properties to non-equilibrium models has already been widely reviewed in the literature and can be found in [26, 52].

By applying all these assumptions on the non-equilibrium Navier-Stokes equations, the following Euler equations based on the Two-Temperature model are obtained

$$\begin{cases} \frac{\partial \rho^s}{\partial t} + \boldsymbol{\nabla} \cdot (\rho^s \mathbf{u}) & = \dot{\omega}^s, \qquad s \in \mathcal{S} \\ \frac{\partial}{\partial t}(\rho \mathbf{u}) + \boldsymbol{\nabla} \cdot (\rho \mathbf{u}\mathbf{u}) & = -\boldsymbol{\nabla} p, \\ \frac{\partial}{\partial t}(\rho E) + \boldsymbol{\nabla} \cdot (\rho H \mathbf{u}) & = 0, \\ \frac{\partial}{\partial t}(\rho e_V) + \boldsymbol{\nabla} \cdot (\rho e_V \mathbf{u}) & = -p^e \boldsymbol{\nabla} \cdot \mathbf{u} + \Omega_{vib} + \Omega_{el} + \Omega^e. \end{cases} \tag{2.38}$$

The last three coefficients present on the right-hand-side of the vibrational-electron-electronic energy modes conservation are accounting for the vibrational, electronic and free electrons energy exchange processes and are derived in 2.6.

## 2.4 Pure species thermodynamics properties

From now on, the Rigid-Rotor and Harmonic Oscillator (RRHO) model [82] will be assumed in order to compute the purely internal energy modes of a given molecule $s$. While the computation of the rotational mode is performed by treating the molecule as a rigid-rotor which constrains its moment of inertia $I^s$ to be constant, vibrational energy mode is computed by treating molecules as harmonic oscillators. Given the mixture's composition utilized in this work, a molecule is at most diatomic and therefore characterised by a single normal mode of vibration at frequency $\nu^s$. Hence, from Eq. 2.8, the partition function of a diatomic particle $s$ can be written as

$$Q^s = Q^s_{el}(T_{el}) Q^s_{rot}(T_{rot}) Q^s_{vib}(T_{vib}), \tag{2.39}$$

where the partition functions related to each mode are [2]

$$Q^s_{el}(T_{el}) = \sum_n g^s_n \exp\left(-\frac{\epsilon^s_{el}(n)}{k_B T_{el}}\right), \tag{2.40}$$

$$Q^s_{rot}(T_{rot}) = \frac{8\pi^2 I^s k_B T_{rot}}{h^2}, \tag{2.41}$$

$$Q^s_{vib}(T_{vib}) = \left[1 - \exp\left(\frac{h\nu^s}{k_B T_{vib}}\right)\right]^{-1}. \tag{2.42}$$

While the translational energy is treated classically, the energy related to any purely internal mode of a species is equal to the sum of its energy levels, yielding

$$e^s_{tr}(T^s_{tr}) = \frac{3}{2} R^s T^s_{tr}, \tag{2.43}$$

$$e^s_m(T_m) = \sum_{i \in \mathcal{E}^s_m} N^s_{i,m} \epsilon^s_{i,m} = R^s T^2_m \left[ \frac{\partial \ln(Q^s_m)}{\partial T_m} \right], \tag{2.44}$$

where $\mathcal{E}^s_m$ is the set of the pure energy levels of the mode $m$, $R^s = \mathfrak{R}/M^s$ the specific gas constant with $M^s$ the molecular mass of species $s$ and $\mathfrak{R}$ the universal gas constant. In Eq. (2.43), the exponent $s$ on the translational temperature means to differentiate the free electrons and heavy particles.

By inserting Eqs. (2.40-2.42) into Eq. (2.44), one obtains the expression of the internal energy, and by extension the enthalpy (Eq. (2.25)), of each mode. These expressions are summarized in Tab. 2.1. Note that enthalpy and energy will be equal for the purely internal modes as no pressure terms are related to them. In sight of alleviating future notations, the electronic $\theta^s_{el,n}$ and vibrational $\theta^s_{vib}$ characteristic temperatures are introduced such that

$$\theta^s_{el,n} = \frac{\epsilon^s_{el}(n)}{k_B} \quad \text{and} \quad \theta^s_{vib} = \frac{h\nu^s}{k_B}. \tag{2.45}$$

Given the enthalpy and the internal energy, evaluation of the specific heats at constant pressure and volume, for a given mode and species, can therefore be derived as

$$c^s_{p,m} = \left. \frac{\partial h^s_m(T_m)}{\partial T_m} \right|_p \quad \text{and} \quad c^s_{v,m} = \left. \frac{\partial e^s_m(T_m)}{\partial T_m} \right|_v. \tag{2.46}$$

The total specific heats at constant pressure and volume for the whole mixture are obtained as follows

$$c_p = \sum_{s \in \mathcal{S}} Y^s \left( \sum_{m \in \mathcal{M}} c^s_{p,m} \right) \quad \text{and} \quad c_v = \sum_{s \in \mathcal{S}} Y^s \left( \sum_{m \in \mathcal{M}} c^s_{v,m} \right). \tag{2.47}$$

Table 2.1: Internal energy and enthalpy of the translational, electronic, rotational and vibrational modes of diatomic particles

| $m$ | $e^s_m\,[J/kg]$ | $h^s_m\,[J/kg]$ | $c^s_{v,m}\,[J/kgK]$ | $c^s_{p,m}\,[J/kgK]$ |
|---|---|---|---|---|
| $tr$ | $\frac{3}{2}R^sT^s_{tr}$ | $\frac{5}{2}R^sT^s_{tr}$ | $\frac{3}{2}R^s$ | $\frac{5}{2}R^s$ |
| $el$ | $\frac{R^s}{Q^s_{el}} \sum_n g^s_{el} \theta^s_{el,n} \exp(\frac{-\theta^s_{el,n}}{T_{el}})$ | $e^s_{el}$ | $\partial e^s_{el}/\partial T_{el}$ | $c^s_{v,el}$ |
| $rot$ | $R^sT_{rot}$ | $e^s_{rot}$ | $R^s$ | $c^s_{v,rot}$ |
| $vib$ | $R^s\theta^s_{vib}\left[\exp(\frac{\theta^s_{vib}}{T_{vib}}) - 1\right]^{-1}$ | $e^s_{vib}$ | $R^s \left(\frac{\theta^s_{vib}}{T_{vib}}\right)^2 \frac{\exp(\theta^s_{vib}/T_{vib})}{\left(\exp(\theta^s_{vib}/T_{vib})-1\right)^2}$ | $c^s_{v,vib}$ |

The expression of the electronic contribution to the specific heats in Tab. 2.1 is left under differential form as no closed-form expression analogous to the others is possible for the electronic energy mode. Rather, the sum is usually truncated up to a maximum energy level

where values of the predeceasing levels are found through electronic spectroscopy [35] and directly inserted in the sum. For example, the evaluation of electronic energy of $O_2$ on Fig. (2.7) is computed based on the first four electronic energy levels. As we can see on Fig. (2.8), dioxygen molecule under "normal conditions" has translational and rotational energy, but no significant vibrational or electronic energy leading to constant specific heats, $c_v^{0_2} = \frac{5}{2}R^{O_2}$, $c_v^{0_2} = \frac{7}{2}R^{O_2}$ and $\gamma = c_p/c_v = 1.4$. However, as temperature increases, vibrational and then electronic energies become no longer negligible such that $c_v^{O_2}, c_p^{O_2} = f(T)$ and the gas can no longer be considered as calorically perfect.

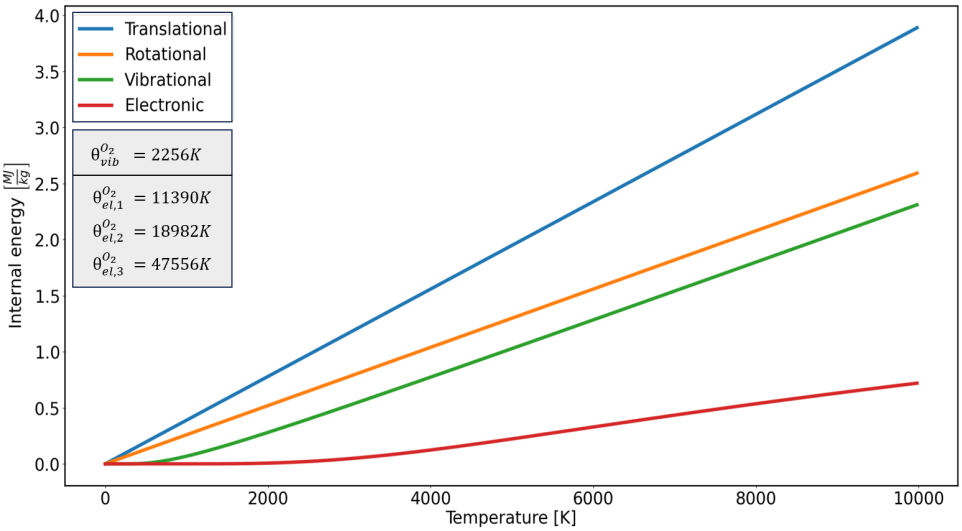


Figure 2.7: Evaluation of the internal energy modes for $O_2$ under the RRHO model. Electronic energy mode is computed based on the first four energy levels, data from [33]

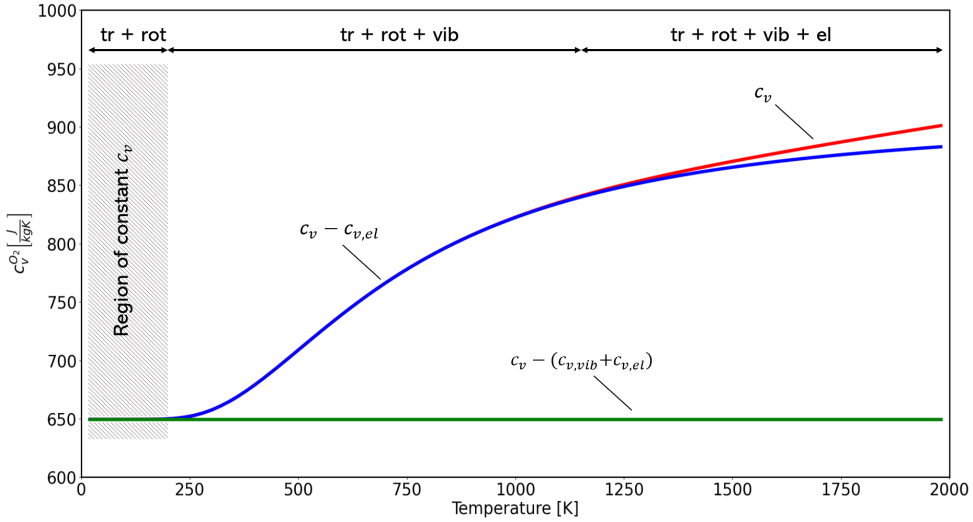


Figure 2.8: Evaluation of the specific heat at constant volume for $O_2$ under the RRHO model. Electronic energy mode is computed based on the first two energy levels, data from [33]

## 2.5 Chemical kinetic model

The very large temperatures encountered in the shock layer make the flow field very reactive and knowledge of its chemical kinetic becomes crucial as the reaction processes, such as dissociation (see Sec. 2.6), can play an important role in the energy transfer mechanisms.

### 2.5.1 Chemical source term

By considering a system of $n^{\mathcal{S}}$ species with $n^{\mathcal{R}}$ reactions such as

$$\sum_{i=1}^{n^{\mathcal{S}}} \alpha_r^s A_r^s \rightleftharpoons \sum_{i=1}^{n^{\mathcal{S}}} \beta_r^s A_r^s, \qquad s \in \mathcal{S}, \quad r \in \mathcal{R}, \tag{2.48}$$

where $A_r^s$ are the chemical species for the reaction $r$, $\alpha_r^s$ and $\beta_r^s$ are respectively the stoichiometric coefficients for reactants and products for the reaction $r$. From the law of mass-action, the chemical source term in Eq. (2.16) accounting for production rate of species $s$, is taken as the sum of the reaction sources over the $N^{\mathcal{R}}$ reactions in which the species $s$ participates in, yielding

$$\dot{\omega}^s = M^s \sum_{r=1}^{n^{\mathcal{R}}} (\beta_r^s - \alpha_r^s) \left[ k_{f,r} \prod_{i=1}^{n^{\mathcal{S}}} \left( \frac{\rho^s}{M^s} \right)^{\alpha_r^s} - k_{b,r} \prod_{i=1}^{n^{\mathcal{S}}} \left( \frac{\rho^s}{M^s} \right)^{\beta_r^s} \right], \tag{2.49}$$

where $k_{f,r}$ and $k_{b,r}$ are respectively denoting the forward and backward reaction rates of the reaction $r$. The forward reaction rate constant is assumed to follow the Arrhenius law such that

$$k_{f,r} = C_{f,r} T_{f,c}^{\eta} \exp\left( \frac{E_{a,r}}{\mathfrak{R} T_{f,c}} \right), \tag{2.50}$$

$$k_{b,r} = \frac{k_{f,r}(T_{b,c})}{K_{c,r}(T_{b,c})}, \tag{2.51}$$

where $K_{c,r}$ is the equilibrium constant for the reaction $r$, the term $T_{f,c}$ is the controlling temperature of the forward reaction while the pre-exponential parameters $C_{f,r}$ and $\eta$ and the activation energy $E_{a,r}$ are fitted usually to match experimental data.

### 2.5.2 Thermal non-equilibrium impact on chemical kinetic

In general, non-equilibrium models multiply the equilibrium rate coefficient $k_{f,r}^{eq}$ by a non-equilibrium coupling factor $\Phi$ [76] such that

$$k_{f,r}(T_{f,c}) = \Phi(T_{f,c}, T_{int}) k_{f,r}^{eq}(T_{f,c}), \tag{2.52}$$

where $T_{f,c}$ generally represents the temperature of the thermal bath which provides the energy for the reaction to proceed. For example, in the Two-Temperature model, $T_{f,c} = T$ for the heavy particles impact reactions while $T_{f,c} = T_V$ in case of electron impact reactions. The internal temperature $T_{int}$ denotes a "dummy" variable accounting for thermal nonquelibrium and may represent more than one temperature depending on the reaction's type. A summary of the important reaction types and their relative controlling temperature is proposed in Tab. 2.2. In case of equilibrium, one obtains $\Phi = 1$.

Furthermore, a special attention must be given to dissociation reactions. In fact, due to high-enthalpy flows, the characteristic times for dissociative reactions and vibrational relaxation are comparable [26]. Hence, chemical-vibrational coupling models for the dissociation's kinetic must be used in order to accurately treat non-equilibrium flows.

These models can be regrouped under two types. The first one, called *preferential* model, states that dissociation will more be more likely to occur if the molecule is at high-vibrational levels while molecules at low-lying energy levels must "ladder climb" to the higher vibrationally excited states before dissociation. Hence, distribution of the vibrational energy levels has an impact on the dissociation rate. The other type, called *non-preferential* model, considers that dissociation can occur from all vibrational levels with the same likelihood. The latter has been introduced because the ladder climbing process may not be required anymore as the dissociation energy for the molecules is much smaller than the kinetic energy of the flow under highly energetic conditions [26, 46].

Several models relying on the MT schemes exist in the literature. For example, the preferential model of Marrone and Treanor [46] relies on a coupling factor based on the vibrational partition function evaluated at a fictitious temperature $U$ such that

$$\Phi(T, T_V) = f\left(Q^s_{vib}(T), Q^s_{vib}(T_V), Q^s_{vib}(U)\right). \tag{2.53}$$

In the development of its Two-Temperature model, Park [65] proposed a simple phenomenological model which is used in this thesis. This model relies on a specific controlling rate temperature $T_P$, called the *Park temperature*, weighted with the vibrational temperature due to the preferential dissociation concept. When applied to the Arrhenius rate law in Eq. (2.50), the coupling factor is expressed as

$$\Phi(T, T_V) = \left(\frac{T_P}{T}\right)^{n_{f,r}} \exp\left[\frac{E_{a,r}}{\mathfrak{R}}\left(\frac{1}{T} - \frac{1}{T_P}\right)\right], \tag{2.54}$$

$$\text{with} \quad T_P = T^q T_V^{1-q}, \tag{2.55}$$

where the value of the exponent factor $q$ is usually taken as 0.7 or 0.5 in order to fit experimental data [14, 78] but the difference between the results obtained with the two values is negligible [29].

Table 2.2: Controlling temperature depending on the type of the chemical reaction for the Park model. Table reproduced from [15]

| Reaction type | $T_{f,c}$ | $T_{b,c}$ |
|---|---|---|
| Heavy-particle impact dissociation | $T_P$ | $T$ |
| Free-electron impact dissociation | $T_V$ | $T_V$ |
| Exchange | $T$ | $T$ |
| Charge exchange | $T$ | $T$ |
| Electron impact ionization | $T_V$ | $T_V$ |
| Associative ionization | $T$ | $T_V$ |

## 2.6 Relaxation processes

In this section, a review of the energy source terms participating in the energy transfer mechanisms is proposed. More specifically, the terms which were left under their generic formulation in Eq. 2.38 are detailed and their expressions are derived.

### 2.6.1 Vibrational energy exchange

The vibrational energy exchange can be expressed as

$$\Omega^s_{vib} := \Omega^s_{VT} + \Omega^s_{CV} = \rho^s \frac{e^s_{vib}(T) - e^s_{vib}(T_V)}{\tau^s_{VT}} + e^s_{vib}\dot{\omega}^s. \tag{2.56}$$

***Term $\Omega^s_{VT}$***

The vibrational-translational energy transfer follows a Landau-Teller formula [54, 6] where the average relaxation time in seconds is given as

$$\tau^s_{VT} = \frac{\sum_{j\in\mathcal{H}}(\rho^j/M^j)}{\sum_{j\in\mathcal{H}}\left[\rho^j/(M^j\tau^{sj}_{VT})\right]}. \tag{2.57}$$

The species relaxation time $\tau^{sj}_{VT}$ is based on semiempirical correlations proposed by Milikan and White [50, 26], valid for temperatures up to 8000K which is then coupled to the Park's correction [67] to extend the validity range for temperatures above 8000K such that

$$\tau^{js} = \tau^{js}_{MW} + \tau^{js}_{P}. \tag{2.58}$$

The contribution of Millikan and White and Park are respectively expressed as

$$\tau^{js}_{MW} = \frac{1}{p}\exp\left[1.16\times10^{-3}\sqrt{\mu^{js}}(\theta^j_{vib})^{4/3}\left(T^{-1/3} - 0.015(\mu^{js})^{1/4}\right) - 18.42\right], \tag{2.59}$$

$$\tau^{js}_{P} = \left[N^{js}\sigma^j_{vib}\sqrt{8R^sT/\pi}\right]^{-1}, \tag{2.60}$$

where $p$ is the pressure in atm, $\mu^{js} = M^sM^j/(M^s+M^j)$ is the reduced mass of species $j$ and $s$, $\theta^j_{vib}$ the characteristic vibrational temperature of species $j$, $N^{js}$ the number density of the colliding pair *(j,s)* and $\sigma^j_{vib}$ is an effective cross-section for vibrational relaxation.

***Term $\Omega^s_{CV}$***

The vibration-chemistry-vibration energy transfer due to creation or destruction of molecules through chemical reactions [15] is given as

$$\Omega^s_{CV} = \hat{D}^s\dot{\omega}^s, \tag{2.61}$$

where the coefficient $\hat{D}^s$ represents the vibrational energy of the species $s$ which is created or destroyed at rate $\dot{\omega}^s$. This coefficient can either be determined from a non-preferential or a preferential model. If the preferential model is considered, from the discussion in Sec 2.5.2, one should have that $\hat{D}^s > e^s_{vib}$ where $\hat{D}^s$ is taken as a fraction of the dissociation energy of the species $s$ [26]. However, in this thesis, the non-preferential form proposed by Candler and MacCormack [14] is used, then

$$\hat{D}^s = c_1 e^s_{vib}, \tag{2.62}$$

where the preferential factor $c_1 = 1$. If $c_1 > 1$, one obtains a simple preferential model [76].

### 2.6.2 Electronic energy exchange

The electronic energy exchange can be expressed as

$$\Omega^s_{el} := \Omega^s_{CE} = e^s_{el}\dot{\omega}^s. \tag{2.63}$$

***Term $\Omega^s_{CE}$***

Similarly to the vibration-chemistry-vibration energy transfer in Eq. (2.61), this term accounts for the electronic energy added or removed from creation or destruction of molecules through chemical reactions [62].

### 2.6.3 Free electrons energy exchange

The free electrons energy exchange can be expressed as

$$\Omega^e := \Omega^e_C + \Omega^e_T - \Omega^e_I = e^e_{tr}\dot{\omega}^e + \rho^e \frac{e^e_{tr}(T) - e^e_{tr}(T_V)}{\tau_{ET}} - \sum_{r\in\mathcal{I}} \Delta h_r \dot{\omega}^e_r, \tag{2.64}$$

**Term $\Omega^e_C$**

This term represents the production of free electrons translational energy from heavy particle collision ionization reactions. The term $\dot{\omega}^e$ denotes the production mass rate of the free electrons due to heavy particles collisions. From Tab. 2.1, the translational energy of the free electrons $e^e_{tr}$ is

$$e^e_{tr} = \frac{3}{2} R^e T^e_{tr}, \tag{2.65}$$

where $T^e_{tr} = T_V$ under the Two-Temperature model.

***Term $\Omega^e_T$***

The translation energy exchange between free electrons and heavy particles is also governed by a Landau-Teller form. From Eq. (2.65), the term $\Omega^e_T$ can be rewritten as

$$\Omega^e_T = \frac{2}{3}\rho^e R^e \frac{T - T_V}{\tau^e_{ET}}, \tag{2.66}$$

where the average relaxation time $\tau^e_{ET}$ is proportional to an effective collision frequency $\nu^{es}$ of a free-electron with a heavy particle $s \in \mathcal{H}$. Furthermore, the expression for the effective collision frequency depends on whether the particle is charged or neutral [26].

***Term $\Omega^e_I$***

Finally, this term denotes the free electrons translational energy loss during ionization of the heavy particles. Due to the large production of electrons in high enthalpy flows, tracking of their kinetic energy depletion is important. In fact, if this energy exchange is not taken into account, the surplus energy could enhance their production leading to an overestimated avalanche ionization with consequential related numerical problems [60]. The expression of the amount of energy lost amount includes $\Delta h_r$, the reaction enthalpy and $\dot{\omega}^e_r$ the electron chemical production term of the ionization reaction $r \in \mathcal{I}$. The set $\mathcal{I}$ regroups all the electron-impact ionization reactions.

## 2.7 Conclusion

The aim of this chapter was to provide the set of equations required to describe the thermo-chemical non-equilibrium phenomena occurring in high enthalpy flows.

As a first step, several energy partitioning models have been reviewed with their advantages and disadvantages. Based on this discussion, the MT scheme has been chosen due to his application to the multi-dimensional flows unlike the CR and the STS models. Then, relatively to the MT model, the non-equilibrium Navier-Stokes equations have been presented as well as the assumptions that were made to obtain the governing model considered for this thesis : the Two-Temperature Euler equations.

$$\begin{cases} \frac{\partial \rho^s}{\partial t} + \boldsymbol{\nabla} \cdot (\rho^s \mathbf{u}) & = \dot{\omega}^s, \qquad s \in \mathcal{S} \\ \frac{\partial}{\partial t}(\rho \mathbf{u}) + \boldsymbol{\nabla} \cdot (\rho \mathbf{u}\mathbf{u}) & = -\boldsymbol{\nabla} p, \\ \frac{\partial}{\partial t}(\rho E) + \boldsymbol{\nabla} \cdot (\rho H \mathbf{u}) & = 0, \\ \frac{\partial}{\partial t}(\rho e_V) + \boldsymbol{\nabla} \cdot (\rho e_V \mathbf{u}) & = -p^e \boldsymbol{\nabla} \cdot \mathbf{u} + \Omega_{vib} + \Omega_{el} + \Omega^e. \end{cases}$$

In addition, impact of the thermal non-equilibrium on the thermodynamic properties and on the chemical kinetic has been discussed. Finally, a listing of the energy transfer terms involved in the relaxation towards equilibrium, in case of the Two-Temperature model, has been proposed.

While this chapter was purely theoretical, the next chapter will provide the practical implementation of the model within Argo along with a contrast between what was already implemented or imported and the contributions of this thesis.

CHAPTER

# THREE

# NUMERICAL IMPLEMENTATION

## 3.1 Introduction

The aim of this chapter is to explain the practical implementation of the thermal non-equilibrium within Argo based on the physical model seen in Chapter 2. Another purpose of this chapter is to set the limits between what already exists in Argo and the extensions brought forward in this work. To do so, the chapter is arranged in the following manner.

In the first place, the current implementation of Argo is reviewed along with the main contributions of this work. A presentation of the Discontinuous Galerkin methods is also proposed in order to facilitate the presentation of the code's extension to thermal non-equilibrium.

Then, the library *Mutation*$^{++}$ is presented. This library is central as it provides all the thermochemical properties related to the Two-Temperature model, including the thermodynamic properties (Sec. 2.4), the chemical kinetics (Sec. 2.5) and the relaxation mechanisms (Sec. 2.6). A reformulation of the thermodynamic properties in Tab. 2.1 is also proposed to alleviate future notations specific to the Two-Temperature model.

Finally, the last section summarizes all the practical work performed in Argo allowing it to deal with thermal non-equilibrium. This section can be subdivided into two parts. The first one is dedicated to the presentation of two test codes which have been developed beside Argo (Sec. 3.4.2-3.4.1) and the other part is related to the extensions of the numerical schemes within Argo (Sec. 3.4.3).

## 3.2 Argo, a high order numerical tool

Developed at Cenaero, Argo is a multi-physics platform based on Discontinuous Galerkin methods. Written in the programming language C++, the code benefits from the polymorphism and the flexibility inherent to this language.

### 3.2.1 Current implementation and contributions of this work

As shown on Fig. 3.1, Argo is built from different blocks deserving their own purpose along with separate modules which are implemented to treat different kinds of problems. The only module of interest in this work is called *DGAblation*. This module has been developed by Schrooyen [74] during his PhD thesis and the objective was to model high enthalpy flows of several species and the presence of a reactive porous medium. While some efforts have

been proposed by Schrooyen on the discretization schemes, the main focus was to increase the fidelity of the already implemented physicochemical models. The present thesis can be seen as a continuity in the sense that the only effort was to enhance the physicochemical model by treating thermal non-equilibrium. In this perspective, no addition relating to the numerical schemes has been made, except for their extension in order to deal with thermal non-equilibrium.

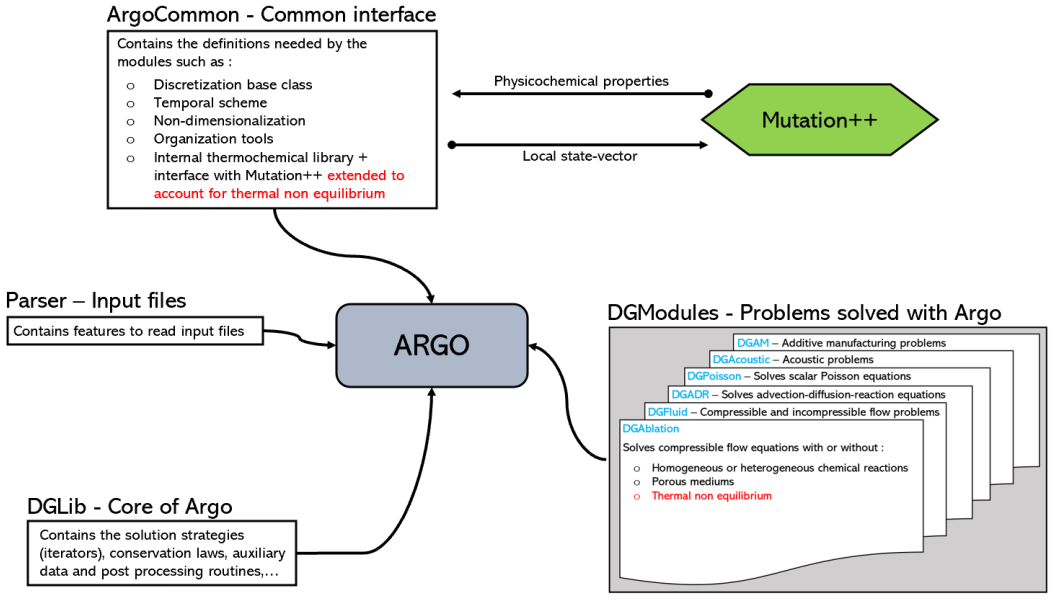


Figure 3.1: Summary of the architecture of Argo with the main contributions brought in this thesis highlighted in red. Figure modified from Schrooyen [74].

In Argo, an input file which enables the user to modify the code's execution without requiring manipulation of the core source code itself is proposed. The input file, processed by the *Parser* module, allows the characterisation of the problem such as its definition and initialisation along with the numerical integration (in time and space), flux functions, boundary conditions and especially the underlying equations themselves. A special care has thus been brought during the implementation to avoid any conflicts between the actual state of Argo and the modifications related to this work. In that way, the user is free to set the model either at thermal equilibrium or in its extended version to deal with thermal non-equilibrium simply through a True/False switch. Note that if thermal non-equilibrium is enabled, the additional inputs required for the initialisation of the problem must be specified (e.g. the initial vibrational temperature on a boundary). On the contrary, if thermal equilibrium is enabled but the user left by mistake an input specific to thermal non-equilibrium model, the code will still be able to run by overriding it.

### 3.2.2 The discontinuous Galerkin finite element method

The discontinuous Galerkin finite element methods, more commonly abbreviated to Discontinuous Galerkin (DG) methods, belong to the family of the Finite Element Methods (FEM). Let us consider a general systems of $N_{eq}$ coupled convection-diffusion-source equations such as

$$\mathcal{L}(\tilde{\mathbf{u}}) = 0, \tag{3.1}$$

$$= \frac{\partial}{\partial t} \underbrace{Q\left(\tilde{\mathbf{u}}, \mathbf{x}, t\right)}_{\substack{\text{Conserved} \\ \text{variables} \\ \text{state-vector}}} + \boldsymbol{\nabla} \cdot \underbrace{F^c\left(\tilde{\mathbf{u}}, \mathbf{x}, t\right)}_{\substack{\text{Convective} \\ \text{flux vector}}} + \boldsymbol{\nabla} \cdot \underbrace{F^d\left(\tilde{\mathbf{u}}, \boldsymbol{\nabla}\tilde{\mathbf{u}}, \mathbf{x}, t\right)}_{\substack{\text{Diffusive} \\ \text{flux vector}}} - \underbrace{S\left(\tilde{\mathbf{u}}, \boldsymbol{\nabla}\tilde{\mathbf{u}}, \mathbf{x}, t\right)}_{\substack{\text{Source} \\ \text{terms vector}}}, \tag{3.2}$$

where $\tilde{\mathbf{u}}$ is the solution state vector composed of $m$ variables with $m \in \{1, ..., N_{eq}\}$ and $\boldsymbol{\nabla}\tilde{\mathbf{u}}$ its gradients, $\mathbf{x}$ the position vector and $t$ the time. This solution state vector can also be designated as the working variables vector where these variables can be taken as the primitive ones $\mathbf{P} = (p^s, \mathbf{u}, T, T_V)^T$ or the conservative ones $\mathbf{Q} = (\rho^s, \rho\mathbf{u}, \rho E, \rho e_V)^T$. The convective flux vector $\mathbf{F}^c$ and diffusive flux vector $\mathbf{F}^d$ respectively represent the hyperbolic and elliptic subsystems.

Usually, one would need an infinite number of values to characterise the solution $\tilde{\mathbf{u}}$ of Eq. (3.1). However, this is computationally impossible. Therefore, in FEM, the solution is approximated on a finite-dimensional trial space $\mathcal{V}$ such that each variable $\tilde{u}_m$ can be approximated by a linear combination of shape functions $\Phi_j$ which form a basis for $\mathcal{V}$. This trial space $\mathcal{V}$ is constructed based on an approximation of the domain $\Omega$ by a set of geometrically simple elements $\Omega_e$ such as triangles (see Fig. 3.2) or quadrangles for domains in 2D. The approximated solution of order $p$ within each element can then be expressed as

$$\tilde{u}_m \approx u_m = \sum_{j=1}^{N_p} U_{j,m} \Phi_j, \tag{3.3}$$

where $N_p$ and $U_{j,m}$ respectively represent the total number of terms in the expansion and the coefficients of the approximation which are the degrees of freedom of the problem.

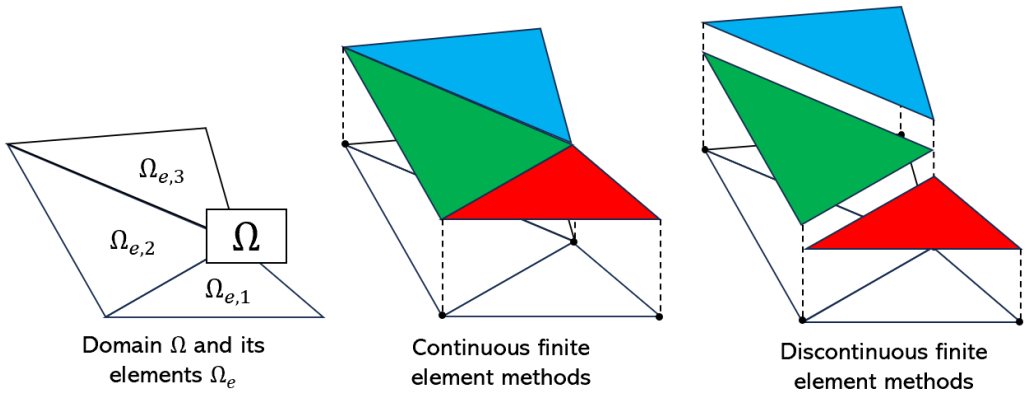


Figure 3.2: Schematic representation of continuous and discontinuous finite elements on a domain $\Omega$.

Unlike the continuous FEM, the elements in DG methods consist of vectors of functions which are fully regular within each mesh element but without any imposed continuity at their boundaries (see Fig. 3.2). This specificity allows the DG methods to be more flexible as

1. any shape functions can be supported on a single element;
2. the interpolation can change from element to element leading to local adaptation in mesh size (h-adaptation) and interpolation order $p$ (p-adaptation). Adaptive finite element methods that are capable of exploiting both are called *hp-adaptation* methods [32];
3. hybrid structured/unstructured meshes and complex geometries can be handled.

For this reason, one can associate each shape function to an element and Eq. (3.3) can be rewritten as

$$u_m = \sum_e \sum_{j=1}^{N_p^e} U_{j,m}^e \Phi_j^e, \tag{3.4}$$

where $N_p^e$ denotes the total number of terms in the expansion relatively to a specific element $e$. Several options for the definition of the shape functions exist. Within Argo, Lagrange interpolants are used and defined with respect to equidistant control points in the element [74]. Moreover, the Lagrangian polynomials are usually defined relatively to a reference or parent element $\epsilon$ through parametrical coordinates $\boldsymbol{\xi}$. This simplifies the use of unstructured sets and a mapping from parametric to physical coordinates $\mathbf{x}$ is then required (see Fig. 3.3).

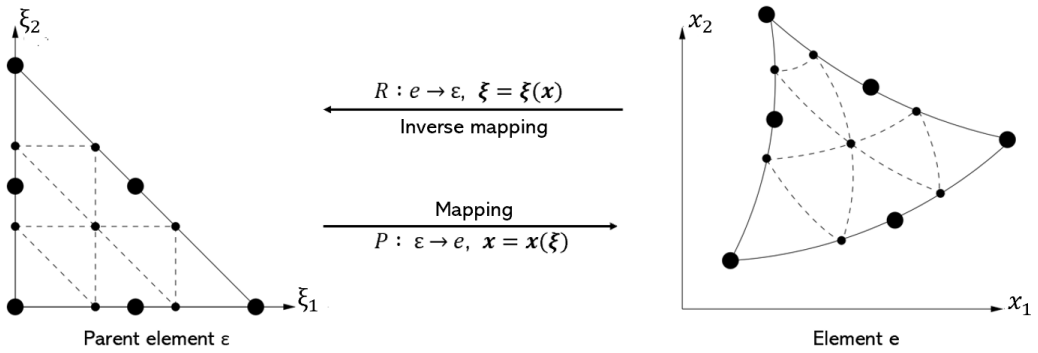


Figure 3.3: Third order mapping (small control points) of a triangle with second order interpolation (large control points). Figure taken from [30].

Another distinguishing feature of DG methods in contrast to continuous finite elements is that the discontinuity between elements leads to additional terms associated to their interfaces. As mentioned before, the resolution of Eq. (3.1) on the whole domain is not possible. Instead finite element methods require the residual of these equations, computed with the approximate solutions $u_m$, to be orthogonal to all members $v$ of a well suited test space $\mathcal{V}^*$. If the test space is the trial space itself ($\mathcal{V}^* = \mathcal{V}$), one obtains the *Galerkin variational formulation* [30] which allows to find the unknown coefficients $U_{j,m}$ of the expansion in Eq. (3.3)

$$\int_\Omega v \mathcal{L}_m(\mathbf{u}) = 0, \quad v \in \mathcal{V}. \tag{3.5}$$

By means of an elementwise decomposition and integration by parts applied on the Galerkin variational form in Eq. (3.5)[1], the weak form of Eq. (3.1) can be obtained. As the diffusive part is not considered in this work, only the hyperbolic subsystem related to the convective fluxes

[1] In this section, the term $\mathbf{u}$ is the approximate solution vector and not the velocity vector

is developed. However, complete developments and discussions for all terms are proposed in [74, 30].

$$\begin{aligned}\int_{\Omega} v\mathcal{L}_m(\mathbf{u}) = 0, \quad v \in \mathcal{V}, \quad m \in \{1,..,N_{eq}\},\\ = \sum_{\Omega_e \in \Omega} \int_{\Omega_e} v \frac{\partial}{\partial t}\left(Q_m(\mathbf{u}, x^k, t)\right) d\Omega_e - \sum_{\Omega_e \in \Omega} \int_{\Omega_e} \frac{\partial v}{\partial x^k} F_m^{c,k}(\mathbf{u}, x^k, t) d\Omega_e \\ + \sum_{I_i \in I} \oint_{I_i} [v]^k n^k \mathcal{H}_m(\mathbf{u}^+, \mathbf{u}^-, \mathbf{n}) dS - \sum_{\Omega_e \in \Omega} \int_{\Omega_e} vS(\mathbf{u}, \boldsymbol{\nabla}\mathbf{u}, x^k, t) d\Omega_e,\end{aligned} \tag{3.6}$$

where $k$ denotes the spatial coordinate, $I_i$ the interfaces between adjacent elements and the jump operator $[.]$ is such that

$$[a] = a^+ n^+ + a^- n^-. \tag{3.7}$$

The term $\mathcal{H}$ represents a numerical flux which depends on the internal interface state $\mathbf{u}^+$, on the neighbouring element interface state $\mathbf{u}^-$ and on the direction $\mathbf{n}$ normal to the interface (see Fig. 3.4). Furthermore, the numerical flux is required to satisfy the following relations [3]

$$\mathcal{H}_m(\mathbf{u}, \mathbf{u}, \mathbf{n}) = F_m^c(\mathbf{u}, \mathbf{x}, t) \cdot \mathbf{n} \quad \text{and} \quad \mathcal{H}_m(\mathbf{u}^+, \mathbf{u}^-, \mathbf{n}) = -\mathcal{H}_m(\mathbf{u}^-, \mathbf{u}^+, -\mathbf{n}), \tag{3.8}$$

which respectively represent the consistency and the conservative conditions. Several numerical flux functions satisfying the above criteria exist. In the late fifties, Godunov [28] was the first to suggest using the solution to Riemann problems at the boundaries of each cell in order to define the numerical flux. In Argo, several Riemann solvers are available going from an exact Riemann solver to approximate Riemann solvers such as the *Lax-Friedrichs* [71] and the *AUSM+up* [39] schemes. A dedicated discussion of these two solvers with their extension to the Two-Temperature model is provided in Sec. 3.4.3.

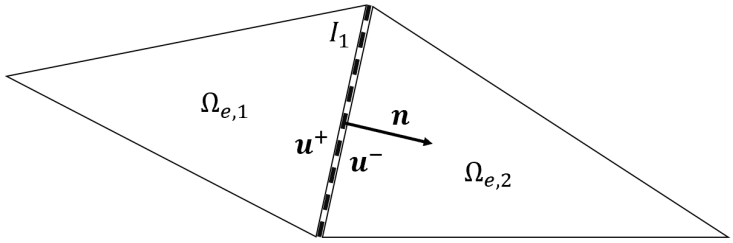


Figure 3.4: Schematic representation of two elements and their interface.

In Argo, the time discretization term in Eq. 3.6 can be handled by several explicit or implicit time stepping schemes. In this work, only the fourth order Runge-Kutta (RK44) scheme and the second order Backward Differentiation Formula (BDF2) scheme have been respectively used for the explicit and implicit schemes.

The implicit scheme gives rise to a non-linear system solved based on a Newton-Raphson algorithm which requires itself the solution of a linear system. To solve this linear system, either a direct Gauss solver or iterative methods such as the Generalized Minimal RESidual (GMRES) method are implemented in Argo. To ensure faster convergence of the iterative methods, a precondition may be required as the linear system can be badly conditioned and several methods are at disposal such as the Incomplete LU (ILU) factorization. However, these methods require the Jacobian of the problem. Therefore, the latter also had to be treated to deal with the new conservation equation of the model. As mentioned in [74], derivation of the Jacobian with respect to the primitive variables and not the conservative ones is more suitable.

Given the discretization seen in Eq. 3.6, the definition of the Jacobians require to evaluate the derivatives of the convective flux and the source terms with respect to the primitive variables.

While finite differences have been used for the source terms, the expression of the updated conservative flux is given as

$$\frac{\partial \mathbf{F}^c}{\partial \mathbf{P}} = \begin{bmatrix} \frac{\partial \rho^s \mathbf{u}}{\partial p^s} & \frac{\partial \rho^s \mathbf{u}}{\partial \mathbf{u}} & \frac{\partial \rho^s \mathbf{u}}{\partial T} & \frac{\partial \rho^s \mathbf{u}}{\partial T_V} \\ \frac{\partial (\rho \mathbf{u}\mathbf{u}+p\mathbf{I})}{\partial p^s} & \frac{\partial (\rho \mathbf{u}\mathbf{u}+p\mathbf{I})}{\partial \mathbf{u}} & \frac{\partial (\rho \mathbf{u}\mathbf{u}+p\mathbf{I})}{\partial T} & \frac{\partial (\rho \mathbf{u}\mathbf{u}+p\mathbf{I})}{\partial T_V} \\ \frac{\partial (\rho H \mathbf{u})}{\partial p^s} & \frac{\partial (\rho H \mathbf{u})}{\partial \mathbf{u}} & \frac{\partial (\rho H \mathbf{u})}{\partial T} & \frac{\partial (\rho H \mathbf{u})}{\partial T_V} \\ \frac{\partial (\rho e_V \mathbf{u})}{\partial p^s} & \frac{\partial (\rho e_V \mathbf{u})}{\partial \mathbf{u}} & \frac{\partial (\rho e_V \mathbf{u})}{\partial T} & \frac{\partial (\rho e_V \mathbf{u})}{\partial T_V} \end{bmatrix} \tag{3.9}$$

Note that the Jacobian for the diffusive fluxes is not proposed here given the physical model used in this work. Moreover, the derivation of the conversion matrix to change from primitive to conservative variables can be expressed as

$$\frac{\partial \mathbf{Q}}{\partial \mathbf{P}} = \begin{bmatrix} \frac{\partial \rho^s}{\partial p^s} & \frac{\partial \rho^s}{\partial \mathbf{u}} & \frac{\partial \rho^s}{\partial T} & \frac{\partial \rho^s}{\partial T_V} \\ \frac{\partial (\rho \mathbf{u})}{\partial p^s} & \frac{\partial (\rho \mathbf{u})}{\partial \mathbf{u}} & \frac{\partial (\rho \mathbf{u})}{\partial T} & \frac{\partial (\rho \mathbf{u})}{\partial T_V} \\ \frac{\partial (\rho E)}{\partial p^s} & \frac{\partial (\rho E)}{\partial \mathbf{u}} & \frac{\partial (\rho E)}{\partial T} & \frac{\partial (\rho E)}{\partial T_V} \\ \frac{\partial (\rho e_V)}{\partial p^s} & \frac{\partial (\rho e_V)}{\partial \mathbf{u}} & \frac{\partial (\rho e_V)}{\partial T} & \frac{\partial (\rho e_V)}{\partial T_V} \end{bmatrix}, \tag{3.10}$$

In order to verify the correct extension of the Jacobians within the code, results have been compared to the ones obtained with finite differences.

Finally, the weak formulation obtained above can be easily integrated by applying the mapping procedure and then using a Gauss-Legendre quadrature over each element and on their edges. The points and the weights are defined on the reference element and a transformation matrix is used to integrate on the physical element, giving the wanted approximated solution $\mathbf{u} \approx \tilde{\mathbf{u}}$ of the problem.

## 3.3 The Mutation++ library

*Mutation*$^{++}$ is an open source library developed by Scoggins *et al.* [77]. The goal of this library is to provide accurate and efficient computation of physicochemical properties associated with partially ionized gases in various degrees of thermal non-equilibrium given a state-vector $\tilde{\mathbf{u}} = [\rho^s, \rho e, \rho e_m]$. Fluxes and sources functions are closed by constitutive relations for thermodynamic, transport, and chemical properties of the gas.

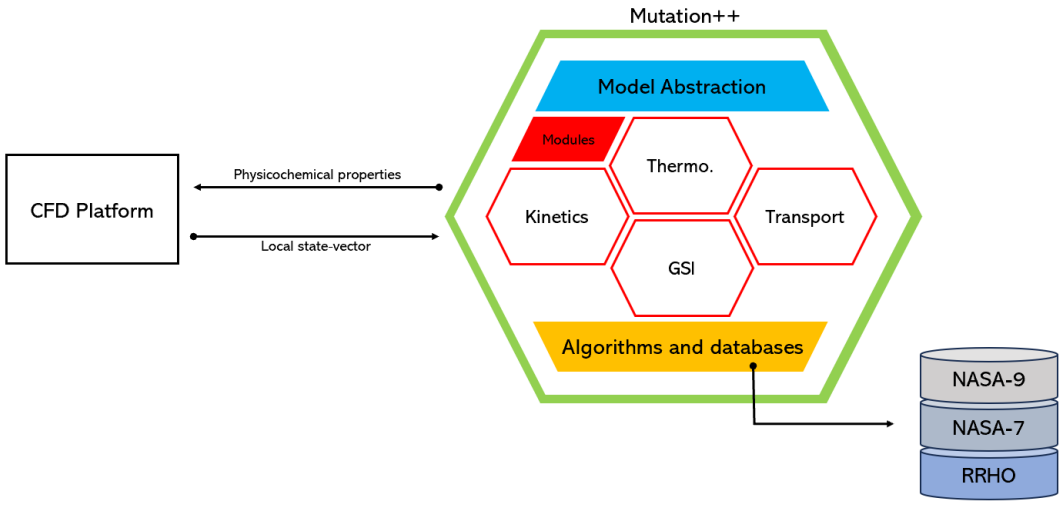


Figure 3.5: Overview of the *Mutation*$^{++}$ library and its coupling to CFD. Figure modified from Scoggins [77].

As shown on Fig. 3.5, *Mutation*$^{++}$ is composed of different modules. From the discussion in Sec. 2.3.2 neither the *Transport* module or the *Gas-Surface Interactions* (GSI) module are of use in the scope of this thesis. Considering the *Kinetics* module, its goal is provide the species production rates due to finite-rate chemical reactions as reviewed in Sec. 2.5. It has been shown that reaction mechanisms depend on the reaction type and also on the controlling rate temperature. In order to avoid the manual input of the type of every reaction in a mechanism of hundreds or thousands of reactions, *Mutation*$^{++}$ relies on a classification tree (see Fig. 3.6) which determines the type of reaction automatically when a mechanism is loaded [77].

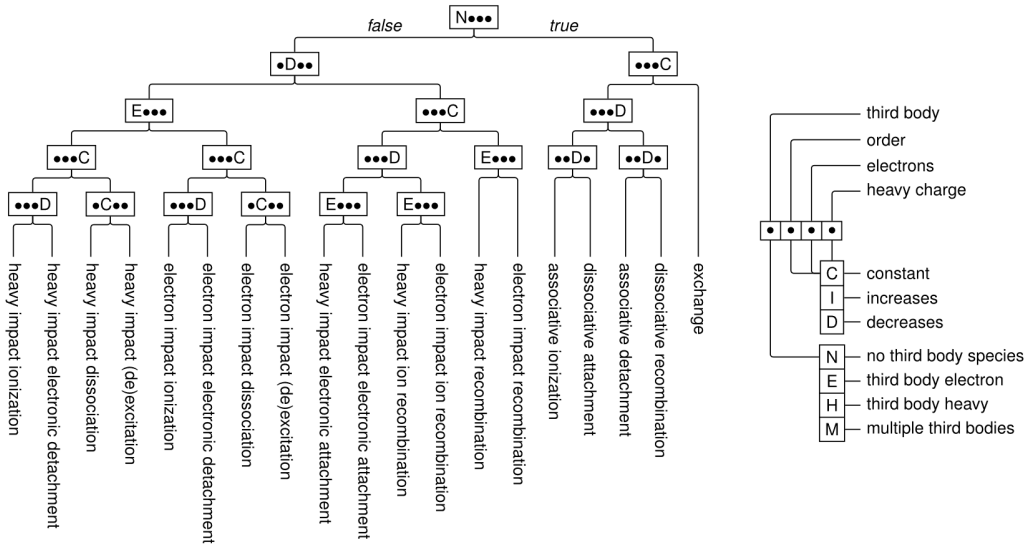


Figure 3.6: Example classification tree used in *Mutation*$^{++}$ for automatically determining chemical reactions. Figure taken from Scoggins [77].

```
<!-- O2 dissociation mechanism -->
<mechanism name="O2">

    <arrhenius_units A="mol,m,s,K" E="kcal,mol,K" />

    <reaction formula="O2+M=2O+M">
        <arrhenius A="2.75e13" n="-1.0" T="59500.0" />
        <M>O:3.</M>
    </reaction>

</mechanism>
```

```
<!-- N2 dissociation mechanism -->
<mechanism name="N2">

    <arrhenius_units A="mol,m,s,K" E="kcal,mol,K" />

     <!-- Park, 2001 -->
    <reaction formula="N2+M=2N+M">
        <arrhenius A="3.0E+22" n="-1.6" T="113200.0" />
        <M>N2:0.2333</M>
    </reaction>


</mechanism>
```

Figure 3.7: Example of a XML file describing the dissociation mechanism of molecular oxygen and nitrogen

The mechanisms are provided through XML files where each reaction composing the wanted mechanism are listed. For example, the XML files related to the mechanism describing molecular oxygen and nitrogen dissociation are given in Fig. 3.7. Finally, the *Thermodynamics* module returns the pure species thermodynamic properties such as the enthalpy or the specific heats of each species.

In Sec. 2.4, the generic expression of these properties have been reviewed. However, under the RRHO approximation and the Two-Temperature model, the expressions for the vibrational-electron-electronic energy and enthalpy can be reduced to

$$e_V = \sum_{i=1}^{n^{\mathcal{H}^p}} Y^i e^i_{vib} + \sum_{i=1}^{n^{\mathcal{H}}} Y^i e^i_{el} + Y^e e^e_{tr}, \tag{3.11}$$

$$h_V = e_V + \frac{p^e}{\rho^e}, \tag{3.12}$$

and for the specific heats

$$c_v = \left.\frac{\partial e}{\partial T}\right|_v = \sum_{i=1}^{n^{\mathcal{H}^p}} Y^i c^i_{v,rot} + \sum_{i=1}^{n^{\mathcal{H}}} Y^i c^i_{v,tr}, \tag{3.13}$$

$$c_p = \left.\frac{\partial h}{\partial T}\right|_p = \sum_{i=1}^{n^{\mathcal{H}^p}} Y^i c^i_{v,rot} + \sum_{i=1}^{n^{\mathcal{H}}} Y^i c^i_{p,tr}, \tag{3.14}$$

$$c_{v,V} = \left.\frac{\partial e}{\partial T_V}\right|_v = \left.\frac{\partial e_V}{\partial T_V}\right|_v = \sum_{i=1}^{n^{\mathcal{H}^p}} Y^i c^i_{v,vib} + \sum_{i=1}^{n^{\mathcal{H}}} Y^i c^i_{v,el} + Y^e c^e_{v,tr}, \tag{3.15}$$

$$c_{p,V} = \left.\frac{\partial h}{\partial T_V}\right|_p = \left.\frac{\partial h_V}{\partial T_V}\right|_p = \sum_{i=1}^{n^{\mathcal{H}^p}} Y^i c^i_{v,vib} + \sum_{i=1}^{n^{\mathcal{H}}} Y^i c^i_{v,el} + Y^e c^e_{p,tr}. \tag{3.16}$$

It is recalled that the thermal baths for free-electrons and heavy particles are different under the Two-Temperature model. Therefore, the free-electrons energy is a function only of $T_V$ such that $\partial e^e/\partial T = \partial h^e/\partial T = 0$. While the RRHO model is more suitable for thermal non-equilibrium cases, two other databases for thermal equilibrium are implemented. These are the NASA-7 and NASA-9 databases and provide thermodynamic properties based on polynomial fits (unlike the RRHO model which computes these properties with analytical formulas (see Tab. 2.1)). For example, under the NASA-9 database, enthalpy is given as

$$\frac{h^s}{R^s T} = -a^i_0 T^{-2} + a^i_1 \frac{lnT}{T} + a^i_2 + \frac{a^i_3}{2} T + \frac{a^i_4}{3} T^2 + \frac{a^i_5}{4} T^3 + \frac{a^i_6}{5} T^4 + \frac{a^i_7}{T}. \tag{3.17}$$

where the coefficients of the fitting polynomials can be found in [48].

## 3.4 Thermal non-equilibrium treatment

In this section, the extension of the current implementation of Argo to deal with thermal non-equilibrium is proposed. Given the complex architecture of the code, a direct implementation and its verification would have been a challenge because of the hazardous tracking of errors in the code. To overcome this problem, two test codes providing results of reference have been used in order to compare the latest with the one obtained within Argo. The first code allows the validation of the source terms and is presented in Sec. 3.4.1 while the second one validates the convective terms and is proposed in Sec. 3.4.2. Finally in Sec. 3.4.3, the boundary conditions and the interface fluxes related to the numerical scheme are modified to take into account the vibrational temperature $T_V$.

In Chapter 2, the physical model has been proposed. From Eq. (3.1), this model can be reformulated under the conservative vectorial form as follows

$$\frac{\partial}{\partial t} Q\left(\tilde{\mathbf{u}}\right) + \boldsymbol{\nabla} \cdot F^c\left(\mathbf{Q}\right) = \mathbf{S}, \tag{3.18}$$

where $\mathbf{Q}$ denotes the conservative variables, $\tilde{\mathbf{u}}$ the solution state vector, $\mathbf{F}^c$ the convective fluxes and $\mathbf{S}$ the source terms, such that

$$\mathbf{Q} = \begin{bmatrix} \rho^s \\ \rho\mathbf{u} \\ \rho E \\ \rho e_V \end{bmatrix}, \quad \mathbf{F}^c = \begin{bmatrix} \rho^s\mathbf{u} \\ \rho\mathbf{u}\mathbf{u} + p\mathbf{I} \\ \rho H\mathbf{u} \\ \rho e_V\mathbf{u} \end{bmatrix}, \quad \mathbf{S} = \begin{bmatrix} \dot{\omega}^s \\ 0 \\ 0 \\ -p^e\boldsymbol{\nabla}\cdot\mathbf{u} + \Omega_{vib} + \Omega_{el} + \Omega^e \end{bmatrix}, \quad s \in \mathcal{S}. \tag{3.19}$$

For convenience, the primitive variables $\mathbf{P} = \left(p^s, \mathbf{u}, T, T_V\right)^T$ are chosen for the solution state vector because the expression of the convective flux as a function of the primitive variables is extremely simple.

### 3.4.1 Energy exchanges and chemical source terms

Validation of the source terms is performed through the 0D *reactor*$2T^{++}$ code which solves the Euler equations for reactive flows using the Two-Temperature model where convective terms are cancelled. Therefore, from Eq. (3.18), one obtains the following reduced conservative vectorial form

$$\frac{\partial \mathbf{Q}}{\partial t} = \mathbf{S}. \tag{3.20}$$

Based on the derivation of Magin *et al.* [44], the vectorial conservative form in Eq. (3.20) can be transformed for a thermal non-equilibrium case into a system of ordinary differential equations for the primitive variables. Then, starting from the vectorial form, the idea is to extract the primitive variables from the conservatives ones by means of chain rules applied to each conservative law. The mathematical developments are proposed in what follows.

$$\frac{\partial}{\partial t}\begin{bmatrix} \rho^s \\ \rho\mathbf{u} \\ \rho E \\ \rho e_V \end{bmatrix} = \begin{bmatrix} \dot{\omega}^s \\ 0 \\ 0 \\ \Omega_{vib} + \Omega_{el} + \Omega^e \end{bmatrix}, \quad s \in \mathcal{S}. \tag{3.21}$$

#### a. Species mass conservation

The partial density can be expressed in terms of the mass fraction and the total density such that $\rho^s = Y^s\rho$. Moreover, from the total mass conservation in Eq. (2.18), one obtains that $\partial\rho/\partial t = 0$. Hence, the species mass conservation can be rewritten as

$$\frac{\partial Y^s}{\partial t} = \frac{\dot{\omega}^s}{\rho}. \tag{3.22}$$

**b. Total energy conservation**

From the momentum conservation equation, the following development can be applied on total energy

$$\rho E = \rho\left(e + \frac{\mathbf{u}^2}{2}\right) = \rho e. \tag{3.23}$$

From the chain rule

$$\frac{\partial e}{\partial t} = \underbrace{\frac{de}{dY^s}\frac{dY^s}{dt}}_{\textit{Term I}} + \underbrace{\frac{de}{dT}\frac{dT}{dt}}_{\textit{Term II}} + \underbrace{\frac{de}{dT_V}\frac{dT_V}{dt}}_{\textit{Term III}}, \tag{3.24}$$

***Term I***

$$\frac{de}{dY^s}\frac{dY^s}{dt} = \sum_{i=1}^{n^{\mathcal{S}}} e^i \frac{dY^i}{dt} = \frac{1}{\rho}\sum_{i=1}^{n^{\mathcal{S}}} e^i \dot{\omega}^i, \tag{3.25}$$

***Term II***

$$\frac{de}{dT}\frac{dT}{dt} = \sum_{i=1}^{n^{\mathcal{S}}} Y^i \frac{de^i}{dT}\frac{dT}{dt} = \left(\sum_{i=1}^{n^{\mathcal{H}}} Y^i c^i_{v,tr} + \sum_{i=1}^{n^{\mathcal{H}^p}} Y^i c^i_{v,rot}\right)\frac{dT}{dt}. \tag{3.26}$$

***Term III***

$$\frac{de}{dT_V}\frac{dT_V}{dt} = \sum_{i=1}^{n^{\mathcal{S}}} Y^i \frac{de^i}{dT_V}\frac{dT_V}{dt} = \left(\sum_{i=1}^{n^{\mathcal{H}}} Y^i c^i_{v,el} + \sum_{i=1}^{n^{\mathcal{H}^p}} Y^i c^i_{v,vib} + Y^e c^e_{v,tr}\right)\frac{dT_V}{dt}. \tag{3.27}$$

**c. Vibrational-electron-electronic energy conservation**

Similarly to the the total energy, by applying a chain rule, it yields

$$\frac{\partial e_V}{\partial t} = \frac{de_V}{dY^s}\frac{dY^s}{dt} + \underbrace{\frac{de_V}{dT}\frac{dT}{dt}}_{=0} + \frac{de_V}{dT_V}\frac{dT_V}{dt}, \tag{3.28}$$

$$= \frac{1}{\rho}\sum_{i=1}^{n^{\mathcal{S}}} e^i_V \dot{\omega}^i + \left(\sum_{i=1}^{n^{\mathcal{H}}} Y^i c^i_{v,el} + \sum_{i=1}^{n^{\mathcal{H}^p}} Y^i c^i_{v,vib} + Y^e c^e_{v,tr}\right)\frac{dT_V}{dt}. \tag{3.29}$$

Finally, by isolating the derivative terms, the following matricial form holds

$$\begin{bmatrix} 1 & 0 & 0 \\ 0 & \rho c_v & \rho c_{v,V} \\ 0 & 0 & \rho c_{v,V} \end{bmatrix} \frac{\partial}{\partial t}\begin{bmatrix} Y^s \\ T \\ T_V \end{bmatrix} = \begin{bmatrix} \frac{\dot{\omega}^s}{\rho} \\ -\sum_{i=1}^{n^{\mathcal{S}}} e^i \dot{\omega}^i \\ \Omega_{vib} + \Omega_{el} + \Omega^e - \sum_{i=1}^{n^{\mathcal{S}}} e^i_V \dot{\omega}^i \end{bmatrix}, \tag{3.30}$$

## 3.4.2 Convective terms

In order to validate the convective terms, the solver *shocking*$2T^{++}$ has been developed. This solver is a direct extension of the one-dimensional steady state reactive Euler equations solver *shocking*++ developed by Schrooyen [74] with the possibility to treat non-equilibrium phenomena by means of the Two-Temperature model. Considering steady-state the conservative form in Eq. (3.18), can be written as

$$\boldsymbol{\nabla}\cdot\mathbf{F}^c = \mathbf{S}, \tag{3.31}$$

The procedure to obtain the system of ordinary differential equations from the partial differential ones remains the same as the one used in the previous subsection. However, the non-conservative term $-p_e \boldsymbol{\nabla} \cdot \mathbf{u}$ is discretized as a source term. In fact, from the discussion of Gnoffo in [26], Eq. (2.30) is more suitable than Eq. (2.26) as terms describing convective and dissipative processes should be expressed in conservative form while the others should be treated as source or sink terms. This allows the simplification of the expressions for eigenvalues and eigenvectors of the Jacobian of the flux vector. Then, one obtains the following 1D vectorial form

$$\frac{\partial}{\partial x}\begin{bmatrix} \rho^s u \\ \rho u^2 + p \\ \rho H u \\ \rho e_V u \end{bmatrix} = \begin{bmatrix} \dot{\omega}^s \\ 0 \\ 0 \\ -p^e \frac{\partial u}{\partial x} + \Omega_{vib} + \Omega_{el} + \Omega^e \end{bmatrix}, \quad s \in \mathcal{S}. \tag{3.32}$$

**a. Species mass conservation**

From the total mass conservation in Eq. (2.18), one obtains that $\dot{m} = \rho u$ is constant. Then,

$$\frac{\partial}{\partial x}\left(\rho^s u\right) = \frac{\partial}{\partial x}\left(Y^s \rho u\right) \implies \frac{\partial Y^s}{\partial x} = \frac{\dot{\omega}^s}{\rho u}. \tag{3.33}$$

**b. Momentum conservation**

Given the constant mass flow rate and by applying the chain rule on the pressure term, the momentum conservation equation can be rewritten as

$$\frac{\partial}{\partial x}(\rho u^2 + p) = \rho u \frac{\partial u}{\partial x} + \underbrace{\frac{dp}{dY^s}\frac{dY^s}{dx}}_{\textit{Term I}} + \underbrace{\frac{dp}{d\rho}\frac{d\rho}{dx}}_{\textit{Term II}} + \underbrace{\frac{dp}{dT}\frac{dT}{dx}}_{\textit{Term III}} + \underbrace{\frac{dp}{dT_V}\frac{dT_V}{dx}}_{\textit{Term IV}}. \tag{3.34}$$

***Term I***

From the expression of the total pressure in Eq. (2.20) and the relation of Eq. (3.33), it yields

$$\frac{dp}{dY^s}\frac{dY^s}{dx} = \left(\rho R T \sum_{i=1}^{n^{\mathcal{H}}} \frac{1}{M^i} + \frac{\rho R T_V}{M^e}\right)\frac{dY^s}{dx}, \tag{3.35}$$

$$= \frac{RT}{u}\sum_{i=1}^{n^{\mathcal{H}}} \frac{\dot{\omega}^i}{M^i} + \frac{RT_V}{u}\frac{\dot{\omega}^e}{M^e}. \tag{3.36}$$

***Term II***

From the total mass conservation, the term $\frac{d\rho}{dx}$ can be rewritten as

$$\frac{\partial}{\partial x}\left(\rho u\right) = \rho\frac{\partial u}{\partial x} + u\frac{\partial \rho}{\partial x} = 0 \implies \frac{\partial \rho}{\partial x} = -\frac{\rho}{u}\frac{\partial u}{\partial x}, \tag{3.37}$$

Then, given the fact that $\frac{dp}{d\rho} = \frac{p}{\rho}$, one obtains

$$\frac{dp}{d\rho}\frac{d\rho}{dx} = -\frac{p}{u}\frac{du}{dx}. \tag{3.38}$$

***Term III and IV***

Finally, derivatives of the total pressure with respect to both temperatures are straightforward and are given as

$$\frac{dp}{dT}\frac{dT}{dx} = \left(\rho R \sum_{i=1}^{n^{\mathcal{H}}} \frac{Y^i}{M^i}\right)\frac{dT}{dx}, \tag{3.39}$$

$$\frac{dp}{dT_V}\frac{dT_V}{dx} = \rho R \frac{Y^e}{M^e}\frac{dT_V}{dx}. \tag{3.40}$$

By injecting Eqs. (3.36-3.40) into Eq. (3.34) and by dividing the result by $RT$, the momentum conservation equation can be rewritten as

$$\begin{aligned}\left[\frac{\rho u^2}{RT} - \rho\left(\sum_{i=1}^{n^{\mathcal{H}}}\frac{Y^i}{M^i} + \frac{T_V Y^e}{T M^e}\right)\right]\frac{\partial u}{\partial x} + \left(\frac{\rho u}{T}\sum_{i=1}^{n^{\mathcal{H}}}\frac{Y^i}{M^i}\right)\frac{\partial T}{\partial x} + \left(\frac{\rho u}{T}\frac{Y^e}{M^e}\right)\frac{\partial T_V}{\partial x} = \\ -\sum_{i=1}^{n^{\mathcal{H}}}\frac{\dot{\omega}^i}{M^i} - \frac{T_V}{T}\frac{\dot{\omega}^e}{M^e}.\end{aligned} \tag{3.41}$$

**c. Total energy conservation**

Based on Eq. (2.25) and the constant mass flow rate, the total energy conservation equation can be expressed as

$$\frac{\partial}{\partial x}(\rho H u) = \rho u \frac{\partial}{\partial x}\left(h + \frac{u^2}{2}\right). \tag{3.42}$$

Then, by applying a chain rule on Eq. (3.42), one obtains the following

$$\frac{\partial}{\partial x}(\rho H u) = \rho u^2 \frac{\partial u}{\partial x} + \rho u\left(\underbrace{\frac{dh}{dY^s}\frac{dY^s}{dx}}_{Term\ I} + \underbrace{\frac{dh}{dT}\frac{dT}{dx}}_{Term\ II} + \underbrace{\frac{dh}{dT_V}\frac{dT_V}{dx}}_{Term\ III}\right). \tag{3.43}$$

***Term I***

$$\frac{dh}{dY^s}\frac{dY^s}{dx} = \sum_{i=1}^{n^{\mathcal{S}}} h^i \frac{dY^i}{dx} = \frac{1}{\rho u}\sum_{i=1}^{n^{\mathcal{S}}} h^i \dot{\omega}^i. \tag{3.44}$$

***Term II***

$$\frac{dh}{dT}\frac{dT}{dx} = \sum_{i=1}^{n^{\mathcal{S}}} Y^i \frac{dh^i}{dT}\frac{dT}{dx} = \left(\sum_{i=1}^{n^{\mathcal{H}}} Y^i c^i_{p,tr} + \sum_{i=1}^{n^{\mathcal{H}^p}} Y^i c^i_{v,rot}\right)\frac{dT}{dx}. \tag{3.45}$$

***Term III***

$$\frac{dh}{dT_V}\frac{dT_V}{dx} = \sum_{i=1}^{n^{\mathcal{S}}} Y^i \frac{dh^i}{dT_V}\frac{dT_V}{dx} = \left(\sum_{i=1}^{n^{\mathcal{H}}} Y^i c^i_{v,el} + \sum_{i=1}^{n^{\mathcal{H}^p}} Y^i c^i_{v,vib} + Y^e c^e_{p,tr}\right)\frac{dT_V}{dx}. \tag{3.46}$$

**d. Vibrational-electron-eletronic energy conservation**

Similarly to the total energy, the reasoning for the vibrational-electron-eletronic energy conservation is the following

$$\frac{\partial}{\partial x}(\rho e_V u) = \rho u\left(\underbrace{\frac{de_V}{dY^s}\frac{dY^s}{dx}}_{Term\ I} + \underbrace{\frac{de_V}{dT}\frac{dT}{dx}}_{=0} + \underbrace{\frac{de_V}{dT_V}\frac{dT_V}{dx}}_{Term\ II}\right), \tag{3.47}$$

***Term I***

$$\frac{de_V}{dY^s}\frac{dY^s}{dx} = \sum_{i=1}^{n^{\mathcal{S}}} e_V^i \frac{dY^i}{dx} = \frac{1}{\rho u}\sum_{i=1}^{n^{\mathcal{S}}} e_V^i \dot{\omega}^i. \tag{3.48}$$

***Term II***

$$\frac{de_V}{dT_V}\frac{dT_V}{dx} = \sum_{i=1}^{n^{\mathcal{H}}} Y^i \frac{de_V^i}{dT_V}\frac{dT_V}{dx} = \left(\sum_{i=1}^{n^{\mathcal{H}}} Y^i c_{v,el}^i + \sum_{i=1}^{n^{\mathcal{H}^p}} Y^i c_{v,vib}^i + Y^e c_{v,tr}^e\right)\frac{dT_V}{dx}. \tag{3.49}$$

Finally, by isolating the derivative terms, the following matricial form holds

$$\begin{bmatrix} 1 & 0 & 0 & 0 \\ 0 & \frac{\rho u^2}{RT} - \rho\left(\sum_{i=1}^{n^{\mathcal{H}}} \frac{Y^i}{M^i} + \frac{T_V Y^e}{T M^e}\right) & \frac{\rho u}{T}\sum_{i=1}^{n^{\mathcal{H}}} \frac{Y^i}{M^i} & \frac{\rho u}{T}\frac{Y^e}{M^e} \\ 0 & \rho u^2 & \rho u c_p & \rho u c_{p,V} \\ 0 & p^e & 0 & \rho u c_{v,V} \end{bmatrix} \frac{\partial}{\partial x}\begin{bmatrix} Y^s \\ u \\ T \\ T_V \end{bmatrix}$$

$$= \begin{bmatrix} \frac{\dot{\omega}^s}{\rho u} \\ -\sum_{i=1}^{n^{\mathcal{H}}} \frac{\dot{\omega}^i}{M^i} - \frac{T_V}{T}\frac{\dot{\omega}^e}{M^e} \\ -\sum_{i=1}^{n^{\mathcal{S}}} h^i \dot{\omega}^i \\ \Omega_{vib} + \Omega_{el} + \Omega^e - \sum_{i=1}^{n^{\mathcal{S}}} e_V^i \dot{\omega}^i \end{bmatrix}. \tag{3.50}$$

### 3.4.3 Interface fluxes and boundary conditions

As mentioned in Sec. 3.2.2, the DG discretization involves the solution of a Riemann problem at the boundary of each cell. It was also discussed that several approximate schemes were already implemented within Argo. However, these solvers are not extended to deal with thermal non-equilibrium. Therefore, this subsection aims to provide the two Riemann solvers which have been treated and used in this work as well as the extended boundary conditions.

**Interface fluxes**

Considering the conservative system of equations

$$\frac{\partial \mathbf{Q}}{\partial t} + \boldsymbol{\nabla}\cdot F^c(\mathbf{Q}) = 0, \tag{3.51}$$

the Lax-Friedrichs flux can be expressed as [74]

$$\mathcal{H}^{LF} = \frac{\mathbf{F}^{c,L} + \mathbf{F}^{c,R}}{2} + \frac{\lambda_{LF}}{2}\left(\mathbf{Q}^R - \mathbf{Q}^L\right) \tag{3.52}$$

where the superscripts R and L are respectively the right and left state and $\lambda_{LF}$ is the eigenvalue with the largest absolute value in the eigenvalue decomposition of the flux Jacobian $\mathbf{A}$, such that

$$\mathbf{A} = \frac{\partial}{\partial \mathbf{Q}}\left(\mathbf{F}^c\left(\mathbf{Q}\right)\right). \tag{3.53}$$

The maximum eigenvalue for the transport of multicomponent flows is $\lambda_{LF} = \bar{\mathbf{u}}\cdot\mathbf{n} \pm c^{Frozen}$, in which $\bar{\mathbf{u}}$ is the mean velocity at the interface and the exponent *Frozen* refers to the non-equilibrium state at a given composition.

During the development of the *DGAblation* module, the Lax-Friedrichs scheme was the first to be extended to multispecies flows due to its ease of implementation. In order to have first results that could be compared with the *shocking*$2T^{++}$ verification code, this scheme was extended first to deal with thermal non-equilibrium. However, the Lax-Friedrichs scheme is very dissipative leading to inaccuracies in the computations. This behaviour is due to the cut-off of the Taylor expansion the scheme is based on, giving rise to a numerical diffusive term.

Furthermore, a common critical point for standard compressible solvers appears when very low Mach number flows are encountered. In fact, the treatment of such flows leads to slow or stalled convergence due to the huge ratio of characteristic speeds and as well as errors arising from an excessive amount of numerical dissipation [79]. While the convergence problem is tied to the form of governing equations being solved [39], the accuracy problem depends on the numerical flux scheme itself. Therefore, the need of a different approach emerges in order to compute compressible flow at all speeds. This need is all the more important in the application of this work since low Mach number flows may occur due to the large sound speed resulting from the high post-shock temperatures.

To tackle this problem Liou and Steffen [41] introduce the Advection Upstream Splitting Method (AUSM). The idea behind the *AUSM+up* scheme, which is an extension of the AUSM scheme for all speed regimes, is to split the inviscid numerical flux $\mathcal{H}_I^{AUSM}$ into a convective part $\mathcal{H}_I^c$ upwinded in the flow direction and a pressure part $\mathcal{H}_I^p$ upwinded according to the acoustic properties of the flow

$$\mathcal{H}_I^{AUSM} = \mathcal{H}_I^c + \mathcal{H}_I^p, \tag{3.54}$$

$$= \dot{m}_I \boldsymbol{\Phi}_{L,R} + \mathbf{P}_I, \tag{3.55}$$

where the subscript $I$ indicates the interface of two cells and $\boldsymbol{\Phi}_{L,R}$ is a vector of quantities that are convected by the mass flux $\dot{m}_I$ and which is determined from the upstream values such that

$$\boldsymbol{\Phi}_{L,R} = \begin{cases} \boldsymbol{\Phi}_L & \text{if } \dot{m}_I > 0 \\ \boldsymbol{\Phi}_R & \text{otherwise} \end{cases}, \quad \text{with} \quad \boldsymbol{\Phi} = \left(Y^s, u, H, e_V\right)^T. \tag{3.56}$$

The mass flux at the interface $\dot{m}_I$ can be written as

$$\dot{m}_I = c_I Ma_I \begin{cases} \rho^L & \text{if } Ma_I > 0, \\ \rho^R & \text{otherwise.} \end{cases} \tag{3.57}$$

where the terms $c_I$ and $Ma_I$ respectively represent the interface sound of speed and the interface Mach number. Several manners have been proposed to define the interface sound of speed [39], notably by introducing a numerical sound of speed expressed in terms of a scaling function in order to vanish the convective terms at $Ma = 0$ [40] or simply by an average of the sound speed between the left state $a^L$ and right state $a^R$. In Argo, the interface speed of sound is defined such that a normal shock can be exactly resolved between two discontinuous states

$$c_I = min\left(\hat{c}^L, \hat{c}^R\right), \quad \text{with} \quad \hat{c} = \frac{c^{*2}}{max\left(c^*, |u|\right)}, \tag{3.58}$$

where $c^*$ is the critical speed of sound evaluated when the local Mach number is unity. Considering the interface Mach number, it can be defined as a function of the left and right state Mach numbers such that

$$Ma_I = \mathcal{M}^+\left(Ma^L\right) + \mathcal{M}^-\left(Ma^R\right) - M_p, \tag{3.59}$$

where $M_p$ is a pressure diffusion term and $M^{L,R} = u_{L,R}/c_I$. In the case of multidimensional flow, $u = \mathbf{u} \cdot \mathbf{n}$, with $\mathbf{n}$ being the unit normal vector of the interface. The split Mach numbers

$\mathcal{M}^{\pm}$ are polynomial functions of the Mach,

$$\mathcal{M}^{\pm}(Ma) = \begin{cases} 0.5\left(Ma \pm |Ma|\right) & \text{if } |Ma| \geq 1, \\ \pm 0.25\left(Ma \pm 1\right)^2 \pm \beta\left(Ma^2 - 1\right)^2 & \text{otherwise,} \end{cases}, \tag{3.60}$$

$$M_p = \frac{K_p}{f_a} max\left(1 - \sigma\left(\frac{(u^L)^2 + (u^R)^2}{2c_I^2}\right), 0\right)\frac{2(p^R - p^L)}{c_I^2(\rho^L + \rho^R)}, \tag{3.61}$$

The interface pressure $p_I$ in the pressure flux $\mathbf{P}_I = (\mathbf{0}, p_I, 0, 0)^T$ can also be defined in terms of the split Mach number functions, yielding

$$p_I = \mathcal{P}^{+}\left(Ma^L\right)p^L + \mathcal{P}^{-}\left(Ma^R\right)p^R - p_u, \tag{3.62}$$

where $p_u$ is a velocity diffusion term.

$$\mathcal{P}^{\pm}(Ma) = \begin{cases} 0.5\left(1 \pm sign(Ma)\right) & \text{if } |Ma| \geq 1, \\ \pm 0.25\left(Ma \pm 1\right)^2\left(2 \mp Ma\right) \pm \alpha Ma\left(Ma^2 - 1\right)^2 & \text{otherwise,} \end{cases}, \tag{3.63}$$

$$p_u = K_u f_a c_I (u^R - u^L)\left(\rho^L + \rho^R\right)\mathcal{P}^{+}(Ma^L)\mathcal{P}^{-}(Ma^R). \tag{3.64}$$

The values of the parameters in the expressions above are the following [39] : $K_p = \frac{1}{4}$, $K_p = \frac{3}{4}$, $\sigma = 1$, $\beta = \frac{1}{8}$ and $\alpha = \frac{3}{16}\left(-4 + 5f_a^2\right)$ where $f_a(Ma_0) = Ma_0(2 - Ma_0)$ represents a scaling factor which is dependent of a reference Mach number that will act as cut-off when the real Mach tends to zero

$$Ma_0^2 = min\left(1, max\left(\frac{(u^L)^2 + (u^R)^2}{2c_I^2}, M_{co}^2\right)\right), \tag{3.65}$$

where $M_{co}$ is the cut-off Mach number which must be manually specified.

Finally, by defining the upwinding Mach number as $Ma_I^{\pm} = 0.5(Ma_I \pm |Ma_I|)$, one can express Eq. (3.55) as

$$\mathcal{H}_I^{AUSM} = c_I\left(Ma_I^{+}\rho^L\begin{bmatrix}\Upsilon^s \\ \mathbf{u} \\ H \\ e_V\end{bmatrix}^L + Ma_I^{-}\rho^R\begin{bmatrix}\Upsilon^s \\ \mathbf{u} \\ H \\ e_V\end{bmatrix}^R\right) + \begin{bmatrix}\mathbf{0} \\ p_I \\ 0 \\ 0\end{bmatrix} \tag{3.66}$$

.

**Boundary conditions**

While the numerical fluxes provide inter-cells Dirichlet boundary conditions by exchanging the correct characteristics at their interfaces, boundary conditions must also be applied on the limits of the domain. As only the convective part is of interest in this work, weak [2] boundary conditions for inviscid flows are given. Therefore, ghost cell values are specified on the outer domain and the Riemann problem is solved on the physical boundary $I_\Gamma$ of the domain (see Fig. 3.8). Given the fact that the ghost values to be specified must be in agreement with the number of entering characteristics, the vibrational temperature is added to the already implemented types of boundary conditions in [74]. A listing of the main types for inviscid flows is summarized in Tab. 3.1.

[2] Strong form for boundary conditions in discontinuous schemes may not be ideal as it could give rise to oscillations [4]

Table 3.1: Controlling temperature depending on the type of the chemical reaction for the Park model. Table reproduced and extended from [74]

| Boundary condition type | Euler conditions |
|---|---|
| Symmetry | $\mathbf{Q}^+ = \mathbf{Q}^-$ |
| Freestream | $\mathbf{u}^-, T^-, T_V^-, Y^{s-}, p^-$ are given |
| Subsonic inlet | $\mathbf{u}^-, T^-, T_V^-, Y^{s-}$ are given and $p^+ = p^-$ |
| Subsonic outlet | $p^-$ is given, other variables taken as $\mathbf{Q}^+ = \mathbf{Q}^-$ |
| Adiabatic wall | $\mathbf{u}^-$ given, other variables taken as $\mathbf{Q}^+ = \mathbf{Q}^-$ |
| Isothermal wall | $\mathbf{u}^-, T^-$ given, other variables taken as $\mathbf{Q}^+ = \mathbf{Q}^-$ |

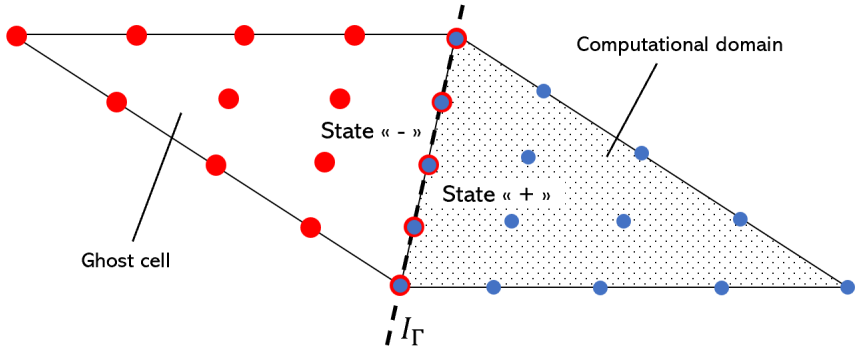


Figure 3.8: Schematic of an inner-domain boundary cell with its ghost cell. Their interface is denoted by $I_\Gamma$.

## 3.5 Conclusion

In this chapter, the implementation of the thermal non-equilibrium within Argo has been proposed. Mainly, the physical model within the *DGAblation* module as well as the numerical schemes have been upgraded to the Two-Temperature model. Furthermore, two side codes, *reactor*$2T^{++}$ and *shocking*$2T^{++}$, which allow simpler verification and validation of the outputs of Argo have been developed. In the next chapter, a practical validation of the implementation based on these codes is proposed.

CHAPTER

# FOUR

# VERIFICATION

## 4.1 Introduction

In the previous chapter, two test codes have been developed in order to verify the development of the thermal non-equilibrium implementation within Argo based on the physical model which has been presented in Chapter 2.

In this chapter, two test cases are proposed to compare the results obtained with Argo and the results of the test codes. First, the verification of the source terms based on the relaxation of a mixture in a 0D adiabatic reactor is suggested. Then, the convective terms are verified through the relaxation of a mixture behind a strong normal shock.

## 4.2 Adiabatic reactor test case

As mentioned in Chapter 3, the *reactor*$2T^{++}$ code is used in sight of verifying the implementation of the chemical source terms as well as the energy exchange terms. To do so, a pseudo 0D numerical simulation in Argo is performed on a domain represented by a nine-cell box where periodic boundary conditions are imposed on each side. The mixture, under adiabatic conditions, is initially composed of 21% oxygen and 79% nitrogen at a temperature of $10000K$ while the vibrational temperature is kept at $210K$. The mixture is then relaxed in the domain where all reaction mechanisms are listed in Tab. 4.2 and 4.1. In Argo, an explicit scheme for the time integration is chosen where the time step is taken at $10^{-6}s$ to avoid any divergence in the solution and to ensure a good accuracy of the results. As we can see on Fig. 4.1 and Fig. 4.2, the results obtained with Argo and *reactor*$2T^{++}$ seem to be in good agreement.

Furthermore, an external verification of *reactor*$2T^{++}$ based on the results obtained with the SU2-NEMO, SU2-M++ [45] and LeMANS [56] solvers has been performed. The distinction between SU2-NEMO and SU2-M++ simply resides in the use of $Mutation^{++}$ as the thermochemical library instead of the native internal library *CSU2TCLib* of SU2-NEMO. In [45], a comparison between results obtained with SU2-NEMO/M++ and LeMANS was proposed. Then, the idea was to reproduce their verification case with *reactor*$2T^{++}$.

Similarly to the one used in this thesis, their test case consisted in the relaxation of a five-species air mixture in an adiabatic reactor initially at $T = 15000K$ and $T_V = 300K$. It turned out that all models performed similarly and an equilibrium temperature of 6200K was found, 6207K for *reactor*$2T^{++}$ to be exact. Only a minor difference in the relaxation times were seen between the SU2-NEMO/M++, LeMANS and *reactor*$2T^{++}$ which may be due to the

implementations of each code. For example, the relaxation time for SU2-NEMO/M++ was $3.5e^{-7}[s]$ while equilibrium has been reached after $7.3e^{-7}[s]$ with $reactor2T^{++}$.

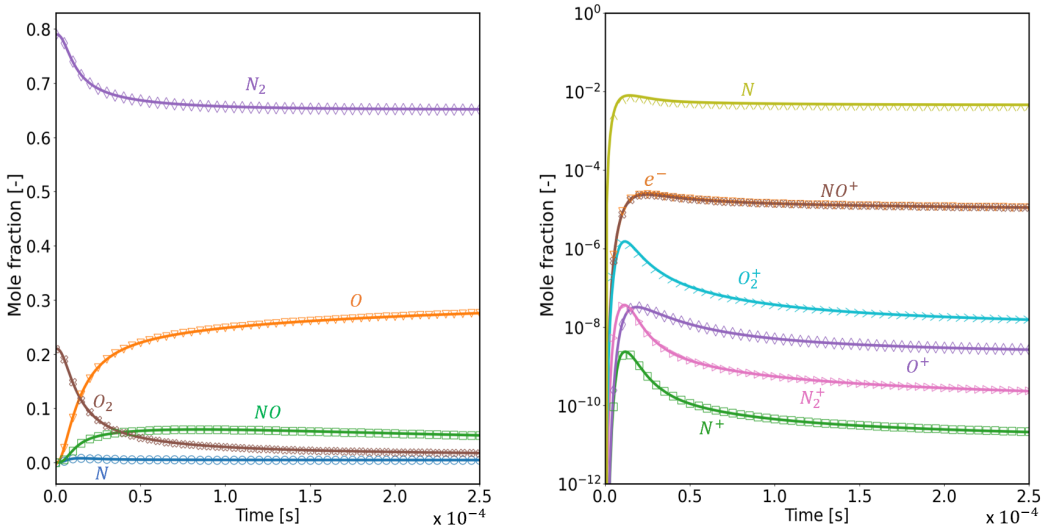


Figure 4.1: Chemical relaxation of an 11 species air mixture in an adiabatic reactor. Solid lines represent the results obtained with Argo, symbols are the results obtained with $reactor2T^{++}$.

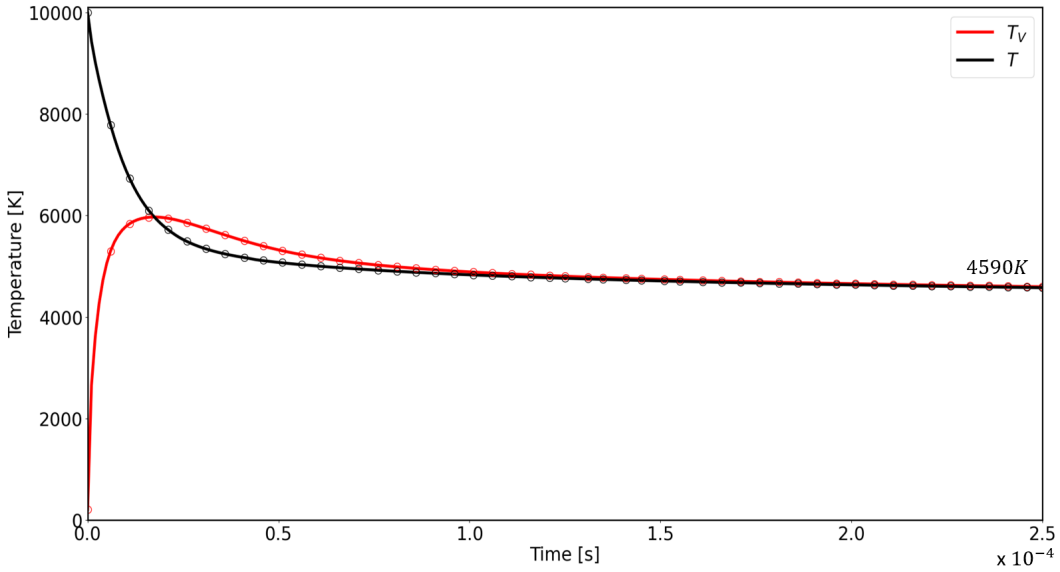


Figure 4.2: Thermal relaxation of an 11 species air mixture in an adiabatic reactor.Solid lines represent the results obtained with Argo, symbols are the results obtained with $reactor2T^{++}$.

Yet, a dissimilarity between the codes actually exists relatively to the free electrons population during the relaxation. In fact, as shown on Fig. 4.3, the follow-up of the free electrons mole fraction over time with the test code (solid red line) and with Argo (solid blue line) are different. Investigations have been performed on both codes in order to find the possible error but it was not conclusive. However, the fact that the values given by the two codes converge to the same one may put the light on the problem. In fact, one must remember

that the thermal bath for the free electrons is at the vibrational temperature and results start to converge as thermal equilibrium is occurring. Therefore, the error could emerge from the evaluation of a quantity related to the free electrons at the trans-rotational temperature $T$ and not the vibrational temperature $T_V$.

To verify this hypothesis the mole fraction of the free electrons in Argo has been multiplied by a scaling factor equal to the ratio $T/T_V$. As we can see on Fig. 4.3, a better agreement of the results between the two codes is achieved when this scaling factor is applied. This proves that the error may be due to a wrong evaluation of the free electrons in one of the codes but this error has not been found yet. However, as it will be seen in the next chapter, impact of the free electrons on the properties of the flow at the speed regimes considered in this work is almost negligible. Therefore, this error can be left behind for the moment but investigations to correct it should be done in the future.

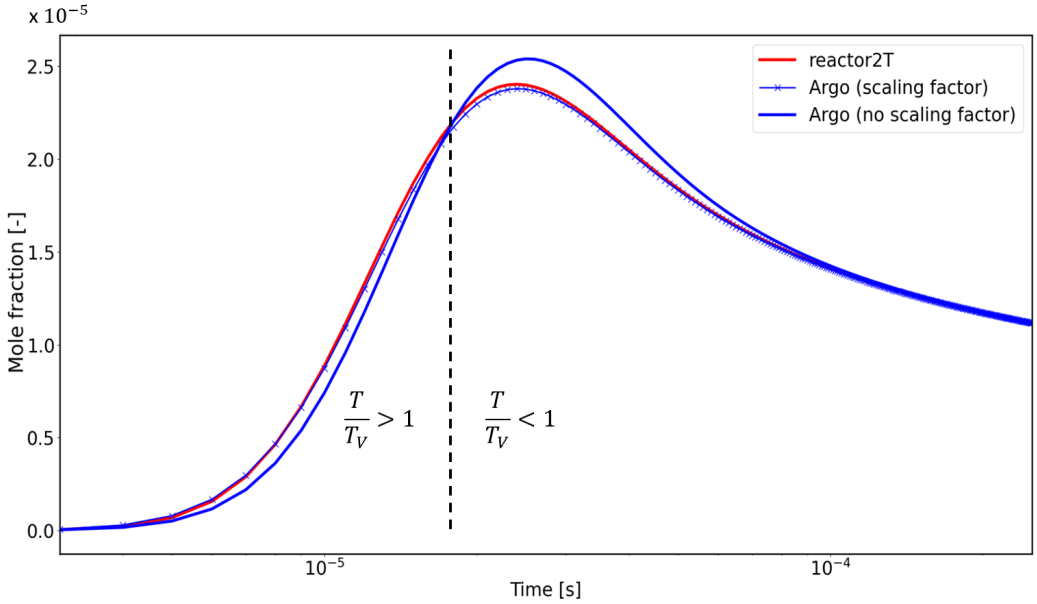


Figure 4.3: Free-electron mole fraction profile of Fig. 4.1 with and without the scaling factor.

Table 4.1: Chemical reactions used in the two verification test cases. The reactions listed below only concern the neutral heavy particles composing the atmospheric air.

| Reaction | $C_r\,[molK/s]$ | $T_a\,[K]$ | $T_c\,[K]$ | $\eta$ | Reference |
|---|---|---|---|---|---|
| Impact dissociation | | | | | |
| $O_2 + M \rightleftharpoons 2O + M$ | $2.0 \times 10^{21}$ | 59360 | $\sqrt{TT_V}$ | $-1.5$ | [68] |
| $N_2 + M \rightleftharpoons 2N + M$ | $7.0 \times 10^{21}$ | 113200 | $\sqrt{TT_V}$ | $-1.6$ | [68] |
| $NO + M \rightleftharpoons N + O + M$ | $5.0 \times 10^{15}$ | 75500 | $\sqrt{TT_V}$ | 0.0 | [66] |
| Exchange | | | | | |
| $N_2 + O \rightleftharpoons NO + N$ | $5.7 \times 10^{12}$ | 42938 | $T$ | 0.42 | [8] |
| $NO + O \rightleftharpoons O_2 + N$ | $8.4 \times 10^{12}$ | 19400 | $T$ | 0.0 | [9] |

Table 4.2: Chemical reactions used in the two verification test cases. The reactions listed below only concern the charged heavy particles and the free-electrons when a partially ionized atmospheric air is considered.

| Reaction | $C_r\,[molK/s]$ | $T_a\,[K]$ | $T_c\,[K]$ | $\eta$ | Reference |
|---|---|---|---|---|---|
| Impact dissociation | | | | | |
| $N_2 + e^- \rightleftharpoons 2N + e^-$ | $3.0 \times 10^{24}$ | 113200 | $T_V$ | $-1.6$ | [68] |
| Associative ionization | | | | | |
| $O + O \rightleftharpoons {O_2}^+ + e^-$ | $7.1 \times 10^{2}$ | 80600 | $T$ | 2.7 | [66] |
| $N + N \rightleftharpoons {N_2}^+ + e^-$ | $4.4 \times 10^{7}$ | 67500 | $T$ | 1.5 | [66] |
| $N + O \rightleftharpoons NO^+ + e^-$ | $5.3 \times 10^{12}$ | 31900 | $T$ | 0.0 | [66] |
| Charge exchange | | | | | |
| $NO^+ + O \rightleftharpoons N^+ + O_2$ | $1.0 \times 10^{12}$ | 77200 | $T$ | 0.5 | [66] |
| $N^+ + N_2 \rightleftharpoons {N_2}^+ + N$ | $1.0 \times 10^{12}$ | 12200 | $T$ | 0.5 | [66] |
| ${O_2}^+ + N \rightleftharpoons N^+ + O_2$ | $8.7 \times 10^{13}$ | 28600 | $T$ | 0.14 | [66] |
| $O^+ + NO \rightleftharpoons N^+ + O_2$ | $1.4 \times 10^{5}$ | 26600 | $T$ | 1.9 | [66] |
| ${O_2}^+ + N_2 \rightleftharpoons {N_2}^+ + O_2$ | $9.9 \times 10^{12}$ | 40700 | $T$ | 0.0 | [66] |
| ${O_2}^+ + O \rightleftharpoons O^+ + O_2$ | $4.0 \times 10^{12}$ | 18000 | $T$ | 0.09 | [66] |
| $NO^+ + N \rightleftharpoons O^+ + N_2$ | $3.4 \times 10^{13}$ | 12800 | $T$ | $-1.08$ | [66] |
| $NO^+ + O_2 \rightleftharpoons {O_2}^+ + NO$ | $2.4 \times 10^{13}$ | 32600 | $T$ | 0.41 | [66] |
| $NO^+ + O \rightleftharpoons {O_2}^+ + N$ | $7.2 \times 10^{12}$ | 48600 | $T$ | 0.29 | [66] |
| $O^+ + N_2 \rightleftharpoons {N_2}^+ + O$ | $9.1 \times 10^{11}$ | 22800 | $T$ | 0.36 | [66] |
| $NO^+ + N \rightleftharpoons {N_2}^+ + O$ | $7.2 \times 10^{13}$ | 35500 | $T$ | 0.0 | [66] |
| Impact ionization | | | | | |
| $O + e^- \rightleftharpoons O^+ + e^- + e^-$ | $3.9 \times 10^{33}$ | 158500 | $T_V$ | $-3.78$ | [68] |
| $N + e^- \rightleftharpoons N^+ + e^- + e^-$ | $2.5 \times 10^{34}$ | 168200 | $T_V$ | $-3.82$ | [68] |

## 4.3 Post-shock relaxation test case

The aim of this section is to verify the implementation of the convective terms within Argo. To do so, the test code *shocking*$2T^{++}$ presented in Sec. 3.4.2 is used on a test case consisting in the relaxation of air directly after a stationary normal shock. The numerical setup is represented in Fig. 4.4. As it will be shown in the next chapter, capturing a shock with high order interpolation methods remains a challenge in CFD and is currently unfeasible within Argo. Therefore, only the relaxation after the shock is modeled and post-shock conditions are given as the inlet boundary conditions. These conditions are derived from the Rankine-Hugoniot relations assuming thermal equilibrium, yielding

$$\rho_1 u_1 = \rho_2 u_2, \tag{4.1}$$

$$\rho_1 u_1^2 + p_1 = \rho_2 u_2^2 + p_2, \tag{4.2}$$

$$h_1 + 0.5 u_1^2 = h_2 + 0.5 u_2^2. \tag{4.3}$$

This assumption is motivated by the fact that energy transfer mechanisms do not have time to occur as the thickness of the shock is only of the order of a few mean paths of the gas molecules. For the same reason, the chemistry is also assumed frozen through the shock. Therefore, the post-shock gas composition as well as the post-shock vibrational temperature are equal to their relative pre-shock conditions. Given the strong non-linearity of the system due to the dependence of the thermodynamic properties with respect to temperature, jump

conditions are first computed from Eqs. (4.1-4.3) assuming a calorically perfect gas (cold gas approximation) and then used as initial conditions to solve the non-linear system with a Newton-Raphson algorithm (hot gas approximation). Comparison between the two approximations is summarized in Tab. 4.3. This method was already implemented in the *shocking++* code (see Sec. 3.4.2). However, in *shocking*$2T^{++}$, a feature allowing the user to chose between the cold or the hot gas approximation has been added.

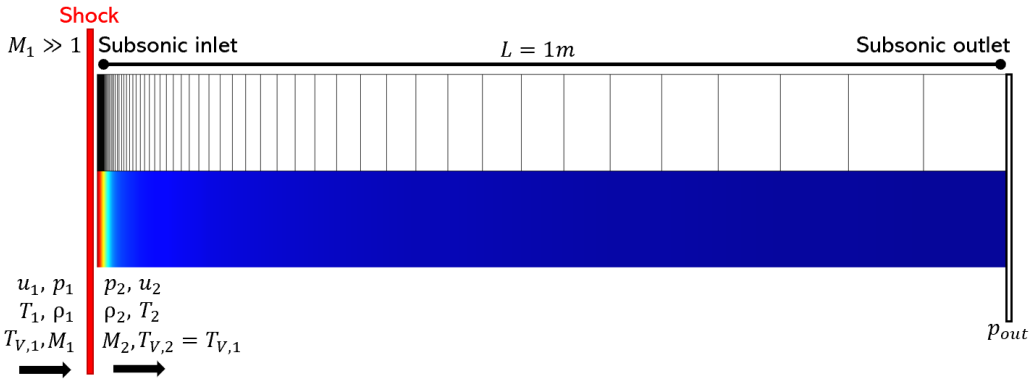


Figure 4.4: Numerical setup of the post-shock relaxation test case. The mesh and the resulting translational temperature profile are superposed.

Table 4.3: Comparison between the hot and cold gas approximations for a shock speed of 5 $[km/s]$.

| | $u\,[m/s]$ | $T\,[K]$ | $T_V\,[K]$ | $p\,[Pa]$ |
|---|---|---|---|---|
| Pre-shock conditions | 5000 | 228 | 228 | 9.75 |
| Post-shock conditions | | | | |
| Cold gas approximation | 848.38 | 12260.2 | 228 | 3089.91 |
| Hot gas approximation | 644.8 | 9773.63 | 228 | 3240.95 |

With respect to Tab. 3.1, the subsonic inlet and outlet boundary conditions are respectively characterized by the post-shock conditions and the outlet pressure $p_{out}$. To avoid the flow going backward, this pressure is taken sufficiently far away from the inlet where the system is at equilibrium. Furthermore, in order to accurately capture the thermo-chemical phenomena, the mesh is progressively refined in direction of the inlet as stronger gradients will be more likely to occur in this region.

Finally, the numerical simulation relies on second order interpolant polynomials ($p = 2$) where a three-level order sequencing has been used to hasten the computations. The order sequencing consists in progressively increasing the interpolation order where results of each level are utilized as an initial guess for the next one. This method allows better computation performances as the convergence at high orders requires less iterations (see Fig. 4.6). To illustrate that, on an *AMD Ryzen 9 6900HS*, the simulations (for this test case) with and without order sequencing on a single core respectively took 140.7$[s]$ and 242.4$[s]$.

As we can see on Fig. 4.5, a good agreement exists between Argo and *shocking*$2T^{++}$, except for the free electrons mole fraction given the same reason as the adiabatic reactor test case.

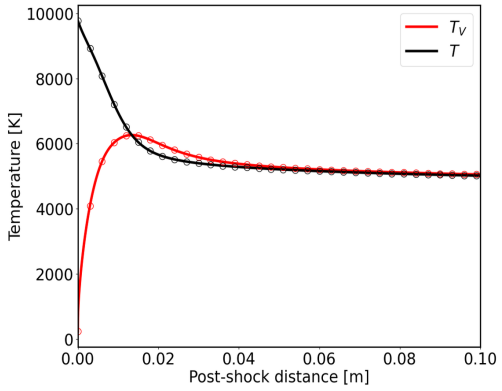


(a) Temperatures

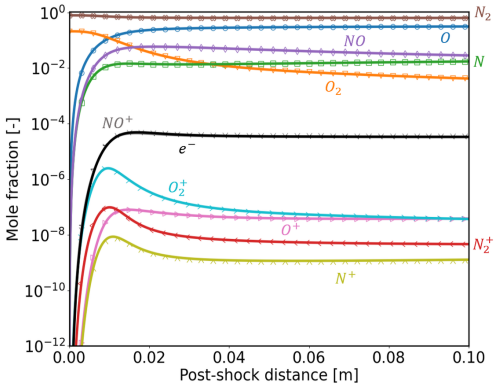


(b) Mole fractions

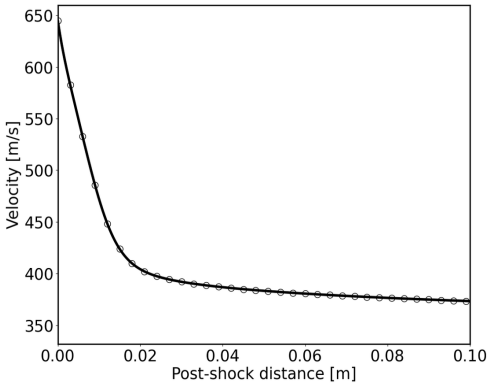


(c) Velocity

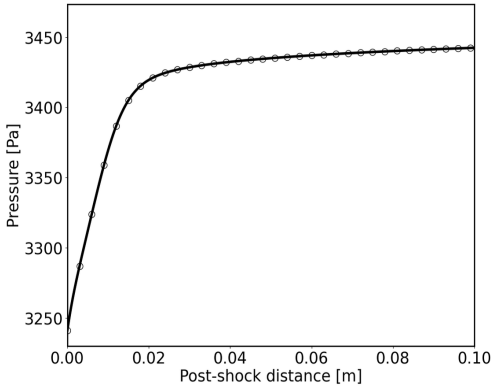


(d) Pressure

Figure 4.5: Post-shock relaxation of an 11 species air mixture, chemical reactions are listed in Tabs. 4.1 and 4.2. Solid lines represent the results obtained with Argo, symbols are the results obtained with *shocking*$2T^{++}$.

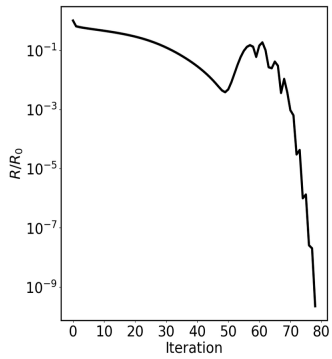


(a) Level 0 - 78 iterations

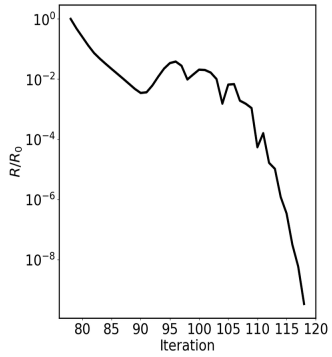


(b) Level 1 - 40 iterations

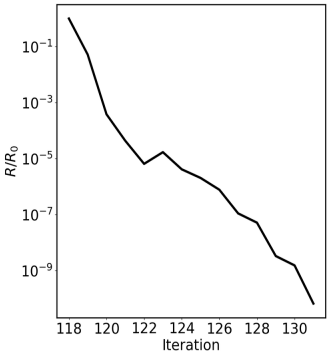


(c) Level 2 - 13 iterations

Figure 4.6: Norm of the residuals over the iterations at each level of the order sequencing. These levels are characterized by an increasing interpolation order from $p = 0$ (level 0) to $p = 2$ (level 2).

## 4.4 Conclusion

The aim of this chapter was to validate the development made within Argo by means of two separate practical test cases. The first one consisted in verifying the chemical source terms as well as the energy transfer terms through the use of the *reactor*$2T^{++}$ test code. The second one had for objective to validate the convective terms where results for comparison have been provided through the *shocking*$2T^{++}$ test code.

In both cases, good agreements between the test codes and Argo have been obtained, except for the free electrons where a dissimilarity has been observed. However, the possible source of error has been investigated and presented. Nonetheless, the error remains and further investigations should be done in the future to correct it.

In the next chapter, a discussion of the implemented model based on more complex simulations is proposed. This discussion will cover several points viewed in the past chapters such as the impact of thermal non-equilibrium in high enthalpy flows or the current limitations of capturing shocks with high order DG methods.

CHAPTER

# FIVE

# RESULTS

## 5.1 Introduction

In this chapter, the Two-Temperature model implemented within Argo will be applied to concrete applications involving thermal non-equilibrium in high enthalpy flows and is arranged as follows.

First, a comparison between the current state of Argo, where a single temperature is considered, and its extension to treat thermal non-equilibrium phenomena is proposed. For convenience, the two models will be sometimes abbreviated by the TT (Two-Temperature) and OT (One-Temperature) models. Given the restrictions emanating from the physical model in analyzing quantities such as heat fluxes or radiation terms, the study of the thermal non-equilibrium impact will be mainly focused on the chemical kinetic of the flow. To do so, the first case will consist in modeling a flow at hypersonic regime past a basic blunt body.

Then, the current limitation inherent to Argo in modeling hypersonic flows at high orders will be addressed. From this discussion, the alternative of using an adaptive mesh method to regain some of the lost accuracy due to the imposed zero-order interpolation will be proposed. Furthermore, its impact on the numerical results will be reviewed based on the modeling of an hypersonic flow around a more complex geometry : the Apollo Command Module from the AS-202 mission presented in the introduction.

Finally, an application where a high enthalpy flow at thermal non-equilibrium can be modeled at high orders will be proposed.

## 5.2 Hypersonic flow past a blunt body

### 5.2.1 Presentation of the numerical setup

As shown on Fig. 5.1, the blunt body is taken as a cylinder. Given the symmetry of the flow resulting from the inviscid model, the simulations are performed on an half domain to gain computational time.

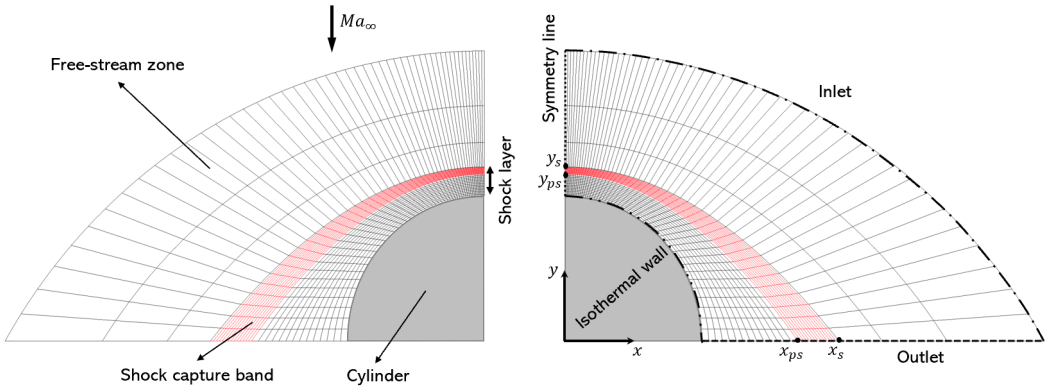


Figure 5.1: Numerical setup of the inviscid and hypersonic flow past a cylinder. Regions of the mesh are detailed on the left while the mesh parametrization is proposed on the right.

This domain can be decomposed in two main areas : the free-stream zone and the one encompassing all the shock layer. Within each zone, the number of elements and their progression in any direction are independently adjustable in order to only refine specific areas. As it will be discussed in Sec. 5.3, capturing the detached shock in front of the cylinder with high order methods is currently not possible in Argo. Therefore, all simulations in this section will be performed at a $p = 0$ interpolation order and also at steady-state.

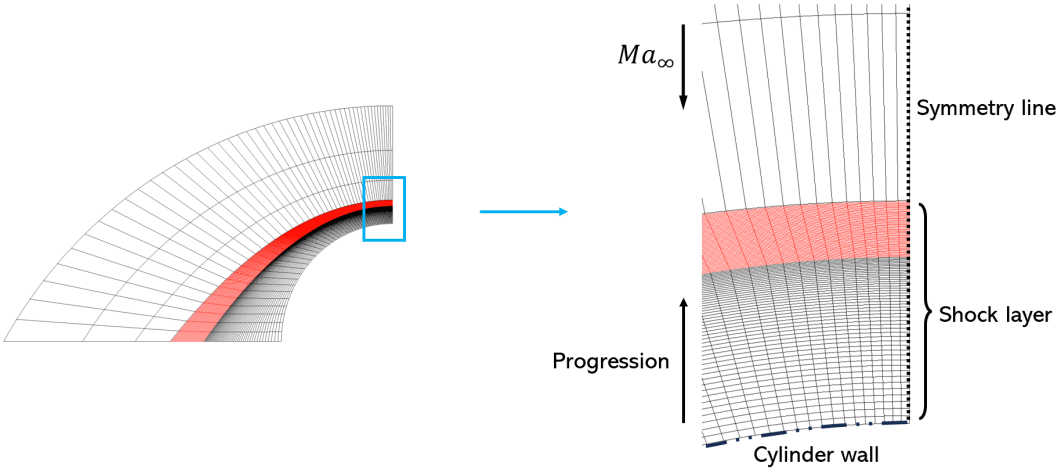


Figure 5.2: Mesh refinement strategy around the shock capture band.

To tackle the limitation in the interpolation order, the shock capture band (in red on Fig. 5.1) will be refined through an iterative process of simulations where the coordinates $[x_s, y_s]$ and $[x_{ps}, y_{ps}]$ are continuously modified in sight of only containing the shock as much as possible. For a constant number of elements in the shock capture band, this method allows to reduce their sizes permitting the shock to be captured in a more accurate fashion while limiting the computational time. Then, the rest of the shock layer is adapted based on a increasing progression of the elements towards the shock capture band to avoid strong jumps in elements size at the interface (see Fig. 5.2). Note that the free-stream region is characterised by large elements as the flow remains constant there and does not require a fine mesh.

Finally, two test cases representing two different degrees of non-equilibrium are considered. The first one is characterised by a Mach 16.5 free-stream velocity while the second one is taken at Mach 20. These test cases are respectively called *Ma16* and *Ma20*. The rest of the free-stream flow parameters are proposed in Tab. 5.1.

Table 5.1: Values of the free-stream flow parameters with respect to the *Ma16* and *Ma20* cases. $T_w$ represents the temperature at the wall of the cylinder.

| Case | $u_\infty\,[m/s]$ | $Ma_\infty\,[-]$ | $T_\infty = T_{V\infty}\,[K]$ | $p_\infty\,[Pa]$ | $T_w\,[K]$ |
|---|---|---|---|---|---|
| *Ma16* | 5000 | 16.5 | 228 | 9.75 | 300 |
| *Ma20* | 6000 | 20 | 228 | 9.75 | 300 |

### 5.2.2 Influence of the non-equilibrium phenomena on the flow properties

The aim of this subsection is to compare the results obtained when thermal non-equilibrium is considered or not for the *Ma*16 case. To begin with the comparisons, the impact of the thermal loads on the chemistry will be proposed. Then, in a second time, the position of the shock with respect to the two models will be discussed. In order to distinguish the quantities resulting from the Two-Temperature model or the One-Temperature model, the subscripts *2T* and *1T* will be respectively used.

As it will be seen later, the impact of the ionization processes on the flow properties is negligible for the *Ma16* case. Therefore, the mixture will be considered as neutral to limit the computational time of the simulations. The air is then reduced to a five species mixture such that $\mathcal{S} = \{N_2, O_2, N, O, NO\}$ where all reactional mechanisms are summarized in Tab. 4.1.

Results for the distributions of the pressure, Mach number as well as the temperatures, when thermal non-equilibrium is considered, are proposed on Fig. 5.3 and Fig. 5.4.

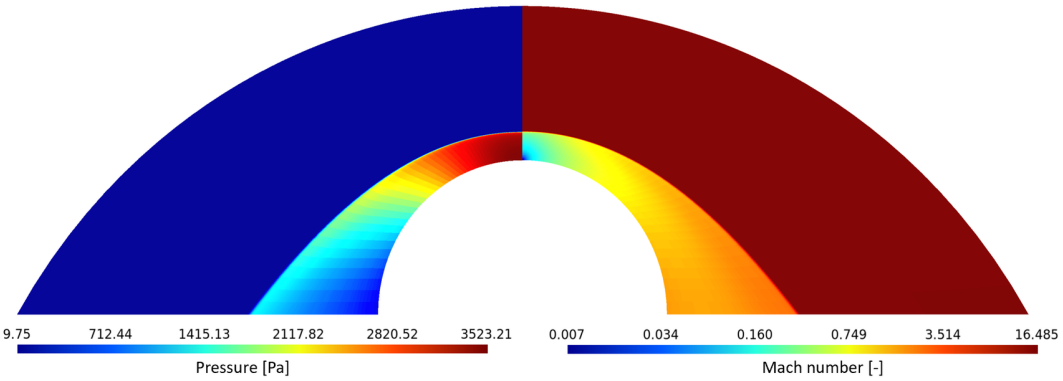


Figure 5.3: Distributions of the pressure and the Mach number around the cylinder for the *Ma*16 test case.

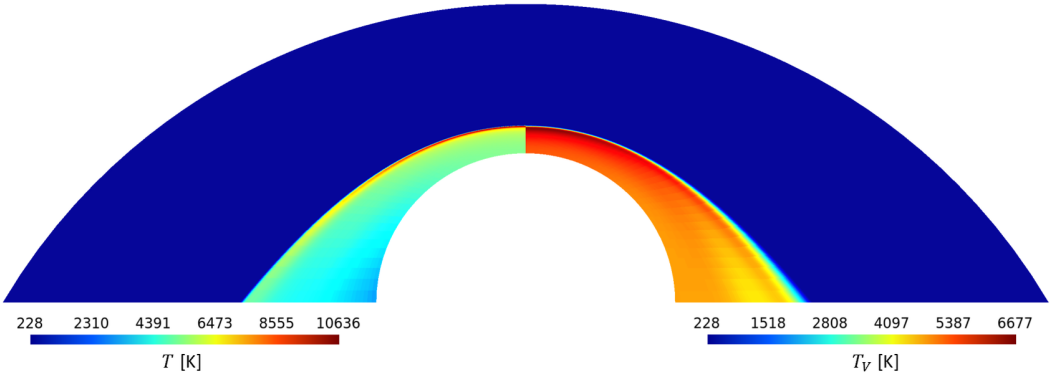


Figure 5.4: Distributions of the trans-rotational and vibrational temperatures around the cylinder for the *Ma*16 test case.

***Remark :***

Theoretically, on the stagnation line, the velocity at the cylinder's wall should be null. However, as we can see on Fig. 5.3, it is not the case. This result could be explained by the fact that the elements skirting the stagnation line are not just encompassing the latter. Indeed, it is recalled that the approximated solution is constant on each element under the $p = 0$ interpolation. Therefore, the element which is in contact of both the stagnation line and the wall, let us call it the *stagnation element*, will also experience a non-null velocity flow field leading to an overall non-null approximated velocity on this particular element. Normally, in order to have a velocity which tends to zero near the stagnation point at $p = 0$ interpolation, one should reduce the size of this stagnation element to zero such that it tends to be the stagnation point itself.

## Thermal loads impact on the chemical relaxation :

On Fig. 5.5, temperatures obtained with the Two-Temperature and One-Temperature models are compared for steady-state conditions. While all temperatures equilibrate to the same value near the wall, a strong dissimilarity is observed just after the shock between the trans-rotational temperature $T_{2T}$ and the one resulting from the One-Temperature model.

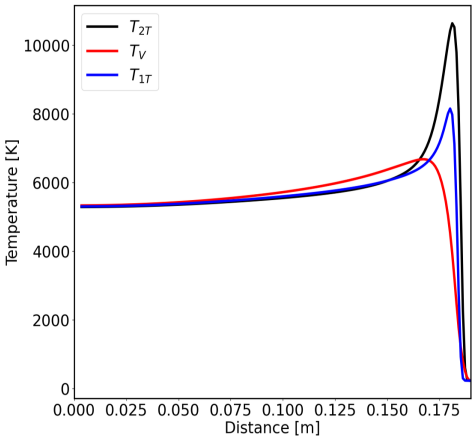


Figure 5.5: Thermal relaxation along the stagnation line for the *Ma*16 case.

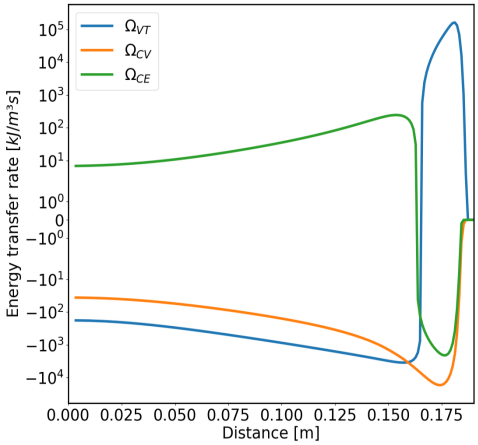


Figure 5.6: Energy transfer terms related to Two-Temperature model.

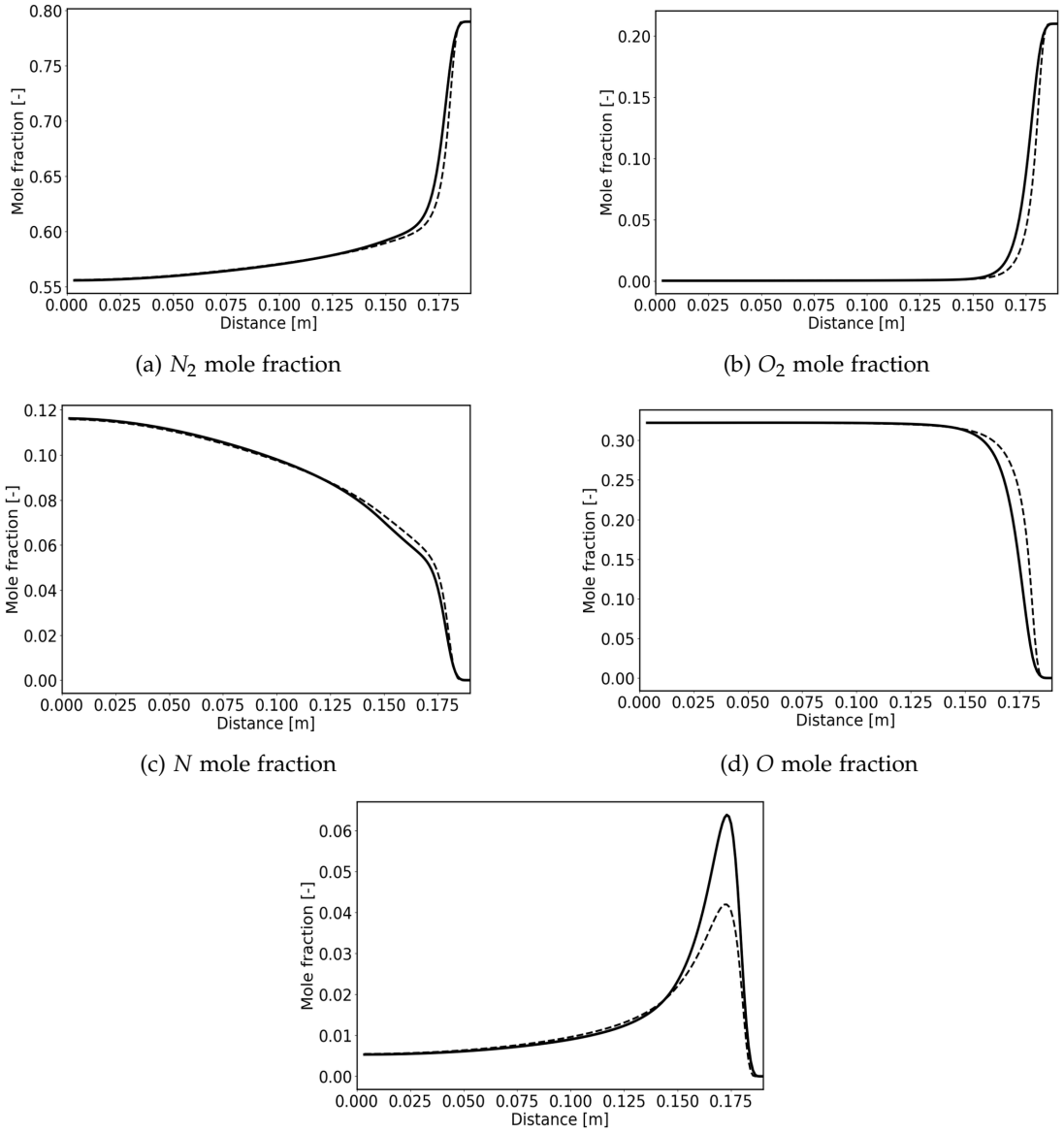


(a) $N_2$ mole fraction

(b) $O_2$ mole fraction

(c) $N$ mole fraction

(d) $O$ mole fraction

(e) $NO$ mole fraction

Figure 5.7: Chemical relaxation of a neutral mixture along the stagnation for the *Ma16* case. Results obtained with the One-Temperature and the Two-Temperature models are respectively represented by the dashed and solid lines.

As mentioned by Park in [65], the one-temperature description of the flow leads to a substantial overestimation of the rate of equilibration. A rate towards equilibrium which is, among other things, impacted by the chemical kinetic of the flow. In fact, the dissociation and exchange processes consume a lot of the internal energy of the gas which tends to decrease the post-shock temperature. At thermal equilibrium, the controlling rate temperatures $T_c$ is dictated by $T_{1T}$ itself. Therefore, the onset temperature required for the reactional mechanisms is reached faster compared to non-equilibrium model where the controlling rate temperature is defined as an average of the trans-rotational and vibrational temperatures.

The consequences of this behaviour is shown on Figs. 5.7a-5.7b where the dissociation processes for the One-Temperature model occur quicker than the ones when the thermal non-equilibrium is considered. Consequently, on Figs. 5.7c-5.7d, the production of atomic nitrogen and oxygen is also seen to be hastened. The effect of the chemical kinetic on the rate towards equilibrium can also be seen on Fig. 5.5 where the temperature $T_{1T}$ decreases in a more abrupt fashion compared to the temperature profiles of the Two-Temperature model.

On the other hand, when the TT model is considered, the controlling rate temperature for the dissociation processes is such that $T_c = \sqrt{TT_V}$. However, the vibrational temperature requires a certain amount of time to reach a sufficiently high value to allow dissociation leading to that particular offset seen above. As we can see on Fig. 5.6, this raise of vibrational temperature is caused by an abrupt excitation of the vibrational mode of the molecules through collisional processes just after the shock. These processes are mainly characterised by the energy exchange term $\Omega_{VT}$ which tends to rapidly decrease as the molecules dissociate. These events lead to a decay in the dissociation processes which allows the trans-rotational temperature $T_{2T}$ to reach higher values compared to the temperature $T_{1T}$ of the OT model.

Another impact of the disparity between the temperature profiles resides in the production of nitrogen oxide ($NO$). In fact, from Tab. 4.1, the production of this species results from an exchange process where the controlling rate temperature is equal to the trans-rotational one. Therefore, the $NO$ production is significantly increased in the non-equilibrium model in contrast to the One-Temperature model where the peak value of production is almost twice lower (see Fig. 5.7e). Note that, as discussed in [74, 8, 9], $NO$ molecules play an important role in the radiative heat flux which itself can have a large impact on the degradation of the thermal protection system.

Until now, steady-state was considered for the thermochemical relaxation which may justify the similar values in temperature and species concentrations between the One-Temperature and Two-Temperature models near the wall of the cylinder. However, this behaviour may not be the same for unsteady conditions. In fact, as the flow is establishing itself, variations of the species concentrations over time will occur at the wall, variations that will be tend to zero as the flow reaches its steady-state.

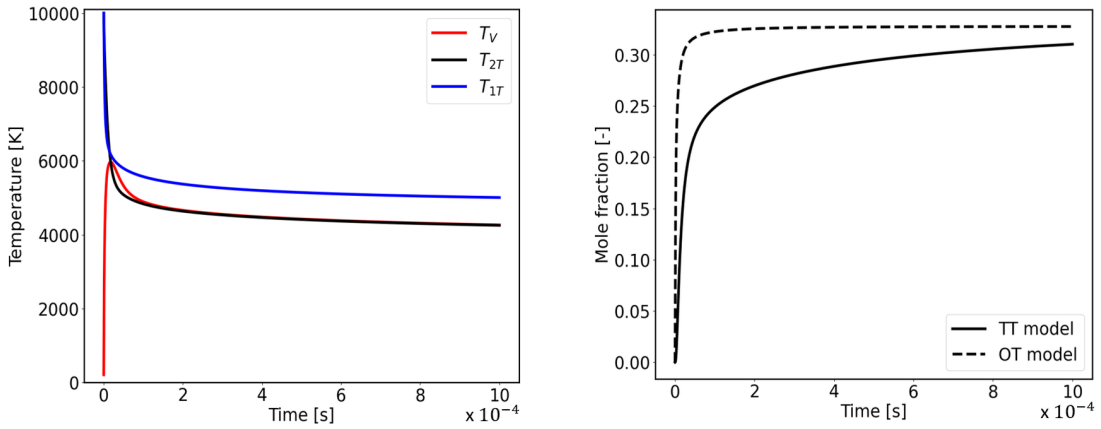


(a) Temperatures

(b) $O$ mole fraction

Figure 5.8: Results obtained with the Two-Temperature (TT) and One-Temperature (OT) models for the relaxation of a five-species air mixture in an adiabatic reactor. Only the atomic oxygen is represented for the chemical relaxation.

As we can see on Fig. 5.8, differences exist in the results between the TT and OT models for the relaxation of a five-species air mixture in an adiabatic reactor. The adiabatic reactor case

has been used given the unsteady state and only the atomic oxygen has been represented to serve as an illustration. By imagining this behaviour being convected within the shock layer, one would then obtain values in the species concentrations at the wall hat will differ between the two models at a given time.

In brief, the temporal variation of the species concentration at the wall varies depending on whether thermal non-equilibrium is considered or not. Therefore, this result reinforces the need of considering thermal non-equilibrium for ablative problems as the reactional mechanism occurring at the TPS depends on the species quantities convected at the wall by the flow (see Fig. 1.8).

### Shock standoff distance variations :

As we can see on Fig. 5.9, the distance of the shock along the stagnation line is slightly reduced when thermal equilibrium is assumed. As mentioned in [88], this standoff distance from the wall depends on many factors and can also have several relationships relatively to the flow environment.

From the theory of Wen and Hornung [85], the standoff distance $\Delta$ for a non-equilibrium flow around a sphere of diameter $D$ can be expressed as

$$\frac{\Delta}{D} = \frac{\rho_\infty}{\rho_{eq}} \left[ \frac{1}{2\tilde{\Omega}} \left( \frac{\rho_{eq}}{\rho_{sh}} - 1 \right)^2 + L \right], \tag{5.1}$$

$$= \frac{\rho_\infty}{\rho_{sh}} \frac{\rho_{sh}}{\rho_{eq}} \left[ \frac{1}{2\tilde{\Omega}} \left( \frac{\rho_\infty}{\rho_{sh}} \frac{\rho_{eq}}{\rho_\infty} - 1 \right)^2 + L \right], \quad \text{with} \quad \tilde{\Omega} = \frac{D}{u_\infty \rho_{sh}} \left( \frac{\partial \rho}{\partial t} \right) \Big|_{sh}, \tag{5.2}$$

where $\rho_{sh}$ and $\rho_{eq}$ respectively denote the densities after the shock and at the equilibrium state while $(\partial\rho/\partial t)_{sh}$ refers to the change rate of density immediately after the shock.

From Eq. 5.2, one can observe that the shock standoff distance is related to the density ratio before and after the shock $\rho_\infty/\rho_{sh}$ such that this distance increases as the ratio increases as well. In the case of the One-Temperature model, $\rho_\infty/\rho_{sh} \simeq 0.11$ while $\rho_\infty/\rho_{sh} \simeq 0.15$ for the Two-Temperature model.

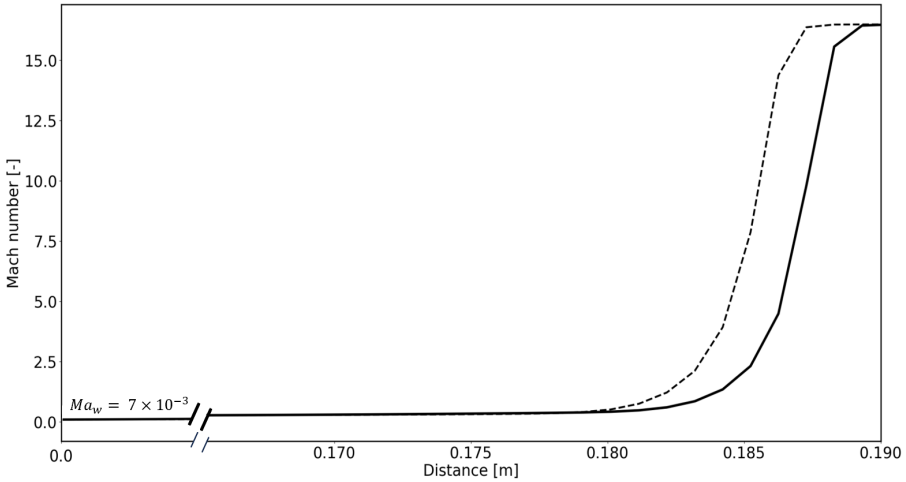


Figure 5.9: Shock standoff distance at the stagnation line with the Two-Temperature model (solid line) and the One-Temperature model (dashed line) for the *Ma16* case.

### 5.2.3 Thermal non-equilibrium impact on the ionization processes

The subject of this section will focus on the analysis of the influence of thermal non-equilibrium on the ionization processes. As the mole fractions for the neutral heavy species follow the same behaviour as the one for a neutral mixture, only the effect of thermal non-equilibrium on the ions and free electrons will be discussed here. The results proposed on Fig. 5.10 and Fig. 5.13 are respectively representing the thermal and chemical relaxations for the *Ma20* case.

As we can see on Fig. 5.10, the thermal relaxation profiles are very similar to the ones obtained in the previous subsection, except for the peak values for all temperatures due to the stronger shock occurring at Mach 20. However, new terms appear in the participation of the vibrational temperature elevation. In fact, it is recalled that the free electrons translational energy also contributes to the vibrational energy in the Two-Temperature model (see Eq. 3.11). From Sec. 2.6, these sources of kinetic energy for the free electrons (see. Fig. 5.11b) emerge from :

1. the elastic energy exchange between the free electrons and heavy particles ($\Omega^e_T$);
2. the free electrons production due to the ionization processes ($\Omega^e_C$).

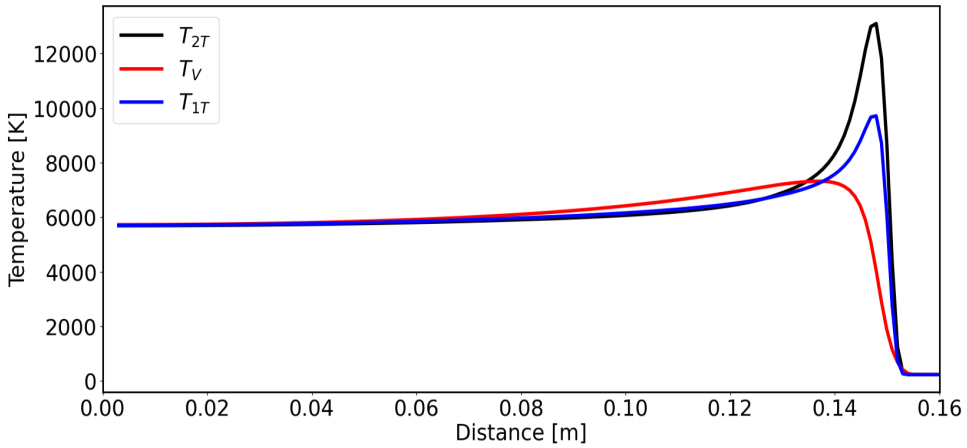


Figure 5.10: Thermal relaxation along the stagnation line for the *Ma*20 case.

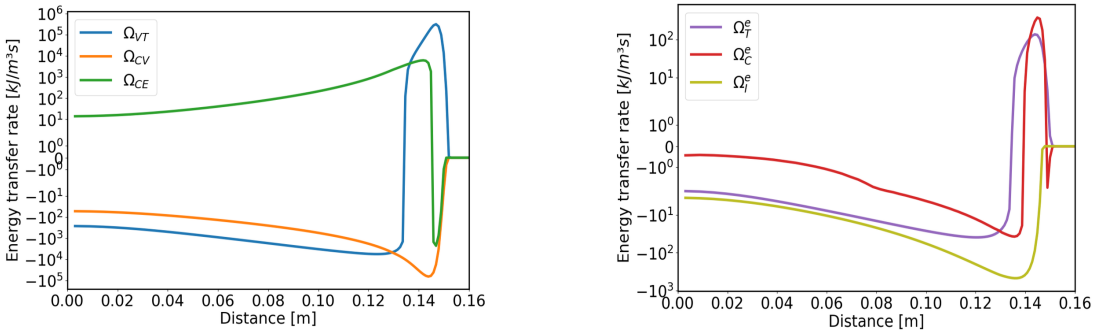


(a) Heavy particles energy transfer terms

(b) Free electrons energy transfer terms

Figure 5.11: Energy transfer terms along the stagnation line for the *Ma20* case when a partially ionized mixture is considered.

Note that the energy sink term $\Omega_I^e$ related to the free electrons translational energy loss during electron impact ionization is slightly delayed. This could be due to time needed for the free electrons to be produced, free electrons that are required for the impact ionization reactions to occur. As mentioned in Sec. 2.6, this energy exchange must be considered as the surplus energy could enhance their production leading to an overestimated avalanche ionization. Regarding the *Ma16* and the *Ma20* cases, this sink term only has a minor impact on the free electrons production. Nonetheless, for more extreme shocks, its impact is far more significant. On Fig. 5.12, a comparison of the free electrons mole fractions when $\Omega_I$ is taken into account or voluntary omitted is proposed. One can see that a complete overestimated free electrons production occurs when this term in disregarded.

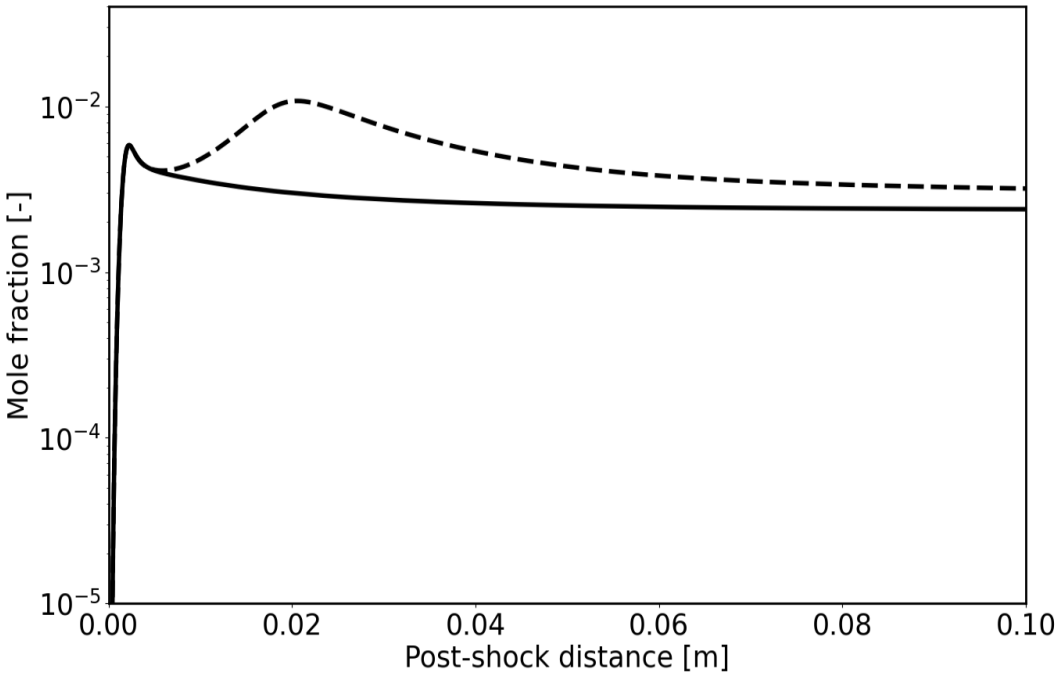


Figure 5.12: Impact of neglecting the free electrons translational energy depletion due to impact ionization mechanisms. The results are based on the *shocking*$2T^{++}$ test code where a shock speed of 11.4 $[km/s]$ has been considered.

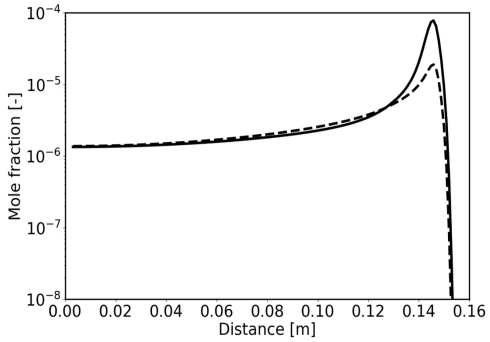


(a) $N_2^+$ mole fraction

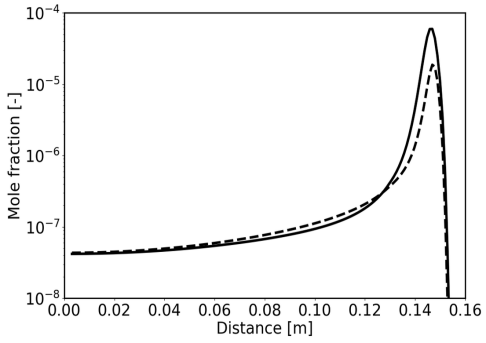


(b) $O_2^+$ mole fraction

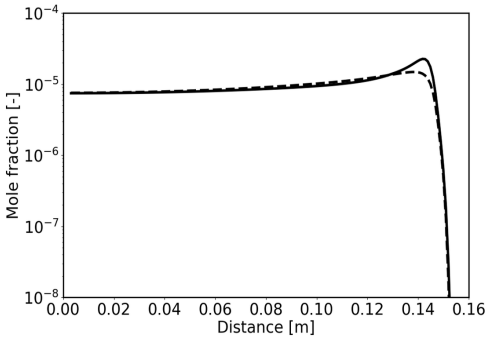


(c) $N^+$ mole fraction

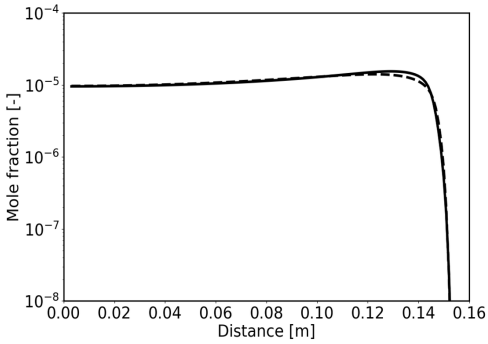


(d) $O^+$ mole fraction

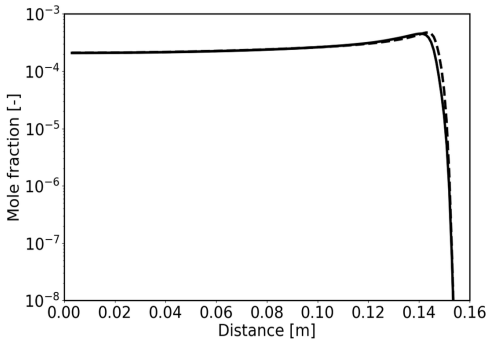


(e) $NO^+$ mole fraction

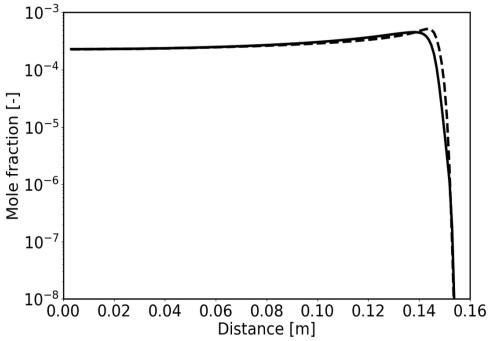


(f) $e^-$ mole fraction

Figure 5.13: Chemical relaxation of a partially ionized mixture along the stagnation for the *Ma20* case. Results obtained with the One-Temperature and the Two-Temperature models are respectively represented by the dashed and solid lines. Only the charged particles are represented.

Similarly to the enhanced production of nitric oxide, one observes higher peaks in the production of ionized species for the Two-Temperature model (see Fig. 5.13). Especially for the molecular nitrogen ions which could be explained by the numerous reactions producing it compared to the other ionized species. By looking at Tab. 4.2, the source of free electrons and ions seems to mainly emerge from associative reactions and not from impact ionization in the TT model.

This hypothesis is motivated by the fact that :

1. associative ionization reactions are controlled by the trans-rotational temperature for the TT model. A temperature which is higher than the one when for the OT model due to the dissociation mechanisms as previously explained;
2. impact ionization processes may be negligible as they are controlled by the vibrational temperature $T_V$ in the TT model.

Contrariwise, these impact ionization reactions could be the reason of the higher production of free electrons right after the shock for the One-Temperature model (see Fig. 5.13f). In fact, it is thought that their additional contribution to the free electrons production may be due to their easiest occurrence as the controlling rate temperature is not dictated by the vibrational temperature anymore.

Finally, in the light of Fig. 5.11, the assumption made in the previous subsection of only considering a neutral air mixture can be validated. In fact, the order of magnitude of the free electrons contribution to the net vibrational energy rate of creation/destruction is very small compared to the heavy species energy transfer terms ($\mathcal{O}(10^2)$ and $\mathcal{O}(10^5)$, respectively). Therefore, the impact of the ionization processes has only a minor effect on the thermochemical properties of the flow for the regimes considered in this work.

## 5.3 The high order shock capture problematic

The main purpose of this section is to address the limitation of Argo in modeling shocks at high order. A limitation that prevented us from studying the impact of the interpolation order on the simulation results obtained in the previous section.

### 5.3.1 Local order adaptation and the current limitation in shock modeling

As discussed in Sec. 3.2.2, one of the advantages of the DG methods resides in the ability to have an interpolation order which can vary locally on the domain through *p-adaptation* methods. This approach can be very useful to accurately capture phenomena only in specific areas of the flow field while saving computational resources by lowering the order everywhere else a high precision is not necessarily required.

As an illustration, one can consider the simulation of the flow past the cylinder presented in Sec. 5.2. Given the lack of interest in modeling the free-stream at high order, a $p = 0$ interpolation can be used on this part of the flow field (see Fig. 5.14). On the other hand, the high reactivity of the shock layer and the shock itself may require the utilisation of a higher interpolation order in sight of accurately capturing all phenomena. Therefore, a $p = 2$ interpolation in the shock layer can be performed based on a step function which increases the order with respect to the external boundary of the shock capture band.

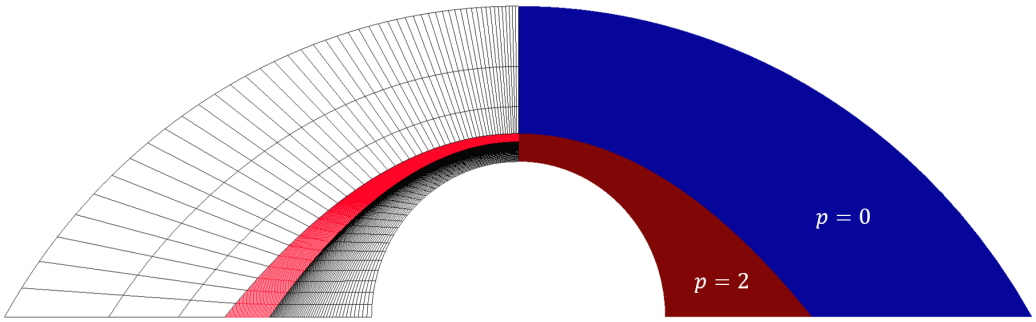


Figure 5.14: Representation of the local interpolation order adaptation.

However, the capture of sharp interfaces such as shocks in high order DG methods has always been a challenge in CFD and its insufficient resolution usually leads to Gibbs oscillations, inaccurate results, nonlinear instability and simulation breakdowns [25]. To counter this issue, a number of methods have been proposed in the literature but a complete review of these methods is out of the scope of this thesis. Therefore, only the shock capturing method based on artificial viscosity will be mentioned here.

Initially proposed by VonNeumann and Richtmeyer [84] in the early fifties, the idea behind artificial viscosity is to add dissipation close to discontinuous regions through extra viscous terms. This allows to cancel spurious oscillations by spreading the shock over a number of cells such that it can be resolved by the numerical method. For a more intensive discussion of this topic, the work proposed by Bordes [7] during his thesis is recommended. The aim of his work was to study the artificial viscosity method at disposal in Argo and to propose an improvement based on the weaknesses identified. His study was based on a several test cases such as the shock capture in supersonic wedge or the prediction of the heat flux profile at the wall of a cylinder in a supersonic flow. Unfortunately, it turned out that the shock capture at hypersonic regimes could not be handled.

In this work, several attempts have been performed in modeling the relaxation phase just after the shock at high orders while trying to capture the shock itself only at $p = 0$. The idea was to reduce the shock capture band as much as possible and then to sequence the order from $p = 0$ to $p = 2$ only in the region delimited by its internal boundary and the cylinder's wall. Nevertheless, this method showed to be inefficient due to the slight variations of the shock's position during the different phases of the order sequencing. Position variations that provoked the shock to enter in the high order area which systematically made the simulations to breakdown. The only solution was to extend the shock capture band to be assured of excluding the shock from the high order zone. However, while a part of the relaxation was successfully captured at $p = 2$, the rest was still captured at $p = 0$ which gave unsatisfactory results. This explains the choice of using a zero order interpolation on the whole domain of the simulations from the previous section.

Note that the motivation of Sec. 5.2.2 was to obtain comparative results for the One-Temperature and the Two-Temperature models. Hence, a zero order method was not really a problem as simulations of both models relied on it.

### 5.3.2 Local mesh size adaptation

From the discussion above, it has been shown that adaptive order features could not currently be applied on shock modeling in Argo such that a $p = 0$ interpolation must be used on the whole domain. But then, how could one enhance the accuracy of the results given this limitation on the interpolation order ?

In the presentation of the numerical setup in Sec. 5.2.1, the idea was to refine the areas respectively to the intensity of their gradients. More specifically, a configurable shock capture band has been proposed where the size of its elements was manually adjustable. Given the structured mesh and its simplicity, such a parametrization was quite easy. However, for unstructured meshes related to more complex geometries, a manual configuration can be very challenging and *h-adaptation* methods may turn out to be very useful.

Actually, Argo is fitted with such a method where the adaptation of the mesh size is dictated by three main user-defined parameters which specify the accuracy, location and density of the mesh refinement. These parameters are respectively represented by the minimum length of the elements, the variables used for the adaptation and the ratio of total elements before and after adaptation.

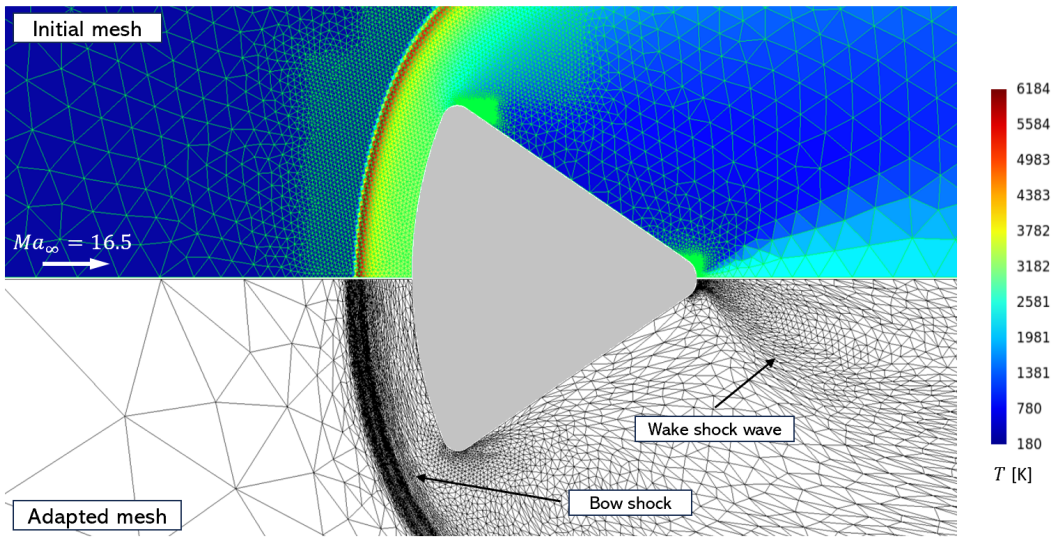


Figure 5.15: Thermal gradient based *h-adaptation* method applied to the *Ma16* case around the Apollo Command Module of Chapter 1. The adapted mesh is displayed on the lower part of the figure.

On Fig. 5.15, the minimum length is set to $1e^{-5}[m]$, the adaptation is based on the trans-rotational temperature gradients and the ratio of total elements before and after adaptation is one. As we can see, the initial distribution of the elements is corrected and areas subjected to strong temperature gradients such as the bow shock or the wake shock wave are refined.

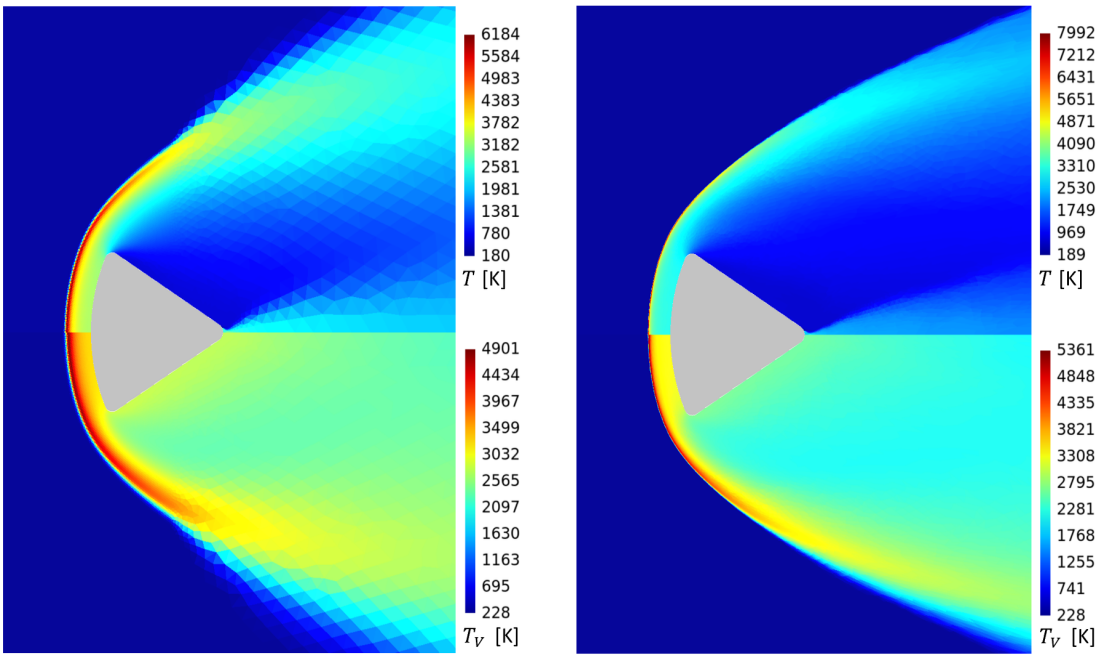


(a) Initial mesh

(b) Adapted mesh

Figure 5.16: Trans-rotational and vibrational temperatures distributions around the Apollo Command Module for the *Ma16* case. Simulations are performed on the "naive" initial mesh (left) and the h-adapted one (right). A pure and reactive molecular oxygen mixture is considered.

On Fig. 5.16, one observes the large impact of the *h-adaptation* method on the results. By means of the *shocking*$2T^{++}$ test code, the post-shock trans-rotational temperature is estimated at 10150K which gives an error of respectively 39% and 21% for the initial and adapted mesh. Note that the estimated peak temperature from the test code is based on the Rankine-Huguniot relations which may overestimate its value due to their theoretical aspect. Note that several iterations of adaptation can be performed in order to reduce this error percentage even more.

**Summary :**

In this section, the problematic of capturing shocks with high order methods has been discussed. Furthermore, given the restriction of modeling shocks at $p = 0$, the idea of using *h-adaptation* methods to enhance the accuracy of the results has been reviewed. This part of the discussion echoed the use of a configurable shock capture band in the previous section.

Finally, for the reasons seen above, the study of the impact of the interpolation order on the simulation results where shocks occur cannot be achieved at the moment. Therefore, one would need another test case which combines the particularity of modeling a high enthalpy flow and being shock-free at the same time. Such a case is proposed in the next section.

## 5.4 Thermal non-equilibrium in supersonic nozzle flows

In the previous section, the current limitation of Argo in capturing shocks at high orders has been discussed. One concluded that the simplest solution to avoid the simulations to breakdown was to model these sharp interfaces by lowering the polynomial order to zero and to locally refine the mesh to recover some lost accuracy. Such a refinement could be done either manually or through a proper *h-adaptation* method depending on the complexity of the mesh and its ease to be manually configurable.

However, one of the main motivations of using DG methods is to benefit from their high-order modeling capacity and, thereby, to avoid these strong refinements at low order. Therefore, the purpose of this section is to investigate the impact of higher order methods in modeling high enthalpy flows. To do so, a shock-free problem is required to get rid of the interpolation order constraint and the supersonic nozzle flow turned out to be a good candidate.

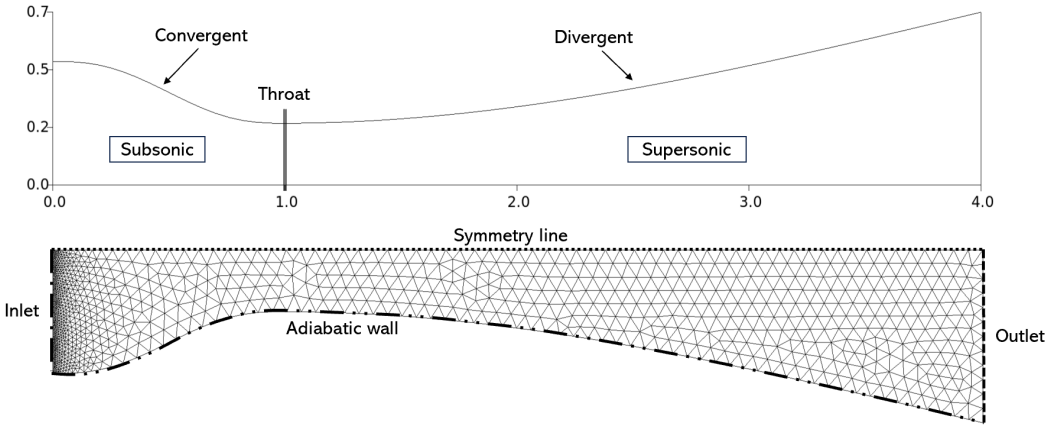


Figure 5.17: Representation of the nozzle geometry and the numerical setup of use in this section.

The test case consists in modeling a steady over-expanded inviscid flow in a supersonic nozzle where the dimensions of the nozzle have been taken from [74]. The inlet boundary condition

is characterised by the reservoir conditions summarized in Tab. 5.2 where thermal equilibrium is assumed. Given the supersonic outlet boundary condition, no information is needed except the initial pressure ratio between the reservoir and the outlet which is imposed to ensure a supersonic flow in the divergent section. The geometry of the nozzle as well as the numerical setup are proposed on Fig. 5.17.

Table 5.2: Reservoir conditions for the supersonic nozzle case.

| Mixture | $Y_0^{N^2}\,[-]$ | $Y_0^{N}\,[-]$ | $T_0 = T_{V0}\,[K]$ | $p_0\,[Pa]$ |
|---|---|---|---|---|
| *Nitrogen* | 0.983 | 0.017 | 5000 | 101325 |

Considering the numerical simulation, a $p = 2$ interpolation order has been used based on a three-level order sequencing. The tolerance on the convergence for the two first levels was $1e^{-6}$ while the last level (at $p = 2$) reduced the initial residual by 12 orders of magnitude. Given the implicit time integration, the GMRES algorithm is also used. Finally, the convective fluxes were estimated by means of the *AUSM+up* scheme. The distributions of the main flow parameters along the nozzle are displayed on Figs. 5.18-5.19 while the thermal relaxation is proposed on Fig. 5.20.

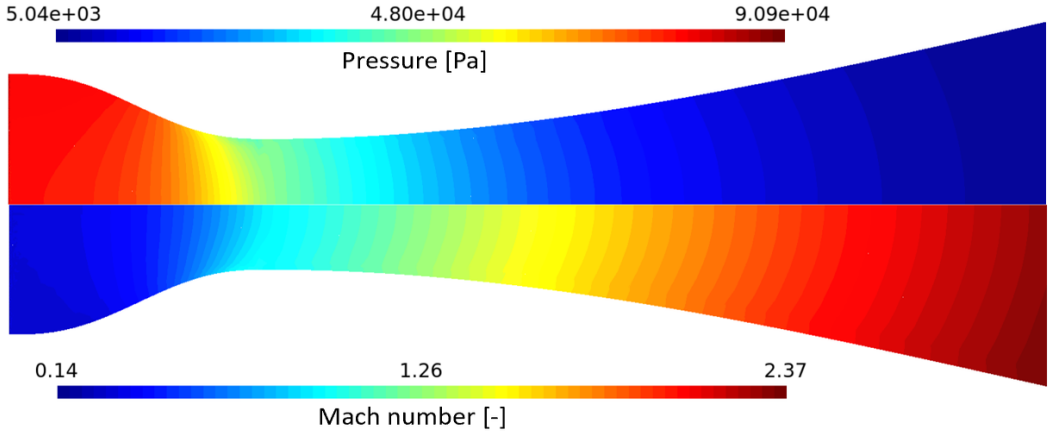


Figure 5.18: Distribution of the pressure and the Mach number along the supersonic nozzle.

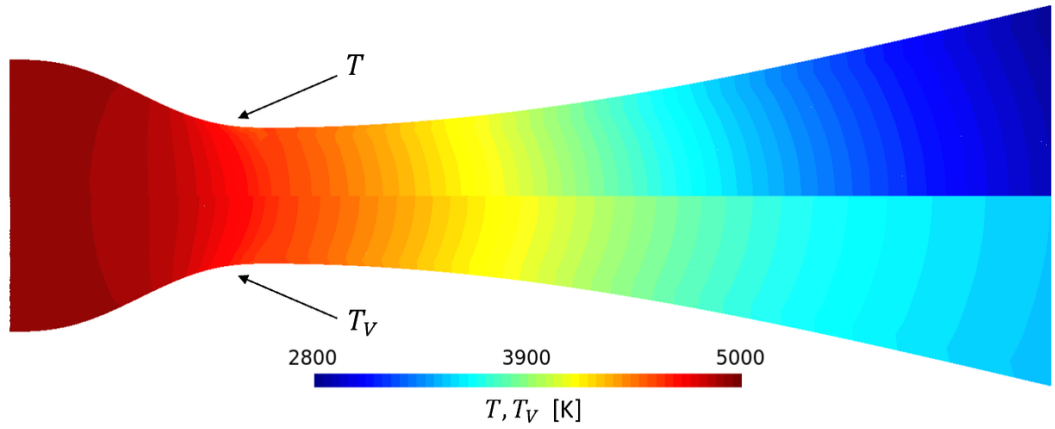


Figure 5.19: Distribution of the trans-rotational and vibrational temperatures along the supersonic nozzle.

One can observe a non-zero velocity right at the inlet and discrepancies between the specified reservoir conditions and the numerical values obtained at the inlet. For the temperatures, this phenomena can be seen on Fig. 5.20 where the trans-rotational temperature is equal to 4900K instead of 5000K. Note that the vibrational temperature, which corresponds to reservoir conditions, rapidly equilibrates the trans-rotational one such that both temperatures are in equilibrium in the convergent section of the nozzle.

This behaviour could be explained by the rapid reactional mechanisms occurring at the inlet due to the high temperatures encountered. Several tests have been carried out to mitigate this effect such as locally refining the mesh right at the inlet or setting the reservoir conditions at the equilibrium composition of nitrogen at 5000K. This equilibrium composition was given by the *mppequil* tool supplied with *Mutation* $++$, the resulting mass fractions are the ones in Tab. 5.2. Nevertheless, the problem persisted.

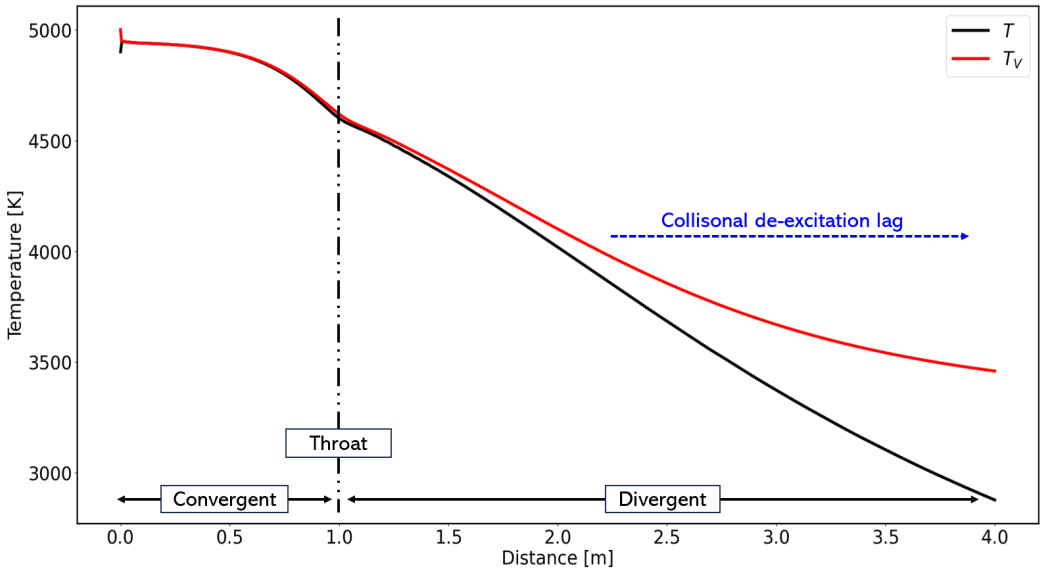


Figure 5.20: Thermal relaxation along the supersonic nozzle.

As mentioned above, thermal equilibrium is continuously achieved in most of the convergent section. This is not surprising as this part of the nozzle is subjected to small gradients leading to a trans-rotational temperature that remains at values which allow all vibrational levels to immediately adapt. Such a result is similar to the one obtained in [51] where a more in-depth discussion of this phenomena is proposed. However, when the flow approaches the throat, the trans-rotational temperature tends to rapidly decrease. Furthermore, due to the increasing flow regime along the nozzle axis, the energy exchanges tend to be frozen as their timescale becomes larger than the timescale of the flow. Thereby, a "lag" in the collisional de-excitation processes emerge and the vibrational and electronical internal modes cannot adapt. A non-equilibrium state is then created with a growing intensity towards the nozzle exit, as we can see on Fig. 5.20.

Note that the results obtained with the supersonic nozzle are very interesting as they are in complete opposition with the one discussed in Sec. 5.2. In fact, when the hypersonic flow past a blunt body was considered, the flow was initially characterised by a strong thermal non-equilibrium after the detached shock which tended to equilibrate downstream. On the other hand, in the nozzle, the flow jumped from an equilibrium state to a non-equilibrium state at the outlet.

Finally, on Figs. 5.21-5.22, the impact of the interpolation order is represented. The simulations were performed based on the exact same numerical setup except for numerical fluxes which are estimated with the flux-splitting *AUSM+up* scheme (see Fig. 5.21) and the Lax-Friedrichs scheme (see Fig. 5.22). Given the constancy of the problem inside the nozzle, no outstanding differences can be observed between the simulations at $p = 0$ and $p = 2$ when the *AUSM+up* scheme is considered. On the contrary, when the more diffusive Lax-Friedrichs scheme is used, strong discrepancies appear between the imposed conditions and the numerical values at the inlet and also between the temperature profiles all along the nozzle.

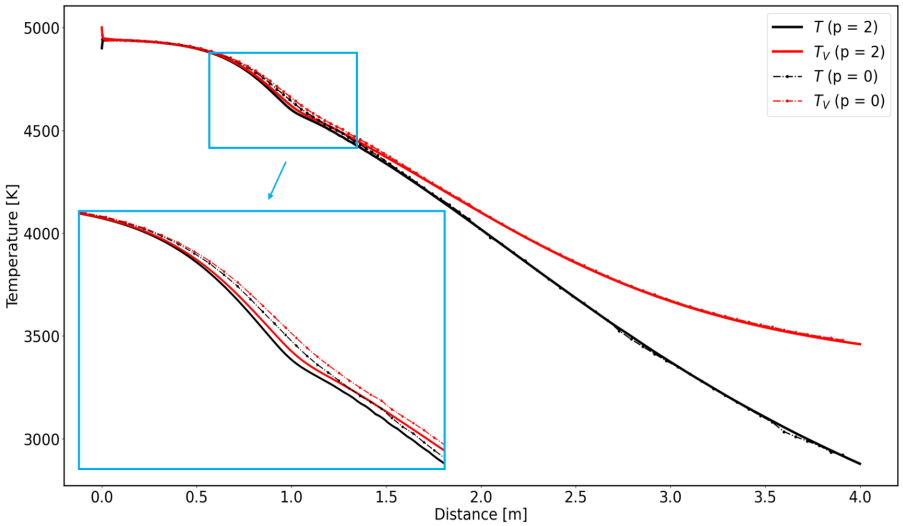


Figure 5.21: Comparison of the thermal relaxation under a $p = 0$ and $p = 2$ interpolation order. The interface fluxes are computed through the *AUSM+up* scheme.

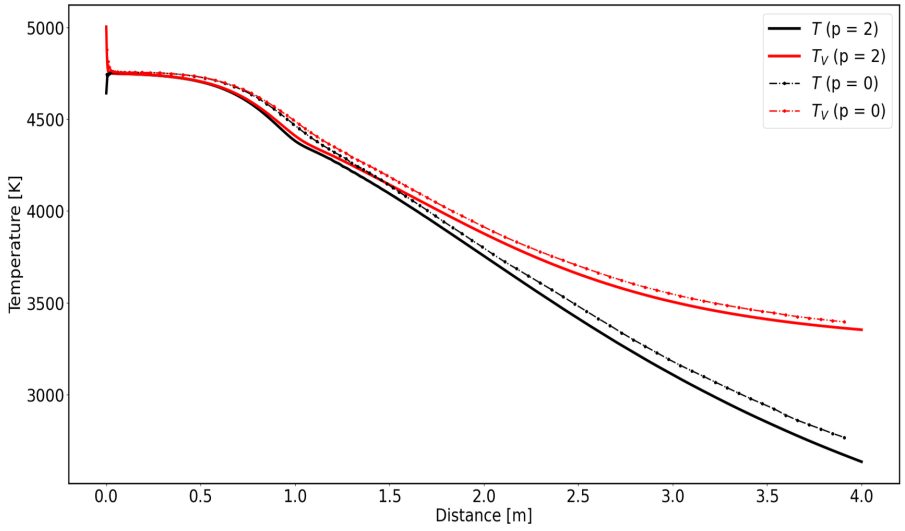


Figure 5.22: Comparison of the thermal relaxation under a $p = 0$ and $p = 2$ interpolation order. The interface fluxes are computed through the Lax-Friedrichs scheme.

## 5.5 Conclusion

In this chapter, the thermal non-equilibrium model implemented within Argo in the scope of this thesis has been used to model high enthalpy flows in various conditions.

In the first place, impact of the model on the thermochemical properties of the flow for a neutral and partially ionized mixture has been investigated. The studies have been made through the modeling of a hypersonic flow past a cylinder at Mach 16 and Mach 20. As expected, discrepancies between the Two-Temperature and the One-Temperature models in the species production straight after the shock have been observed. A strong difference between the two models has been noticed concerning the production of nitric oxide. As mentioned before, an accurate modeling of this species is crucial as it may have a large impact in the radiative heat flux prediction.

Finally, the current limitation of Argo in capturing shock at high orders has been discussed. The outcome was a constraint in the modeling of such problems only at an interpolant polynomial order of zero. Therefore, a shock-free problem allowing higher interpolation orders has been suggested.

CHAPTER

# SIX

# CONCLUSION

## 6.1 Achievements and main outcomes of this work

In this thesis, the module *DGAblation* of the multi-physics platform Argo has been extended allowing it to deal with thermal non-equilibrium based on the Two-Temperature model of Park [64, 65]. This module, developed by Schrooyen [74], is capable of providing highly reliable results by means of its strong coupling approach between the resolution of the material response and the flow field. Coupled with the advantage of Argo in modeling problems with unstructured meshes at high orders based on its Discontinuous Galerkin discretization scheme, this module allows accurate predictions in the thermal response of an ablative material.

Initially, the flow field was solved assuming equilibrium between all energy modes such that it was characterised by a single temperature. However, the conclusions of Park [65] about the limitation of one-temperature based models in predicting high enthalpy flows at hypersonic regime led to the development of a large variety of solvers capable to treat thermal non-equilibrium such as DPLR [86], US3D [13], LAURA [27], hy2Foam [15, 16], SU2-NEMO [45] or LeMANS [57]. Consequently, the motivation of this work was to fit the *DGAblation* module with such a feature in order to enhance its reliability. The development methodology was done in as follows.

The extension of the current Euler governing equations with respect to the Two-Temperature model was developed. This model assumes a non-equilibrium state between the translational-rotational and vibrational-electronic energy modes of the molecules resulting in an additional internal energy modes conservation equation. The thermodynamic and finite-rate chemistry properties required for the closure models were provided with the library $Mutation^{++}$.

Given the discontinuities at the interfaces of the mesh elements inherent to the Discontinuous Galerkin methods, the adaptation of two Riemann solvers to the extended governing model has been done : the Riemann solver based on the Lax-Friedrichs scheme and another one related to the AUSM+up flux-splitting scheme which gives the opportunity to treat low Mach number flows. In the same way, the Jacobians linked to the implicit time integration schemes have also been adapted to the new model where the convective terms have been treated analytically and the energy source terms through finite-differences.

The verification of the model within Argo has been possible through the development of two side codes, both written in $C^{++}$ and coupled to $Mutation^{++}$. The first one called $reactor2T^{++}$ consisted in a zero-dimensional adiabatic thermal bath which allowed to isolate the source

terms related to the energy transfers and the finite-rate chemistry. An external validation of this test code has been conducted based on the comparison of the obtained results with the ones of SU2-NEMO and LeMANS in [45]. The other code, *shocking*$2T^{++}$, allowed the validation of the convective terms and the correct extension of the Riemann solvers through the modeling of the thermochemical relaxation behind a strong normal shock. In both cases, good agreements in the results were found between the side codes and Argo, except for the free electrons population due to a possibly wrong evaluation of a quantity related to that species either in the test codes or in Argo.

Considering the governing model used in this work, the investigations have been mainly brought to the impact of the thermal non-equilibrium phenomena on the flow chemical kinetic. Two results are worth mentioning :

1. In steady conditions, discrepancies in the relaxation times and the species production rates (especially for the *NO* molecules) have been observed between the One-Temperature and Two-Temperature models right after the shock.
2. For unsteady conditions, differences over time in the species concentration at the wall have been experienced between the two models. Differences that tend to diminish as the flow was establishing itself resulting in common values at the wall in steady-state for both models.

Considering the important role of nitric oxide in the radiative phenomena [9] and the need for the ablative processes of an accurate prediction of the species present at the wall, considering thermal non-equilibrium in the modeling of the flow proved to be essential.

## 6.2 Perspectives

As discussed in Chapter 2, the physical model implemented during this thesis is derived from the Multi-Temperature Navier-Stokes equations where a series of assumptions were taken leading to the Two-Temperature Euler equations. Given this simplified model, some improvements to reach a higher fidelity level could be performed. Such improvements are discussed hereunder.

In the first place, one could enhance the accuracy of the model by considering the transport properties of the flow. Mass, momentum, and energy transport in fluids are governed by molecular collisions which require the evaluation of collision integrals. However, a multi-temperature collision integral database is already at disposal within *Mutation*$^{++}$ [77]. As a motivation, it has been shown that the non-equilibrium of the vibrational mode can have a large impact in the modeling of the heat flux [55].

Furthermore, radiative heat flux is also known to play an important role in heat transfers [65]. Therefore, it could be interesting to investigate their impact, especially with the higher production of *NO* molecules which has been observed in Chapter 5. The treatment of the radiative heat flux may however require the upgrade of the energy partitioning model to the Three-Temperature model where the vibrational and electronic-electron heat bath are not considered in the same manifold anymore. The reason of such an upgrade is discussed in [22, 21].

Considering the energy partitioning model itself, its extension to the Three-Temperature model is not a priority except if the radiation phenomena are considered. Nevertheless, an interesting feature would be the extension of the Two-Temperature model to deal with multiple vibrational temperatures for the diatomic particles. In the light of Sec. 2.3, it would require the addition of $x$ vibrational energy mode conservation equations where $x$ represents the number of separate vibrational temperatures. It has been shown that the Vibrational-Vibrational energy transfers promote vibrational energy redistribution between the vibrational energy pools

leading to a quicker relaxation towards equilibrium [16]. At the moment, *Mutation*$^{++}$ considers every diatomic particle as a single oscillator leading to a single vibrational temperature but the library has been specifically designed to be easily extendable.

Finally, given the higher computational cost of three-dimensional problems, the extension of the governing model to treat thermal non-equilibrium has been limited to two-dimensional problems. Furthermore, the optimisation of the code was not the priority here and may deserve a special care.

In conclusion, this work can be seen as a first step in the development of a complete and reliable thermal non-equilibrium model within Argo. Given the framework of a Master thesis, a more complete physical model would have been out of the scope. Nevertheless, some ideas of improvements for future work have been proposed.

# BIBLIOGRAPHY


[1] J. Allegre. The SR3 Low Density Wind Tunnel - Facility Capabilities and Research Development. In *28th Joint Propulsion Conference and Exhibit*, 1992.

[2] John D. Anderson Jr. *Hypersonic and High-Temperature Gas Dynamics, Second Edition*. American Institute of Aeronautics and Astronautics.

[3] F. Bassi and S. Rebay. High-Order Accurate Discontinuous Finite Element Solution of the 2D Euler Equations. *Journal of Computational Physics*, 138(2):251–285, 1997.

[4] Y. Bazilevs and T. J. Hughes. Weak Imposition of Dirichlet Boundary Conditions in Fluid Mechanics. *Computers & Fluids*, 36(1):12–26, 2007.

[5] G. A. Bird. Breakdown of Translational and Rotational Equilibrium in Gaseous Expansions. *AIAA Journal*, 8(11):1998–2003, 1970.

[6] V. H. Blackman. Vibrational Relaxation in Oxygen and Nitrogen. *Journal of Fluid Mechanics*, 1(01):61, 1956.

[7] M Cruellas Bordes. A study of an artificial viscosity technique for high-order Discontinuous galerkin methods. 2019.

[8] D. Bose and G. V. Candler. Thermal rate constants of the $N_2$ + O $\longrightarrow$ NO + N reaction using *ab initio* $^3A^{"}$ and $^3A^{'}$ potential energy surfaces. *Journal of Chemical Physics*, 104(8):2825–2833, 1996.

[9] Deepak Bose and Graham V. Candler. Thermal rate constants of the $O_2 + N \rightarrow NO + O$ reaction based on the $A_2'$ and $A_4'$ potential-energy surfaces. *Journal of Chemical Physics*, 107(16):6136–6145, October 1997.

[10] I. D. Boyd. Rotational-Translational Energy Transfer in Rarefied Nonequilibrium Flows. *Physics of Fluids*, 2(3):447–452, 1990.

[11] Jean-Luc Cambier and Stephane Moreau. Simulations of a molecular plasma in Collisional-Radiative nonequilibrium. In *24th Plasma Dynamics, and Lasers Conference*. American Institute of Aeronautics and Astronautics.

[12] Lorenzo Campoli, Elena Kustova, and Polina Maltseva. Assessment of machine learning methods for state-to-state approach in nonequilibrium flow simulations. 10(6):928.

[13] Graham V. Candler, Heath B. Johnson, Ioannis Nompelis, Vladimyr M. Gidzak, Pramod K. Subbareddy, and Michael Barnhardt. Development of the US3d code for advanced compressible and reacting flow simulations. In *53rd AIAA Aerospace Sciences Meeting*. American Institute of Aeronautics and Astronautics.

[14] Graham V Candler and Ioannis Nompelis. Computational Fluid Dynamics For Atmospheric Entry.

[15] Vincent Casseau, Daniel Espinoza, Thomas Scanlon, and Richard Brown. A Two-Temperature Open-Source CFD Model for Hypersonic Reacting Flows, Part Two: Multi-Dimensional Analysis. 3(4):45.

[16] Vincent Casseau, Rodrigo Palharini, Thomas Scanlon, and Richard Brown. A Two-Temperature open-source CFD Model for Hypersonic Reacting Flows, Part One: Zero-Dimensional Analysis. 3(4):34.

[17] F. Chalot, T. J. Hughes, and F. Shakib. Symmetrization of Conservation Laws with Entropy for High-Temperature Hypersonic Computations. *Computing Systems in Engineering*, 1(2–4):495–521, 1990.

[18] S. Chauveau, C. O. Laux, J. D. Kelley, and C. Kruger. Vibrationally-Specific Collisional-Radiative Model for Nonequilibrium Air Plasmas. 2002.

[19] Y. Chen and F. S. Milos. Ablation and Thermal Response Program for Spacecraft Heatshield Analysis. *Journal of Spacecraft and Rockets*, 36(3):475–483, 1999.

[20] A. V. Chikitkin, B. V. Rogov, G. Tirsky, and S. Utyuzhnikov. Effect of Bulk Viscosity in Supersonic Flow past Spacecraft. *Applied Numerical Mathematics*, 93:47–60, 2015.

[21] M. Clarey and R. B. Greendyke. Three-Temperature Thermochemical Nonequilibrium Model with Application to Slender-Body Wakes. *Journal of Thermophysics and Heat Transfer*, 2019.

[22] Matthew Clarey and Robert Greendyke. Investigation of the Thermochemical Non-Equilibrium Phenomena in the Wake of a Hypersonic Vehicle using Three-Temperature Models. In *2018 AIAA Aerospace Sciences Meeting*. American Institute of Aeronautics and Astronautics.

[23] G. Colonna, M. Tuttafesta, M. Capitelli, and D. Giordano. Non-Arrhenius NO Formation Rate in One-Dimensional Nozzle Airflow. *Journal of Thermophysics and Heat Transfer*, 13(3):372–375, 1999.

[24] Dmitri G. Fedorov, Shiro Koseki, Michael W. Schmidt, and Mark S. Gordon. Spin-orbit coupling in molecules: Chemistry beyond the adiabatic approximation. 22(3):551–592. Publisher: Taylor & Francis _eprint: https://doi.org/10.1080/0144235032000101743.

[25] P. Fernandez, N. Nguyen, and J. Peraire. A Physics-Based Shock Capturing Method for Large-Eddy Simulation. *arXiv (Cornell University)*, 2018.

[26] P A Gnoffo, R N Gupta, and J L Shinn. Conservation equations and physical models for hypersonic air flows in thermal and chemical nonequilibrium.

[27] Peter A. Gnoffo. An Upwind-Biased, Point-Implicit Relaxation Algorithm for Viscous, Compressible Perfect-Gas Flows. Number NASA STI/Recon Technical Report N, 1990.

[28] Sergei K Godunov and I Bohachevsky. Finite difference method for numerical computation of discontinuous solutions of the equations of fluid dynamics.

[29] David Hash, Joseph Olejniczak, Michael Wright, Dinesh Prabhu, Maria Pulsonetti, Brian Hollis, Peter Gnoffo, Michael Barnhardt, Ioannis Nompelis, and Graham Candler. FIRE II calculations for hypersonic nonequilibrium aerothermodynamics code verification: DPLR, LAURA, and US3d. In *45th AIAA Aerospace Sciences Meeting and Exhibit*. American Institute of Aeronautics and Astronautics.

[30] Koen Hillewaert. Development of the discontinuous galerkin method for high-resolution, large scale CFD and acoustics in industrial geometries.

[31] J. Michael Hollas. *Modern spectroscopy*. J. Wiley, 4th ed edition.

[32] Paul Houston and Endre Süli. *hp* -Adaptive Discontinuous Galerkin Finite Element Methods for First-Order Hyperbolic Problems. 23(4):1226–1252.

[33] K. P. Huber and G. Herzberg. *Molecular Spectra and Molecular Structure*. Springer US.

[34] Richard Jaffe. The calculation of high-temperature equilibrium and nonequilibrium specific heat data for $N_2$, $O_2$ and NO. In *22nd Thermophysics Conference*. American Institute of Aeronautics and Astronautics.

[35] Rita Kakkar. *Atomic and Molecular Spectroscopy: Basic Concepts and Applications*. Cambridge University Press, 1 edition.

[36] Hai Le, Ann Karagozian, and Jean-Luc Cambier. Complexity Reduction of Collisional-Radiative Kinetics for Atomic Plasma. *Physics of Plasmas*, 20(12):123304, 2013.

[37] J.-H. Lee. Basic governing equations for the flight regimes of aeroassisted orbital transfer vehicles. In *19th Thermophysics Conference*. American Institute of Aeronautics and Astronautics.

[38] Sanghoon Lee, Ikhyun Kim, Gisu Park, Jong Kook Lee, and Jae Gang Kim. Thermochemical nonequilibrium flow analysis in low enthalpy shock-tunnel facility. 15(10):e0240300.

[39] Meng-Sing Liou. A sequel to AUSM, Part II: AUSM+-up for all speeds. 214(1):137–170.

[40] Meng-Sing Liou and Jack Edwards. Numerical speed of sound and its application to schemes for all speeds. In *14th Computational Fluid Dynamics Conference*. American Institute of Aeronautics and Astronautics.

[41] Meng-Sing Liou and Christopher J. Steffen. A new flux splitting scheme. *Journal of Computational Physics*, 107(1):23–39, 1993.

[42] Kenny B. Lipkowitz and Donald B. Boyd, editors. *Reviews in Computational Chemistry. Volume 17*. Wiley-VCH, New York, 2001.

[43] Matthew MacLean, Michael Holden, Timothy Wadhams, and Ronald Parker. A computational analysis of thermochemical studies in the LENS facilities. In *45th AIAA Aerospace Sciences Meeting and Exhibit*. American Institute of Aeronautics and Astronautics.

[44] T. E. Magin, L. Caillault, A. Bourdon, and C. O. Laux. Nonequilibrium radiative heat flux modeling for the huygens entry probe. *Journal of Geophysical Research - Planets*, 111(E07S12):1–11, 2006.

[45] Walter T. Maier, Jacob T. Needels, Catarina Garbacz, Fábio Morgado, Juan J. Alonso, and Marco Fossati. SU2-NEMO: An Open-Source Framework for High-Mach Nonequilibrium Multi-Species Flows. 8(7):193.

[46] Peter V. Marrone and Charles E. Treanor. Chemical Relaxation with Preferential Dissociation from Excited Vibrational Levels. *The Physics of Fluids*, 6(9):1215, 1963.

[47] Franck Mazoue and Lionel Marraffa. Determination of the Radiation Emission during the Fire II Entry. 629:15, November 2006.

[48] Bonnie J McBride, Michael J Zehe, and Sanford Gordon. NASA Glenn Coefficients for Calculating Thermodynamic Properties of Individual Species.

[49] Donald A. McQuarrie. *Statistical Mechanics*. Harper Row, 10 East 53rd Street, New York, N.Y, 10022, 1976.

[50] Robert C. Millikan and David R. White. Systematics of Vibrational Relaxation. *Journal of Chemical Physics*, 39(12):3209–3213, 1963.

[51] Alessandro Munafo', Marco Panesi, Richard Jaffe, Thierry Magin, and Andrea Lani. Vibrational state to state kinetics in expanding and compressing nitrogen flows. In *10th AIAA/ASME Joint Thermophysics and Heat Transfer Conference*. American Institute of Aeronautics and Astronautics.

[52] Ekaterina Nagnibeda and Elena Kustova. *Non-Equilibrium Reacting Gas Flows*. Heat and Mass Transfer. Springer Berlin Heidelberg.

[53] Elena A. Nagnibeda, Ksenia V. Papina, and Olga Kunova. State-to-State Modeling of Non-Equilibrium Air Nozzle Flows. *Nucleation and Atmospheric Aerosols*, 2018.

[54] Eugene E. Nikitin and Jürgen Troe. 70 Years of Landau–Teller Theory for Collisional Energy Transfer. Semiclassical Three-Dimensional Generalizations of the Classical Collinear Model. *Physical Chemistry Chemical Physics*, 10(11):1483–1501, 2008.

[55] Ioannis Nompelis, Graham V. Candler, and Michael Holden. Effect of Vibrational Nonequilibrium on Hypersonic Double-Cone Experiments. *AIAA Journal*, 41(11):2162–2169, 2003.

[56] Ioannis Nompelis, Tyler Drayna, and Graham V. Candler. Development of a Hybrid Unstructured Implicit Solver for the Simulation of Reacting Flows over Complex Geometries. In *34th AIAA Fluid Dynamics Conference and Exhibit*, 2004.

[57] Ioannis Nompelis, Tyler Drayna, and Graham V. Candler. A Parallel Unstructured Implicit Solver for Hypersonic Reacting Flow Simulation. pages 389–395, 2006.

[58] Pamelia B. Pack. AS-202 Launch Vehicle Operational Flight Trajectory. Technical report, NASA Marshall Space Flight Center, Huntsville, Alabdma, 1966.

[59] A. V. Panasenko, L. B. Ruleva, and S. I. Solodovnikov. Increasing Hypersonic Aerodynamic Shock Tube Working Time Duration. *IOP Conference Series*, 927(1):012082, 2020.

[60] Marco Panesi. *Physical models for nonequilibrium plasma flow simulations at high speed reentry conditions*. PhD thesis, Pisa University, 2009.

[61] Marco Panesi, Richard L. Jaffe, David W. Schwenke, and Thierry Magin. Rovibrational Internal Energy Transfer and Dissociation of $N_2(^1\Sigma_g{}^+)$–$N(^4\Sigma_u{}^-)$ System in Hypersonic Flows. *Journal of Chemical Physics*, 138(4):044312, 2013.

[62] Marco Panesi, Thierry Magin, Anne Bourdon, Arnaud Bultel, and Olivier Chazot. Analysis of the FIRE II Flight Experiment by Means of a Collisional Radiative Model. In *46th AIAA Aerospace Sciences Meeting and Exhibit*. American Institute of Aeronautics and Astronautics.

[63] C. Park. On convergence of computation of chemically reacting flows. In *23rd Aerospace Sciences Meeting*. American Institute of Aeronautics and Astronautics.

[64] Chanyoung Park. Assessment of a Two-Temperature Kinetic Model for Dissociating and Weakly Ionizing Nitrogen. *Journal of Thermophysics and Heat Transfer*, 2(1):8–16, 1988.

[65] Chanyoung Park. Assessment of Two-Temperature Kinetic Model for Ionizing Air. *Journal of Thermophysics and Heat Transfer*, 3(3):233–244, 1989.

[66] Chanyoung Park. Review of Chemical-Kinetic Problems of Future NASA Missions. I - Earth Entries. *Journal of Thermophysics and Heat Transfer*, 7(3):385–398, 1993.

[67] Chanyoung Park, John T. Howe, Richard L. Jaffe, and Graham V. Candler. Review of Chemical-Kinetic Problems of Future NASA Missions. II - Mars Entries. *Journal of Thermophysics and Heat Transfer*, 8(1):9–23, 1994.

[68] Chanyoung Park, Richard L. Jaffe, and Harry Partridge. Chemical-Kinetic Parameters of Hyperbolic Earth Entry. *Journal of Thermophysics and Heat Transfer*, 15(1):76–90, 2001.

[69] Laurent Pierrot, Christophe Laux, and Charles Kruger. Vibrationally-specific collisional-radiative model for nonequilibrium nitrogen plasmas. In *29th AIAA, Plasmadynamics and Lasers Conference*. American Institute of Aeronautics and Astronautics.

[70] Najeh Rekik, Jaber Suleiman, Philippe Blaise, Marek J. Wójcik, Henryk T. Flakus, and Takahito Nakajima. Electrical Anharmonicity in Hydrogen Bonded Systems: Complete Interpretation of the IR Spectra of the C − L Stretching Band in the Gaseous $(CH_3)_2O \cdot ..HCl$ Complex. *Physical Chemistry Chemical Physics*, 19(8):5917–5931, 2017.

[71] W. J. Rider and R. B. Lowrie. The Use of Classical Lax-Friedrichs Riemann Solvers with Discontinuous Galerkin Methods. *International Journal for Numerical Methods in Fluids*, 40(3-4):479–486, 2002.

[72] Isil Sakraker, Ertan Umit, Thorsten Scholz, Paride Testani, and Gilles Baillet. Qarman: An Atmospheric Entry Experiment on Cubesat Platform.

[73] Hideo Sakurai, Masaharu Kobayasi, Isao Yamazaki, Mikio Shirouzu, and Makoto Yamamoto. Development of the Hypersonic Flight Experimental Vehicle. *Acta Astronautica*, 40(2-8):105–112, 1997.

[74] Pierre Schrooyen. *Numerical simulation of aerothermal flows through ablative thermal protection systems*. PhD thesis, Université catholique de Louvain, Louvain-la-Neuve, Belgium, 2015.

[75] Dieter Schwamborn, Thomas Gerhold, and Ralf Heinrich. The DLR TAU-Code: Recent Applications in Research and Industry. 2006.

[76] James Scoggins. Développement de méthodes numériques et Étude des phénomènes couplés d'Écoulement, de rayonnement, et d'ablation dans les problèmes d'entrée atmosphérique, 2017. NNT : 2017SACLC048.

[77] James B. Scoggins, Vincent Leroy, Georgios Bellas-Chatzigeorgis, Bruno Dias, and Thierry E. Magin. Mutation$^{++}$ : MUlticomponent Thermodynamic And Transport properties for IONized gases in C++. 12:100575.

[78] Surendra P. Sharma, Win Min Huo, and Chanyoung Park. Rate Parameters for Coupled Vibration-Dissociation in a Generalized SSH Approximation. *Journal of Thermophysics and Heat Transfer*, 6(1):9–21, 1992.

[79] Eiichi Shima and Keiichi Kitamura. Parameter-Free Simple Low-Dissipation AUSM-Family Scheme for All Speeds. *AIAA Journal*, 49(8):1693–1709, 2011.

[80] Hill L. Terrell. Ideal diatomic gas. In *An Introduction to Statistical Thermodynamics*, chapter 8, pages 147–160. Addison-Wesley, London, England, 1987.

[81] Ryan A. Thompson and Peter A. Gnoffo. Implementation of a Blowing Boundary Condition in the LAURA Code. In *46th AIAA Aerospace Sciences Meeting and Exhibit*, 2008.

[82] C.L. Tien and J.H. Lienhard. *Statistical Thermodynamics*. Hemisphere, Washington, 1979.

[83] Pham Tran, J.C. Paulat, and Patrick Boukhobza. Re-entry Flight Experiments Lessons Learned - The Atmospheric Reentry Demonstrator ARD. In *Flight Experiments for Hypersonic Vehicle Development*, Educational Notes RTO-EN-AVT-130, Paper 10, pages 10–1–10–46, Neuilly-sur-Seine, France, 2007. RTO.

[84] John von Neumann and Robert D. Richtmyer. A Method for the Numerical Calculation of Hydrodynamic Shocks. *Journal of Applied Physics*, 21(3):232–237, 1950.

[85] C. Wen and H. G. Hornung. Non-Equilibrium Dissociating Flow over Spheres. *Journal of Fluid Mechanics*, 299:389–405, 1995.

[86] M. J. Wright, Graham V. Candler, and Deepak Bose. Data-Parallel Line Relaxation Method for the Navier-Stokes Equations. *AIAA Journal*, 36(9):1603–1609, 1998.

[87] M. J. Wright, M. Loomis, and P. Papadopoulos. Aerothermal Analysis of the Project Fire II Afterbody Flow. *Journal of Thermophysics and Heat Transfer*, 17(2):240–249, 2003.

[88] Jianlong Yang and Meng Liu. Numerical analysis of hypersonic thermochemical non-equilibrium environment for an entry configuration in ionized flow. 32(12):2641–2654.

**UNIVERSITÉ CATHOLIQUE DE LOUVAIN**
**École polytechnique de Louvain**
Rue Archimède, 1 bte L6.11.01, 1348 Louvain-la-Neuve, Belgique | **www.uclouvain.be/epl**